

## X-RAY SPECTRAL ANALYSIS OF THE STEADY STATES OF GRS 1915+105

CHARITH S. PERIS<sup>1,2</sup>, RONALD A. REMILLARD<sup>3</sup>, JAMES F. STEINER<sup>1</sup>, SAEQA D. VRTILEK<sup>1</sup>,  
PEGGY VARNIÈRE<sup>4</sup>, JEROME RODRIGUEZ<sup>5</sup>, GUY POOLEY<sup>6</sup>

*Draft version October 23, 2021*

### ABSTRACT

We report on the X-ray spectral behavior within the steady states of GRS 1915+105. Our work is based on the full data set on the source obtained using the Proportional Counter Array on the Rossi X-ray Timing Explorer and 15 GHz radio data obtained using the Ryle Telescope. The steady observations within the X-ray data set naturally separated into two regions in the color-color diagram and we refer to them as steady-soft and steady-hard. GRS 1915+105 displays significant curvature in the coronal component in both the soft and hard data within the *RXTE*/PCA bandpass. A majority of the steady-soft observations displays a roughly constant inner disk radius ( $R_{\text{in}}$ ), while the steady-hard observations display an evolving disk truncation which is correlated to the mass accretion rate through the disk. The disk flux and coronal flux are strongly correlated in steady-hard observations and very weakly correlated in the steady-soft observations. Within the steady-hard observations we observe two particular circumstances when there are correlations between the coronal X-ray flux and the radio flux with log slopes  $\eta \sim 0.68 \pm 0.35$  and  $\eta \sim 1.12 \pm 0.13$ . They are consistent with the upper and lower tracks of Gallo et al. (2012), respectively. A comparison of model parameters to the state definitions show that almost all steady-soft observations match the criteria of either thermal or steep power law state, while a large portion of the steady-hard observations match the hard state criteria when the disk fraction constraint is neglected.

*Subject headings:* accretion, accretion disks — binaries: close — black hole physics — magnetic fields  
— X-rays: binaries — X-rays: individual (GRS 1915+105)

### 1. INTRODUCTION

The primary source of information about stellar mass black holes in the Milky way and nearby galaxies is the radiation from mass accretion systems known as black-hole binaries (BHBs). They consist of a secondary donor star that transfers matter on to the black hole, creating an accretion disk which is X-ray luminous. Today we have > 20 binary systems which have a dynamically determined primary mass above  $3 M_{\odot}$ : strong evidence to support the presence of a black hole.

The X-ray spectra of most BHBs are readily describable using a simple model consisting of a multi-temperature accretion disk component together with a hard X-ray power-law component which is widely attributed to inverse-Compton scattering of disk photons in a hot corona and modeled using a simple power-law or cut-off power-law function (McClintock & Remillard 2006). In most cases a Fe K $\alpha$  emission line should be included at  $\sim 6.4$  keV. Sometimes it is necessary to add a

disk reflection component when the inclination angle is  $\leq 60^{\circ}$ . In some cases absorption features are also evident (Ueda et al. 1998, see also Sobczak et al. 2000). Broadly speaking, this class of models has been employed to satisfactorily fit many spectra of numerous BHBs (e.g. LMC X-1, LMC X-3, GX 339-4, Ebisawa 1991; GS 2000+25, Ebisawa 1991; Takizawa 1991; Terada et al. 2002; GS 1354-64, Kitamoto et al. 1990; and Nova Muscae 91, Ebisawa et al. 1994; GRO J1650-40, Sobczak et al. 1999; XTE J1550-564, Sobczak et al. 2000) and have been an essential tool in forming a physical picture of these sources. Such endeavors at spectral fitting via such simple modeling has revealed that while individual BHBs have their own behavioral tendencies, BHBs generally occupy a few distinctive X-ray spectral-timing states (e.g., Remillard & McClintock 2006 hereafter RM06, Fender & Belloni 2004).

A black hole in outburst typically occupies one of three states: the thermal state, the hard state, or the steep power-law state (SPL; RM06). Loosely defined, the thermal state (also called the high/soft state) features domination of the X-ray spectrum by a hot accretion disk. The hard state (or low/hard state) features domination by a hard X-ray corona that is related to a steady radio jet. The SPL state (sometimes referred to as the very high state) shows a significant contribution from a steep power-law component which is linked to activity in a hot corona, the absence of a steady jet, but possible production of a transient jet and a prominent disk. These states have been pivotal in understanding the physics that generates different modes of black-hole accretion.

Of the BHBs discovered thus far, GRS 1915+105 (hereafter referred to as GRS1915) stands out as excep-

<sup>1</sup> Harvard-Smithsonian Center for Astrophysics, 60 Garden Street, Cambridge, MA 02138, U.S.A.; email:cperis@cfa.harvard.edu

<sup>2</sup> Department of Physics, Northeastern University, 360 Huntington Avenue, Boston, MA 02115, U.S.A.

<sup>3</sup> Kavli Institute for Astrophysics and Space Research, MIT, Cambridge, MA 02139, U.S.A.

<sup>4</sup> APC, AstroParticule & Cosmologie, UMR 7164 CNRS/N2P3, Université Paris Diderot, CEA/Irfu, Observatoire de Paris, Sorbonne Paris Cité, 10 rue Alice Domon et Léonie Duquet, 75205 Paris Cedex 13, France

<sup>5</sup> Laboratoire AIM, CEA/IRFU-CNRS/INSU-Université Paris Diderot, CEA DSM/IRFU/SAP, Centre de Saclay, 91191 Gif-sur-Yvette, France

<sup>6</sup> Astrophysics, Cavendish Laboratory, Madingley Road, Cambridge CB3 0HE, UK

tional in many ways. It was discovered in 1992 by the WATCH all-sky monitor on board GRANAT as a transient Galactic source (Castro-Tirado *et al.* 1992), and it sparked a lot of interest as the first Galactic object discovered to exhibit superluminal motion in its radio jets (Mirabel & Rodríguez 1994; Fender *et al.* 1999b). These Galactic radio jet sources, which display bi-polar radio emission analogous to that observed in radio-loud active galactic nuclei, are known as “microquasars”. Initial estimates suggested a  $\sim 14M_{\odot}$  black hole (Greiner *et al.* 2001). More recently, a trigonometric parallax was measured for the radio nucleus yielding a distance of  $8.6^{+2.0}_{-1.6}$  kpc and a revised primary mass of  $12.4^{+2.0}_{-1.8} M_{\odot}$  (Reid *et al.* 2014). Using a quantitative definition of the thermal state, McClintock *et al.* (2006) selected 22 disk dominated observations and calculated its spin to be  $a_* > 0.98$ , establishing GRS1915 as an extreme Kerr-hole.

Among the fundamental characteristics that set this black hole apart from the rest is GRS1915’s wild X-ray variability, the diversity of which has not been replicated in any other stellar-mass black hole. The complex X-ray light-curves of GRS1915 span at least 14 different variability classes (Belloni *et al.* 2000; Klein-Wolt *et al.* 2002; Hannikainen *et al.* 2005) and were thought to be unique until the recent discovery of a few similar patterns in IGR J17091-3624 (Altamirano *et al.* 2011). However, even though extreme variability is commonplace in its light-curve, about half of the observations of GRS1915 show fairly steady X-ray intensity (see Section 2.1), and most of these intervals yield spectra and power density spectra (PDS) that seem to resemble one of the three states (see Section 5; see also Munro *et al.* 1999; Klein-Wolt *et al.* 2002; McClintock & Remillard 2006). This suggests that within the complexity of this source is a simpler underlying basis of states which may map to those observed in canonical BHBs.

Historically, X-ray spectral analyses of the hot inner accretion disks in thermal states have shown that as the flux varies by several orders of magnitude, the value of the inner disk radius ( $R_{\text{in}}$ ) remains remarkably constant (Tanaka & Lewin 1995). This is also true for SPL state observations with low or modest Compton scattering fractions (Steiner *et al.* 2009a). The stability of  $R_{\text{in}}$  suggests a relationship to the innermost stable circular orbit ( $R_{\text{ISCO}}$ ), as prescribed by General Relativity. In the hard and quiescent states, however, direct measurements of the thermal emission from the inner disk have been elusive. The low temperatures of hard state disks makes them nearly undetectable for many instruments (e.g., XTE J1118+480,  $\sim 0.024$  keV, McClintock *et al.* 2001; Swift J1753.5-0127,  $\sim 0.2$  keV, Miller *et al.* 2006,  $\sim 0.28 - 0.37$  keV, Miller & Rykoff 2007; GX339-4,  $\sim 0.24$  keV, Belloni *et al.* 2013;  $\sim 0.22$  keV, Shidatsu *et al.* 2011; Cyg X-1,  $\sim 0.2$  keV, Makishima *et al.* 2008). This has led to studies in the hard state being focused primarily on the power-law component of the spectrum using the observed flux as an approximation to the total coronal flux. In this context, GRS1915 presents a unique opportunity. It displays a consistently hot disk even in its harder states (Munro *et al.* 1999). We will also exploit this high temperature disk to separate the disk and coronal contributions to the spectrum and explore their

behavior within both soft and hard observations.

Correlations between the radio and X-ray fluxes of hard and quiescent state BHBs have been a source of interest as they indicate a likely physical relationship between the radio jet and the X-ray emitting corona (and possibly the disk as well). After Corbel *et al.* (2003) first reported the correlation over a wide flux range for GX 339-4, Gallo *et al.* (2003, 2006) found that the same relationship ( $L_r \propto L_X^{\eta}$  where  $\eta = 0.58 \pm 0.16$ ) held for a number of hard state black holes. Gallo *et al.* (2012) revisited this inquiry and critically investigated a growing number of outliers to the X-ray–radio correlation and found evidence for a distinct second track (see also Coriat *et al.* 2011). The first track of  $\eta = 0.63 \pm 0.03$  corresponded to the prior track and a second track was revealed with log slope  $\eta = 0.98 \pm 0.08$ . These two tracks are thought to reflect different accretion regimes within the hard state. Gallo *et al.* (2012) did not include GRS1915 in their analysis.

The X-ray–radio correlation in GRS1915 was investigated by Rushton *et al.* (2010) using All-Sky Monitor (ASM) and Ryle telescope data. They found close coupling between the mechanisms that produced X-rays and the radio within hard observations displaying a steady radio jet (“radio plateau” states; Munro *et al.* 2001), which they fitted with an index of  $\eta \sim 1.7 \pm 0.3$ . This index, which showed GRS1915 to be distinct from other BHBs, suggested that the dominant mode of hard-state accretion in GRS1915 is efficient, unlike canonical BHB hard states. We will employ our complete *RXTE*/PCA data set of GRS1915 to revisit and explore the X-ray–radio correlation, while being able to clearly distinguish the coronal flux from the total flux that is conveyed by the ASM.

The spectrum of GRS1915 has been notoriously difficult to describe using standard BHB models (see Munro *et al.* 1999; McClintock *et al.* 2006; Titarchuk & Seifina 2009). Therefore, our main goal is to fit a majority of our data, which consists of an ensemble of locally steady conditions of GRS1915 (described in detail in Section 2.1) with the simplest possible phenomenological models. We will discuss the correlations between the model parameters which will include addressing simple questions such as: “How does the inner radius of the accretion disk behave?”, “Does the disk exhibit any connection to the corona?”, “Do the corona and the disk show a connection to the radio jet?”. We will then attempt to explain the physics revealed by the parameter variation.

In Section 2, we describe our observations. In Section 3, we present an overview of the spectral modeling process terminating with a description of the successful models which we use to analyze the data. We present the results of our spectral analysis in Section 4, followed by a comparison of our observations to canonical BHB states and to the variable states of GRS1915 (Belloni *et al.* 2000) in Section 5. We discuss the implications of our results in Section 6 and end with a summary of our core conclusions.

## 2. OBSERVATIONS

### 2.1. X-ray Data

*RXTE* consists of three instruments; the Proportional

Counter Array (PCA), the High-Energy X-ray Timing Experiment (HEXTE) and the ASM. The *RXTE*/PCA consists of five co-aligned proportional counter units (PCUs), each with a collecting area of  $\sim 1600$  cm<sup>2</sup> and a xenon-filled detector volume with three layers of signal anodes. It is sensitive in the range of approximately 2 – 60 keV with energy resolution  $\approx 18$  % at 6 keV (see Jahoda et al. 2006).

The spectral fitting was conducted on data obtained using all layers of proportional counter unit 2 (PCU-2) because it was operating during almost every observation. The PCA background subtraction was conducted using the `pcabackest` task of the `HEASOFT`/`FTOOLS` package. We used the composite bright/faint source model of Markwardt (2012).

In this study, the elemental spectra consist of continuous data segments that occur between the common interruptions imposed by Earth occultations and the passage of the *RXTE* spacecraft through the South Atlantic Anomaly. We further imposed a segment break when the number of PCUs was changed or to exclude data when one of the PCUs was not operating properly.

During its operational period *RXTE*/PCA observed GRS1915  $\sim 1800$  times. We filtered this data for continuous data segments greater than 400 s in both standard 1 and standard 2 data modes and found 2565 intervals exceeding 5.2 Ms, with a mean exposure of 2.1 ks. After imposing a further requirement that PCU-2 spectra are available with standard 2 data, then the total number of data segments available became 2563.

We selected four energy bands A (2.2-3.6 keV), B (3.6-5.0 keV), C (5.0-8.6 keV) and D (8.6-18.0 keV) and defined soft color - or hardness ratio - HR1 as the count rate in B divided by the count rate in A; and hard color (HR2) as D/C. The four PCA energy bands are used to compute a color-color diagram (CD) and a hardness-intensity diagram (HID), with a scheme to normalize the count rates in each band, throughout the times of PCA observations (1996-2012). Such normalized CDs and HIDs are shown for accreting black holes and neutron stars in Muno et al. (2002), RM06 and Lin et al. (2007). However, there is one significant difference in the normalization strategy used in the present paper. Previously, it was assumed that the X-ray spectrum of the Crab Nebula is invariant, and the PCA count rates in each energy band were normalized to ensure that the Crab CD and HID display constant values, except for statistical fluctuations. However, it has been shown that the Crab Nebula actually varies at the level of several percent over timescales of months (Wilson-Hodge et al. 2011). Their work utilized the observations of several instruments, including the *RXTE*/PCA. It can be concluded that the physical model for the PCA Instrument, which is used to normalize the PCA response files, is “stiffer” than the Crab variations, i.e., the models parameters change on longer timescales, allowing the Crab variations to be seen.

In the present investigation, the PCA response files serve as the basis for the 4-band normalizations. We simulated Crab-like spectra (`XSPEC`: `FAKET`) at 30 day intervals between 1996 January and 2012 January. The simulated spectra adopted the mean PCA Crab spectral parameters, i.e. a power law with photon index ( $\Gamma$ ) 2.11, normalization constant 10.55, and interstellar absorption  $N_H = 3.45 \times 10^{21}$  cm<sup>-2</sup>. For each simulated PCU spec-

trum, we extracted the count rates within the four intervals noted above. We then normalized each band to global constants, using piece-wise linear fits during each PCU gain epoch. The targeted normalization constants, per energy band, are the same values used in Lin et al. (2007), i.e., 550, 550, 850, and 570 counts/s. The normalization parameters, per PCU and per time interval, can then be applied to any PCA data.

There is one caveat to this process that concerns the lowest energy band (channel A). When the Crab observations themselves are normalized by the response files, via the Crab-simulated spectra described above, the mean values for the normalized energy bands agree with the target values, except for channel A. There is a very significant discrepancy between the real Crab spectra and the simulated spectra at energies below  $\sim 3$  keV, where there are substantial numbers of counts. This discrepancy underlies the common practice of PCA users to adopt lower limits for spectral fitting that are typically in the range  $\sim 2.5$ -3.0 keV. We choose to compensate for this problem by imposing an additional normalization constant per PCU and per gain epoch for channel A (only) that brings the real Crab count rates in line with the target value. The additional correction factors to the A Channel are typically in the range 5-15 %, depending on PCU and time interval. Such values are similar to or less than the factors that normalize different PCUs during a given time interval, or the factors that relate different time epochs for a given PCU (e.g., across the times of gain changes or the times when the propane layer was lost for two of the PCUs.)

This paper is focused on the results of spectral fits for the data segments that we infer to be quasi-steady. We have found that the best way to define quasi-steady conditions is to consider three measurement quantities: the source fractional variations (i.e., rms / mean) in 1 s bins, the same measurement with 16 s bins, and the rms variations in the soft color (HR1). Each of these quantities allows us to easily identify the types of variable light curves characterized by high amplitude cycles that operate at timescales of minutes or longer (e.g., variability classes  $\beta, \nu, \mu, \theta, \lambda, \kappa, \rho$ ; see Belloni et al. 2000). However, there are overlapping values of fractional variability (e.g., at 1 s) between light curve types that would appear to be quasi-steady (e.g., class  $\chi$ , which displays hard-state flickering widely treated as quasi-steady), versus others that display tracks in the CD that suggest temperature variations which cannot be averaged (e.g., weaker episodes of classes  $\gamma$  or  $\delta$ ). We report, in advance, that none of the conclusions offered in this paper are changed if we impose additional restrictions that eliminate data selections when there are appearances of weak  $\gamma$  or  $\delta$  characteristics in the light curves. Such cases are subtle, and they would amount to 1-2 % and 4-5 % of the steady intervals, respectively.

The values displayed by GRS1915 for the three variability quantities are shown in Figure 1. We select segments as “quasi-steady” if the fractional variability at 1 s is less than 0.12, the fractional variability at 16 s is less than 0.08, and the variations in HR1 (16 s) is less than 0.03. These selection criteria are displayed with blue lines in the lower-left corner of each panel in Figure 1. There are 1257 data segments (which is 49% of

2563 total) that lie in both selection boxes.

The HID and CD of GRS1915 are displayed in Figure 2 for the 1257 steady observations (2.55 Ms total exposure) that are the focus of this paper. The gaps between these steady observations show a broad distribution, ranging from 0.1 to 35 days (with an average of 2.2 days). We divide these observations into two groups which are best separated in the CD. We refer to the softer extended set of observations as “steady-soft” (red circles; 264 data points totaling 0.54 Ms) and the dense cluster of harder points as “steady-hard” (black squares; 993 data points totaling 2.01 Ms) throughout this paper. A tiny clump of points at [0.4, 1.55] in the CD which appeared ambiguous in the classification was identified as steady-soft, using the low integrated rms power (0.1-10 Hz) to discriminate. We note that this soft/hard separation is based only on the location of the observations in the CD and not on the more general thermal state and hard state classifications given by RM06.

## 2.2. Simultaneous Radio Data

The Ryle telescope (now transformed into the AMI large array) located at the Mullard Radio Astronomy Observatory in UK, was an east-west radio interferometer primarily used for microwave-background studies. Its standard observations were 12 hours apiece so as to fill the synthesized aperture. In order to monitor sources with short-period variability, a program began using interstitial intervals between the standard (long) observations. This program, documented by Pooley & Fender (1997) collected nearly daily observations of GRS1915, at 15 GHz, from May 1995 to June 2006; providing a 10 year overlap with our *RXTE*/PCA X-ray observations. We used the data from this program to study the radio properties of GRS1915 corresponding to its behavior at X-ray wavelengths.

Although baselines between 18 m and 4.8 km were available in a variety of configurations, most of the data used in this study were obtained using a more compact array, typically less than 150 m. Observations were alternated with a nearby calibrator, B 1920+154, so that instrumental phase variations could be detected and removed. The flux-density scale was set using 3C 48 and 3C 286. The data were sampled every 8 seconds and averaged into five minute data points with an rms noise of  $\sim 2$  mJy (Pooley & Fender 1997; Prat et al. 2010; Rushton et al. 2010). We typically average over a longer time period in our study and our fractional uncertainty is reduced.

To investigate the X-ray–radio correlations, we explored either restrictively analyzing the strictly simultaneous observations or alternatively employing a larger sample for which the observation mid-times matched within  $\pm 0.5$  days. In each case, we took the mean value of all radio data points corresponding to each X-ray observation as the corresponding radio flux of that observation. Since the results in both cases were consistent, we employ the latter selection – which is a significantly larger pool of data – in our full analysis presented below. We found 70 and 624 radio-matched X-ray observations in steady-soft and steady-hard, respectively.

## 3. SPECTRAL MODELLING

In this section we describe the fitting process and the models employed for the spectral fits. All fitting was done using XSPEC 12.8.1 (Arnaud 1996). Spectra were fitted over the energy range 2.52 - 45 keV. The lower limit of 2.52 keV reflects the low-energy calibration limit of the detector, and the upper value of 45 keV is chosen due to calibration uncertainty and low effective area at higher energies. To improve the sensitivity of our fits we used a more recent and improved calibration tool PCACORR (García et al. 2014). While PCACORR comes with a recommended systematic uncertainty as low as 0.1 % we employ the customarily used 1 % systematic uncertainty (e.g. Jahoda et al. 2006) for GRS1915 driven by simplicity of the models we employ.

After using the `xspec fit` command for the initial fitting, `xspec's "error"` command was used to find approximate confidence ranges for our main fit parameters. The error command varies the relevant parameter within its hard limits, and finds the change in value required to reach the  $\Delta\chi^2$  which corresponds to the desired confidence interval for 1 d.o.f. and assuming Gaussian statistics. In some cases, as a byproduct of this detailed search for the confidence interval, a new minimum for the fit-statistic may be found.

Given the approximate and idealized nature of the models available to fit the spectra of BHBs, we delineated between successful “good-fits” and poor fits adopting a critical goodness-of-fit  $\chi^2_\nu < 2$  (see also Steiner et al. 2010, 2011) which is appropriate for *RXTE*/PCA. We use only the “good-fits” for all analysis. The extremely large number of counts per spectrum in GRS1915 ( $\sim 5$  million) reduce channel errors significantly. This means that the uncertainty for many measurement bins is dominated by the systematic error, in which case our selection criteria admits errors (when using our simple models) of order  $\sim 1.4\%$ .

### 3.1. First model attempts

In this section we describe a subset of the models investigated to find the simplest ones that best fit the majority of the X-ray spectra. Up to 70 different model variants were explored with most producing unsatisfactory results. Typical BHB models incorporate a multi-temperature accretion disk coupled with a standard power-law component (a proxy for inverse Compton scattering) and a Fe-K $\alpha$  line component. We found that this simplest construction failed and that a strong requirement was the inclusion of a cutoff (i.e. curvature) with unusually low folding energy in the power-law component in order to produce good fits. This result established that the Compton component of GRS1915 (hereafter referred to in a more physical sense, as the ‘coronal component’) is unusually curved within the PCA bandpass. An exponential cutoff was also used in analyses by Munro et al. (1999) and Neilsen et al. (2011).

Gamma ray observations by Grove et al. (1998) has detected emission from GRS1915 at energies up to  $\sim 1$  MeV. X-ray observations by Zdziarski et al. (2001) and Rodriguez et al. (2008) also confirmed the presence of a power-law like component at higher energies, while observing curvature in the spectrum consistent with our observations at energies  $< 45$  keV. Our fits indicate that an additional power-law added into our fits does not affect our  $\chi^2_\nu$  values and number of good-fits. However, an

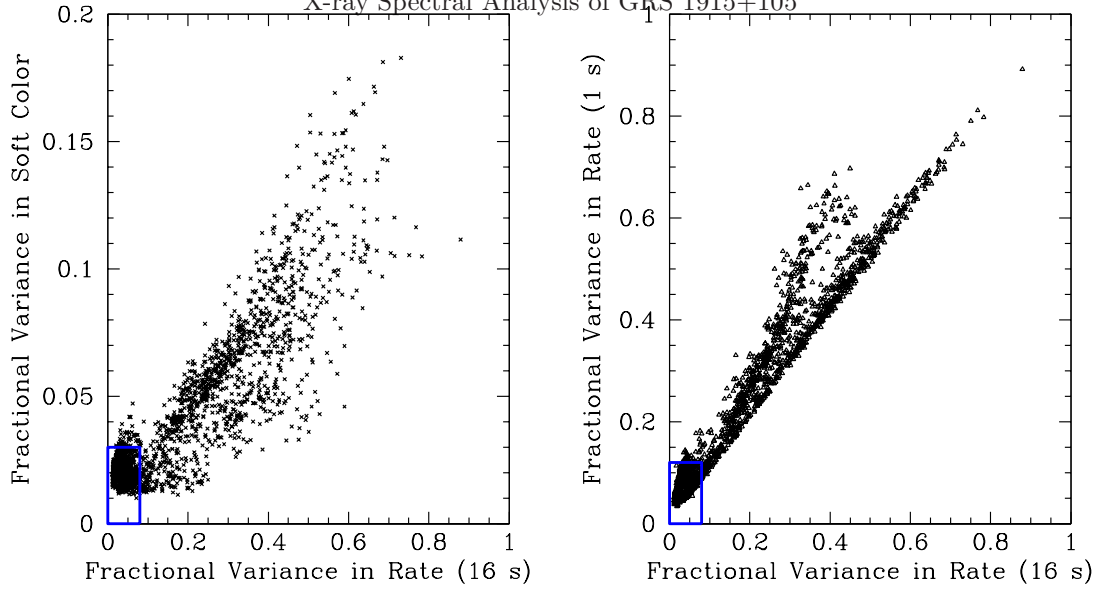


FIG. 1.— Observations are termed “quasi-steady” if the fractional variability at 1 s is less than 0.12, the fractional variability at 16 s is less than 0.08, and the variations in HR1 (16 s) is less than 0.03. These observations fall within both blue boxes in the plots shown.

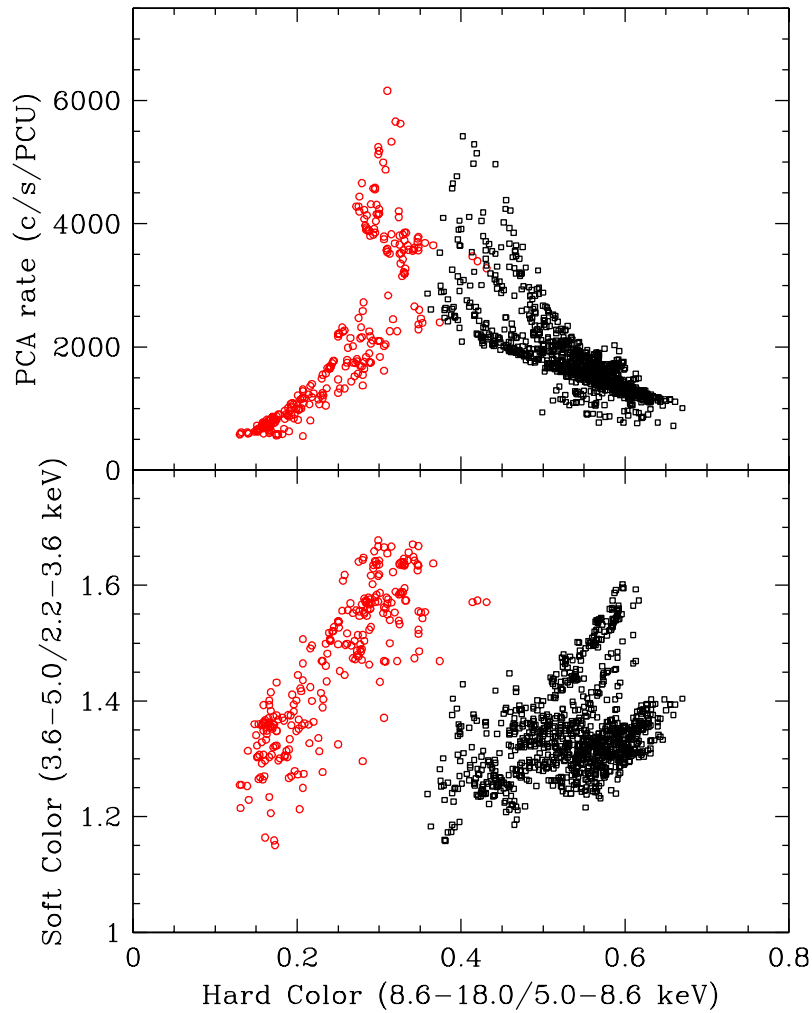


FIG. 2.— The hardness-intensity diagram (HID; *top*) and the color-color diagram (CD; *bottom*) of the steady state data of GRS1915. The steady-soft observations are represented by red circles and the steady-hard observations by black squares.

added power law cannot be constrained given the limited bandwidth available using *RXTE*/PCA. Therefore we do not use it for our fits and do not venture to describe the spectrum of GRS1915 at energies higher than the PCA bandwidth.

Next we explored a more physically-meaningful Comptonization model, *COMPTT*, to fit the corona component (Titarchuk 1994; Hua & Titarchuk 1995; Titarchuk & Lyubarskij 1995). In their paper modeling 107 spectra of GRS1915 in different spectral states, Titarchuk & Seifina (2009) showed that photons from the disk that are scattered by the corona have a constant characteristic temperature  $T_0 \sim 1$  keV. We found that by slightly adjusting their approach, so that the seed photon temperature was tied to the characteristic disk temperature  $T_{\text{disk}}$  (given by the component *EZDISKBB*), we were able to produce a satisfactory number of good-fits. However, beyond this artificial scaling between the characteristic disk temperature and the seed photons, the model showed erratic behavior in  $T_e$ . In addition, both  $T_e$  and the optical depth dropped below the limit where the analytical equations break down due to upscattering inefficiency (see figure 7 in Hua & Titarchuk (1995)). For these reasons, we eschewed this model in favor of an empirical approach.

### 3.2. The empirical approach to a power-law component: *SIMPLCUT*

In order to empirically describe the curvature in the corona component within a self-consistent and flexible framework, we modified the *SIMPL* model (Steiner et al. 2009b), to incorporate a high energy cutoff. *SIMPLCUT* is an extension of the approximate Comptonization component *SIMPL* with an additional parameter; a high energy exponential folding term  $-E_{\text{fold}}$ . The parameter  $\Gamma$  represents the asymptotic power-law before curvature comes into effect. This model is described by equations 3 and 4 in Steiner et al. (2009b) in tandem with an exponential folding in energy and will be described in detail in a future publication (Steiner et al., 2016). It was incorporated in *xspec* as a local model. This model has the virtue of being able to operate on an arbitrary seed spectrum, and conserves photon number – as appropriate for Comptonization. In practice we tied the seed photons to the spectrum of the accretion disk. A fraction of the seed photons  $f_{\text{sc}}$  are scattered into a curved power law shape, locally computed for each energy. Importantly, this enables the calculation of an *intrinsic* disk luminosity, i.e., the luminosity emitted by the disk directly, prior to any transfer or scattering which transpires in the corona. As already mentioned, this curvature is essential for achieving successful fits with GRS1915. *SIMPLCUT*, like *SIMPL*, also eliminates the unphysical rise at the lowest energies which is endemic in the standard *POWERLAW* model. Our approach, though empirical and approximate, allows us to obtain self-consistent values for the disk-normalization parameter and thereby to make physical inferences about changes and patterns in  $R_{\text{in}}$ .

### 3.3. Steady-hard model

As described in Section 2.1, the steady observations of GRS1915 naturally separate into two zones when represented in a CD or a HID (Figure 2). Due to the spectral

differences in these two regimes, we fit them with slightly different models. The backbone of both models was *SIMPLCUT*  $\otimes$  *EZDISKBB*.

In fitting the steady-hard data, the inclination of the system was fixed to  $i = 60^\circ$  (Reid et al. 2014) while the column density was fixed at  $N_H = 5 \times 10^{22} \text{ cm}^{-2}$  (Lee et al. 2002 and references therein). We also tested  $N_H$  values of  $4.5 - 7.0 \times 10^{22} \text{ cm}^{-2}$ . No noticeable changes in the parameter distributions were evident and our conclusions are not sensitive to this setting.

The steady-hard data were modeled via

*TBABS*  $\times$  (*SIMPLCUT*  $\otimes$  *EZDISKBB* + *LAOR* + *GAUSSIAN*).

The model is comprised of a number of elemental components: (*TBABS*, Wilms et al. 2000; *EZDISKBB*, Zimmerman et al. 2005; *LAOR*, Laor 1991). Both *LAOR* and *GAUSSIAN* line centers were fixed at 6.5 keV. The Gaussian width is forced to be very narrow (width fixed to 10 eV), corresponding to a distant, nonrelativistic Fe reflection line, which is sometimes observed. The addition of this component results in a 10 % increase in the number of good-fits. The *LAOR* component describes reflection in the strong-gravity regime in which extreme relativistic effects cause a red and broad distortion of the line (examples of similar broad and narrow Fe-line emission have been commonly observed in AGN; Brenneman et al. 2014). *EZDISKBB* is a standard multicolor disk model, for which the inner disk edge has a zero-torque boundary. This model yielded an impressive 992/993 good-fits (99.9%).

The yellow-filled boxes in Figure 3 show the distribution of the goodness-of-fit for the steady-hard data. It is clear that despite the strong signal, spectral complexity, and our minimalistic models, we are able to successfully model an impressive majority of this data.

### 3.4. Steady-soft model

In fitting the steady-soft data, we employed the same inclination ( $i = 60^\circ$ ), column density ( $N_H = 5 \times 10^{22} \text{ cm}^{-2}$ ) and range of column density examined ( $N_H = 4.5 - 7.0 \times 10^{22} \text{ cm}^{-2}$ ) as in the steady-hard observations, with no significant change in parameter distributions observed.

As noted in Section 3.1, we tested 70 model variants on GRS1915 spectra. This was driven by the need to add features, investigated one at a time, to gain acceptable fits for the steady-soft spectra. This is why the models for steady-soft and steady-hard observations differ. The extra terms have also been used for soft states, when required, by other researchers (see below).

The steady-soft data were modeled using

*TBABS*  $\times$  *SMEDGE*  $\times$  (*SIMPLCUT*  $\otimes$  *EZDISKBB* + *LAOR*)  $\times$  *GABS*

They require the addition of a smeared absorption edge (*SMEDGE*; Ebisawa et al. 1994, see also Sobczak et al. 1999), another feature of reflection, which onsets between 7.5-9.0 keV (the *SMEDGE* width was fixed to 7 keV). We additionally include a Gaussian Fe-absorption component (*GABS*) with width fixed to 0.5 keV and

central energy fitted between 6.3-7.5 keV. Fe-absorption in this region for the soft spectra of GRS1915 has been observed in previous studies (McClintock et al. 2006) and is probably due to the presence of a strong disk wind (Kotani et al. 2000; Neilsen & Lee 2009).  $\chi^2_\nu$  was significantly improved by the addition of these components although the key model parameters (i.e. the disk’s normalization and temperature) were not affected.

Strong degeneracy within the model fits in the steady-soft data was revealed when attempting to determine parameter uncertainties via xspec’s “error” command. In particular, we found degenerate trends allowing in very high  $\Gamma$  and high  $f_{sc}$ , as warned against as a modeling artifact in Steiner et al. (2009b). In order to proceed, and to mitigate this complication, we found it necessary to adopt a fixed value for  $\Gamma$ . We investigated 3 values which were chosen based on typical  $\Gamma$  values observed in canonical BHBs in soft states; 2.0, 2.5 and 3.0. While the parameter distributions remain relatively unaffected by the choice of value, we found that  $\Gamma = 2.0$  yields a lower number of good-fits while  $\Gamma = 3.0$  allows in observations which display degenerate tendencies. Hence we favor  $\Gamma = 2.5$ .

We also observed that a lower limit to  $E_{\text{fold}}$  of  $\sim 10$  keV is necessary for the success of this model. Although a significant number of our fits show  $E_{\text{fold}}$  cluster close to our lower limit, it serves to keep the coronal component from encroaching on the accretion disk and avoid degeneracy within our model fits.

Using this model and set of constraints, we obtained 135/264 good fits (51%) for the steady-soft observations. The red-outlined boxes in Figure 3 show the distribution of the goodness-of-fit for the steady-soft data. Admittedly, there is a broad distribution in  $\chi^2_\nu$ . We also acknowledge that the constraints we apply may limit the information we can obtain from our steady-soft model. However, due to the complexity of the steady-soft spectrum and the simplicity of the available models, we consider it *worthwhile* to examine the implied physical evolution of the steady-soft observations using our model.

Illustrative fits for both steady-hard (top panel) and steady-soft (bottom panel) are shown in Figure 4. Curvature is observed in the Compton components (see also McClintock & Remillard 2006; Neilsen et al. 2011).

#### 4. RESULTS

In this section, we present the results of our spectral analyses. All of the results described use only the good-fit observations characterized in Section 3. We report on the steady-soft and steady-hard behavior of the accretion disk, followed by the corona and then the radio jet. This is followed by a comparison of the observations of GRS1915 to canonical BHB states as well as to the variable states defined by Belloni et al. (2000).

##### 4.1. The accretion disk

The accretion disk parameters are of central interest to our investigation. Although the two models fitted to the steady-soft and steady-hard observations are different, each incorporates the multicolor disk model, EZDISKBB (Zimmerman et al. 2005), which has two free parameters: the maximum disk temperature ( $T_{\text{max}}$ ) and a normalization parameter ( $K$ ). From the normalization, it is

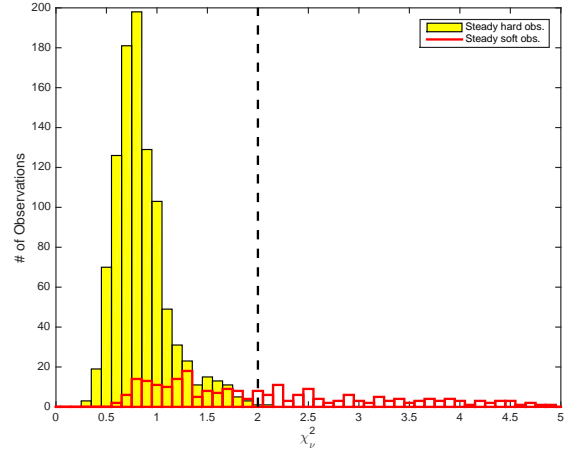


FIG. 3.— The distributions of  $\chi^2_\nu$  of steady-soft and steady-hard fits. The vertical dashed line at  $\chi^2_\nu = 2$  represents the cut defined for a good-fit.

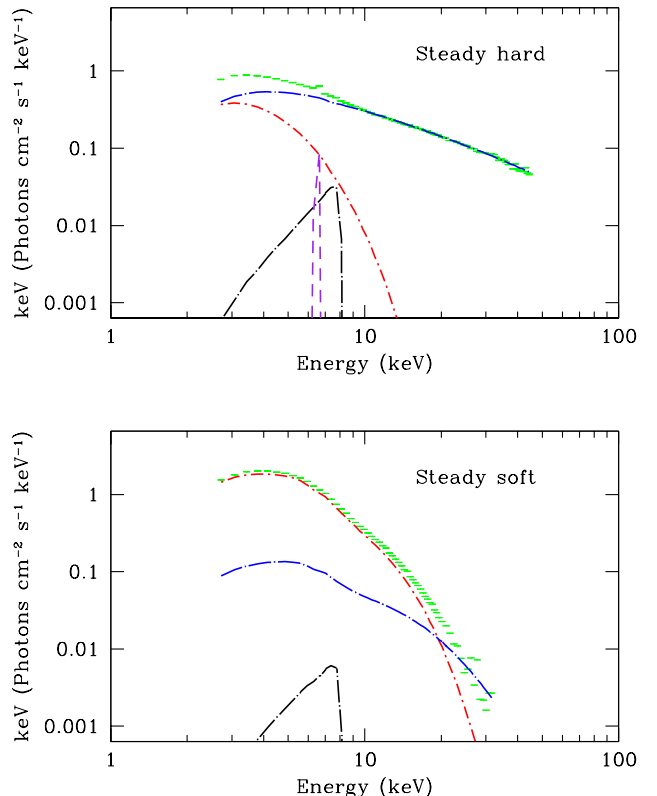


FIG. 4.— Two unfolded spectra which are typical and exemplify the steady-hard and steady-soft data, respectively. **Top:** The steady-hard spectrum for data segment 1103\_a (ObsID 20402-01-10-00) for which we obtain a fit with  $\chi^2_\nu = 0.76$ . **Bottom:** The steady-soft spectrum for data segment 0881\_a (ObsID 10408-01-11-00) for which we obtain a fit with  $\chi^2_\nu = 0.73$ . Data is represented in green, the disk component in red and the coronal component in blue. Note the curvature in both coronal components.

straightforward to determine  $R_{\text{in}}$ . We emphasize that by using SIMPLCUT, our model is self-consistent in counting Comptonized photons which enables us to directly obtain the *intrinsic*  $R_{\text{in}}$  (in km) via:

$$R_{\text{in}} = \left( \frac{K' f_{\text{col}}^4 D_{10}^2}{\cos(i)} \right)^{1/2} \quad (1)$$

where  $f_{\text{col}}$  is the color correction,  $i$  is the inclination and  $D$  is the distance to the source in kpc where  $D_{10} = \frac{D}{10}$  (distance in 10s of kpc) and

$$K' = \frac{K}{(1 - f_{\text{sc}})} \quad (2)$$

where  $f_{\text{sc}}$  is the scattering fraction determined by SIMPLCUT (which is implemented so as to directly report  $K'$ ). We note that many publications which do not use SIMPL or its derivative models and thus have no means of conserving photon number use the apparent inner disk radius ( $R_{\text{app}}$ ) for their analysis.  $R_{\text{in}}$  and  $R_{\text{app}}$  relate as:

$$R_{\text{in}} = \frac{R_{\text{app}}}{(1 - f_{\text{sc}})^{1/2}} \quad (3)$$

$R_{\text{in}}$  is calculated using a distance  $D = 8.6^{+2.0}_{-1.6}$  kpc, and inclination  $i = 60 \pm 5^\circ$  (Reid *et al.* 2014) and a constant color correction factor  $f_{\text{col}}=1.7$  (Shimura & Takahara 1995). We caution that the measurements of  $R_{\text{in}}$  are approximate and their accuracy is limited by the use of non-relativistic, classical models, and other simplifications including a single and static value for  $f_{\text{col}}$  – despite that it should vary with luminosity and depends upon mass and spin (e.g., Davis *et al.* 2006). However, despite these uncertainties which may affect the scaling, our primary interest in the radius measurements is to test for large-scale variations, for which these higher-order modifications are moot.

Figures 5 & 6 show the relationship between the disk temperature, the inner disk radius, the disk luminosity and the mass accretion rate. The mass accretion rate through the accretion disk is determined by

$$\dot{M} = \frac{2L_{\text{disk}}R_{\text{in}}}{GM} \quad (4)$$

where

$$L_{\text{disk}} = 73.9\sigma \left( \frac{T_{\text{max}}}{f_{\text{col}}} \right)^4 R_{\text{in}}^2 \quad (5)$$

(see Mitsuda *et al.* 1984; Makishima *et al.* 1986). Red points (upper panels) represent the steady-soft observations while black points (lower panels) represent the steady-hard observations. The relationships between these accretion disk parameters obtained using both steady-soft and steady-hard observations show reasonably ordered branches. We remind the reader that these branches observed are not necessarily time-ordered. They simply represent a collection of steady state data. In real time, the source can disappear from these diagrams into variable states and later reappear at a different steady location.

#### 4.1.1. The steady-soft accretion disk

Figure 5 displays a 4 cell grid of plots where we present the changes in  $R_{\text{in}}$  as a function of two quantities: luminosity (expressed as a fraction of the Eddington limit) and mass accretion rate through the disk. The upper panels and lower panels show the steady-soft (red circles) and steady-hard (black squares) observations respectively. Mean error bars for each plot are indicated in the right-hand bottom corner. Here and throughout, all errors presented describe  $1 \sigma$  confidence intervals.

A large majority of the steady-soft observations (96 %) display a roughly constant  $R_{\text{in}}$ , strongly reminiscent of the canonical BHB soft state (see also Tanaka & Lewin 1995). Given the constancy of this branch over the large range of luminosities, its  $R_{\text{in}}$  likely corresponds to  $R_{\text{ISCO}}$  for GRS1915. The slightly upward trend for  $R_{\text{in}}$  at higher luminosities (upper panels in Figure 5) is reminiscent of the “spin droop” which has been observed in several BHBs including GRS1915 itself (McClintock *et al.* 2006; see also Steiner *et al.* 2010, 2011). For this source, it is not likely to be caused by change in  $f_{\text{col}}$  (see also Done *et al.* 2007). It could instead be the result of a “local-Eddington effect” (Lin *et al.* 2009) tied to the maximum and roughly constant inner disk temperature seen at  $L_{\text{disk}} > 0.2L_{\text{Edd}}$  (see below). We cannot separate this effect from any structural changes in the disk that may occur at high  $L_{\text{disk}}$ .

At least six observations at low luminosity show a departure to larger  $R_{\text{in}}$  compared to the constant  $R_{\text{in}}$  branch<sup>7</sup>. Amidst our quest for quelling degeneracy in the choice of steady-soft model (see Section 3.4), we investigated the possibility that these points may be erroneous. However, our analyses revealed these points to be just as robust as all the other points which exhibit a more canonical result. Therefore we proceed, albeit with caution, to treat them as good-fits and include them in our analysis in Section 5. We also note that these points seem to lie in the  $L_{\text{disk}}-R_{\text{in}}$  space that is occupied by the steady-hard observations. However, their classification is unambiguously steady soft, which is further shown in Section 5.

Following the format of Figure 5, in Figure 6 we present a second 4 cell grid of plots which displays the changes in  $T_{\text{max}}$  against the same two quantities as before, luminosity and mass accretion rate through the disk. The steady-soft observations (upper panels of Figure 6) show temperatures between 1-2.4 keV (consistent with those observed by Muno *et al.* 1999 for observations with no QPO; see their figure 8b) with the constant  $R_{\text{in}}$  branch featuring higher temperatures of  $\sim 2$  keV. These temperatures are significantly higher than observed in other canonical BHB disks, for which a peak temperature of  $\leq 1$  keV is typical (e.g. RM06). The observations at low luminosity which show departure to larger  $R_{\text{in}}$ , also display the lowest temperatures.

#### 4.1.2. The steady-hard accretion disk

The lower panels of Figure 6 show the temperature of the inner disk for the steady-hard observations. They show a mean disk temperature of  $1.19 \pm 0.12$  keV corroborating the results of earlier studies which suggest the

<sup>7</sup> These are not the points at [0.4,1.55] in the CD which were close to the line between the hard/soft classification



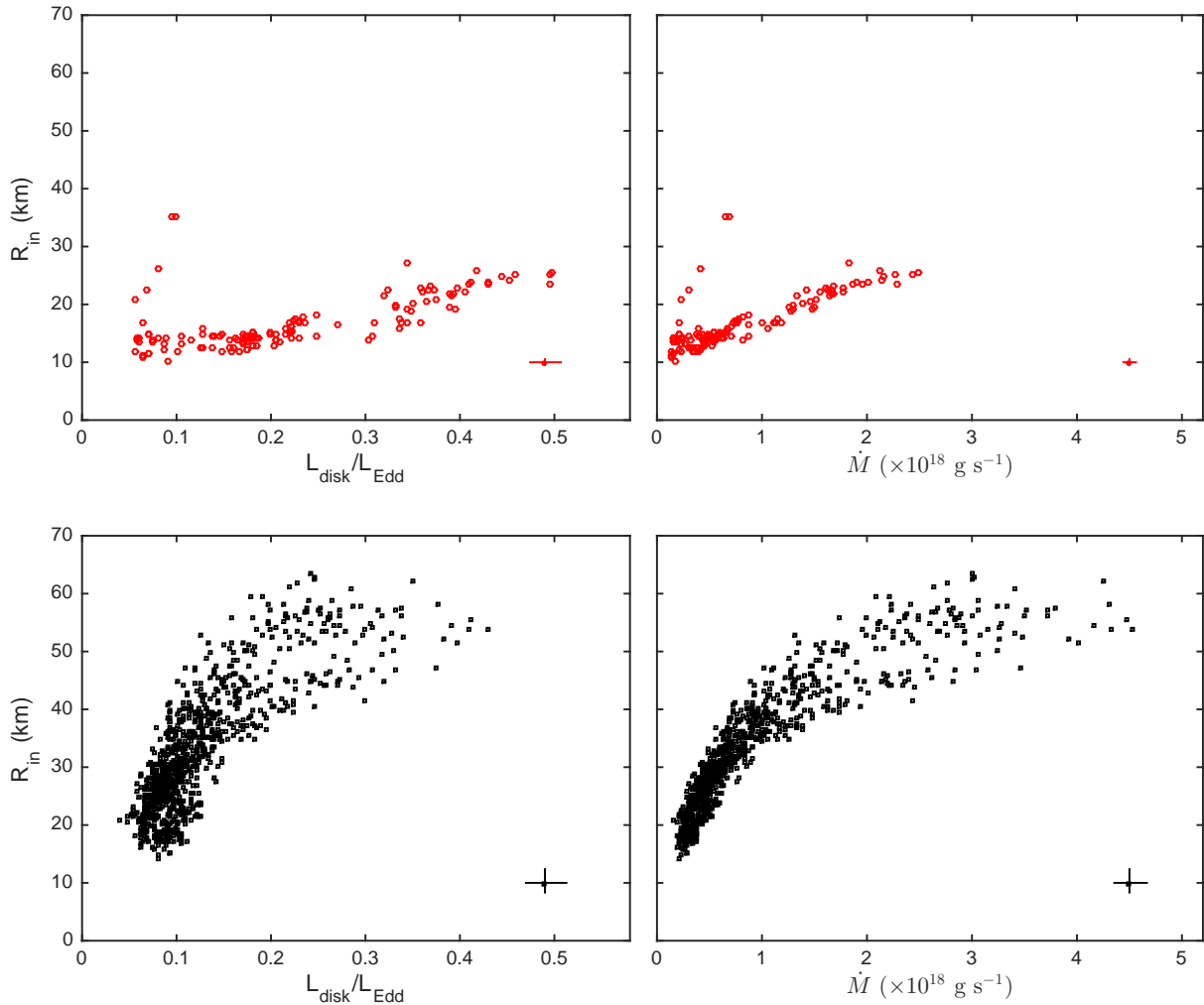


FIG. 5.—  $R_{\text{in}}$  as a function of the disk luminosity ( $L_{\text{disk}}/L_{\text{Edd}}$  where  $L_{\text{Edd}} \approx 1.3 \times 10^{38} (M/M_{\odot})$  erg s $^{-1}$ ; Frank et al. 1992) and mass accretion rate ( $\dot{M}$ ). Top panels show steady-soft observations represented by red circles. A branch showing approximately constant  $R_{\text{in}}$  is apparent. A few observations which show departure to larger  $R_{\text{in}}$  are present at low luminosity. Bottom panels show the steady-hard observations represented by back squares. An organized increase in  $R_{\text{in}}$  with increasing  $L_{\text{disk}}/L_{\text{Edd}}$  and  $\dot{M}$  is observed. The mean  $1\sigma$  error bars are indicated in the right-hand bottom corner of each plot. The full uncertainties (i.e. inclusive of the error due to distance and inclination) in the steady-soft and steady-hard parameters are as follows:  $R_{\text{in}} \sim 26\%$ ,  $L_{\text{disk}} \sim 55\%$  and  $\dot{M} \sim 90\%$ .

presence of a hot disk even in the harder observations of GRS1915 (Muno et al. 1999). This enables us to detect and measure the properties of the inner disk and explore its behavior. The most striking result (see Figure 5) is that  $R_{\text{in}}$  for the *steady-hard* data increases with growing disk luminosity and mass accretion rate, demonstrating an evolving, truncated disk.

Increases in  $R_{\text{in}}$  at much shorter time-scales, have been observed in the variable states of GRS1915 ( $\beta$  state, Belloni et al. 1997b,a;  $\rho$  state, Neilsen et al. 2011) suggesting a possible phenomenological link between the long ( $> 2.1$  ks) and short ( $\sim 10$ s of seconds) time scales in the system. This link will be further evaluated in Section 5.

Several processes can be hypothesized as possible

causes for this truncation and scaling:

- A local-Eddington effect for a thin disk
- An advection dominated accretion flow (ADAF)
- A magnetically-arrested disk (MAD)

A local Eddington effect has been invoked to interpret observations in which the inner disk reaches a maximum temperature, and further increases in luminosity are accommodated by increases in the disk radius at constant (maximum) temperature. Examples are several types of behavior in the accreting neutron star subclass known as Z sources (Lin et al. 2009) and the behavior of the disk in GRS1915 during the  $\rho$  state variability cycles

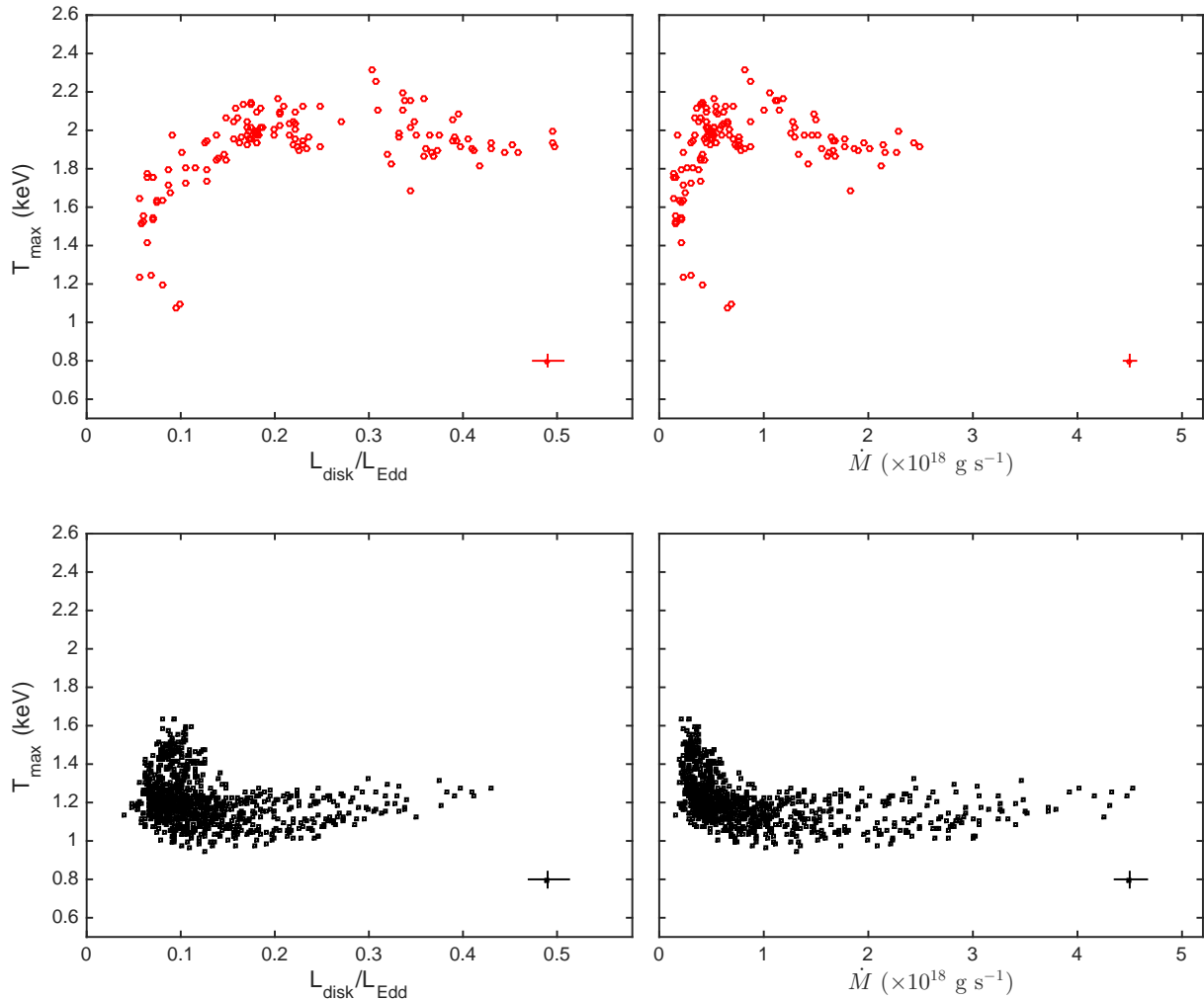


FIG. 6.—  $T_{\max}$  as a function of  $L_{\text{disk}}/L_{\text{Edd}}$  and  $\dot{M}$ . Top and bottom panels show, respectively, steady-soft and steady-hard observations, as in Figure 5. Mean  $1\sigma$  error bars are indicated as in Figure 5.

(Neilsen et al. 2011). This concept was mentioned in the context of the gradient of the roughly constant  $R_{\text{in}}$  branch of the steady-soft observations in Section 4.1.1. However, Figures 5 and 6 show that the steady-hard observations that show radius expansion exhibit temperatures a factor of two lower than the maximum temperatures observed in the system, and so we conclude that a local Eddington effect is not a viable explanation for radius expansion in steady-hard conditions.

An ADAF is characterized by a low density, optically thin, quasi-spherical flow where most of the viscous energy released does not radiate efficiently, resulting in the energy being advected into the black hole. The ADAF model offers an alternative solution to accretion in a thin disk, but the transition radius that may separate these accretion geometries must be determined empirically, rather than by deterministic factors (e.g., Esin et al. 1997). Given the organized behavior of the

steady-hard truncated disk (Figure 5), it would appear that the ADAF hypothesis, in and of itself, is incomplete. In the absence of an ADAF transition mechanism that moves out with growing disk luminosity, we do not discuss this alternative further.

The idea that global magnetic field properties may play a role to distinguish steady-soft and steady-hard conditions and magnetically truncate the accretion disk (Narayan et al. 2003; Tagger et al. 2004) is plausible. The concept here is that a vertical or poloidal magnetic field may be entrained into the inner disk region and then modify the geometry and energetics of the final stages of accretion. This is given further consideration in the Discussion (Section 6.3).

In Figure 5 (lower panels), we note a possible bifurcation in the steady-hard data points when GRS1915 becomes luminous,  $L \geq 20\%$  Eddington. The hint of split  $R_{\text{in}}$  tracks maps to a similar appearance of splitting in

the disk temperatures shown in Figure 6. We know of no clear explanation for such a phenomenon, if it is real.

#### 4.2. The disk–corona relationship

While the origin of the soft X-ray component observed in BHB spectra has been generally agreed upon as thermal radiation from an accretion disk, the origin of the hard X-ray component (power law or cutoff power law) is still poorly understood. The prevalent paradigm has been inverse Compton scattering in a nebulous plasma referred to as the corona. In this scenario, the seed photons are from the inner disk but the origin and geometry of the corona is uncertain (e.g. Poutanen 1999).

In Figure 7 (a,b) we explore the connection between the accretion disk and the corona. The use of the model SIMPLCUT enables us to obtain the fraction of photons from the disk that contribute to the coronal flux ( $f_{sc}$ ). This fraction is represented as a function of the coronal flux integrated over 0.1-100 keV, in Figure 7a.  $f_{sc}$  stays low within the steady-soft observations. In the steady-hard observations  $f_{sc}$  is unusually well-behaved holding steady between 0.2 – 0.5.

Figure 7b shows the division of spectral energy between the disk and coronal components. The steady-soft observations show comparatively low coronal flux and weak correlation between the disk and coronal components, with a slight growth in the contribution from the corona at high disk luminosity. While we fix  $\Gamma$  at 2.5 for the fits represented here (see Section 3.4), we note that the coronal flux slightly decreases if a lower power-law index ( $\Gamma = 2$ ) is used. However, as stated in Section 3.4, the coronal flux distribution remains unchanged. In contrast, the steady-hard observations exhibit a more luminous corona and a strong correlation between the component fluxes (Figure 7b; black points). The differences between these two tracks, despite considerable overlap in the flux from the accretion disk, could be taken to suggest that the coronae in the steady-soft and steady-hard conditions have different origins.

The strong correlation of the disk and coronal fluxes in the steady-hard observations suggests a connection between the processes that govern their production in GRS1915. Due to the extreme faintness of their disks, canonical BHBs in the hard state usually exhibit a near vertical track in the coronal flux versus disk-flux diagrams (see RM06). However, this correlation of disk and coronal flux might be a common feature of BHBs, which is undetected in canonical sources due to the faintness of their disks. X-ray observations of hard state BHBs with instruments sensitive to lower energies (e.g. NICER) will shed light on this matter in the future.

#### 4.3. The steady-hard corona

Due to the constraints enforced on the steady-soft model (discussed in Section 3.4) we focus on the steady-hard observations, in order to explore the coronal parameters. The distributions of these parameters appear more complex and varied than those of the accretion disk parameters.

In Figure 7 (c,d), we explore how the parameters related to the steady-hard coronal component, namely  $E_{fold}$  and  $\Gamma$ , vary as a function of coronal flux. Most of the steady-hard observations (80 %) show a power-law index in the range  $1.4 < \Gamma < 2.1$ , which is one of the

signatures of the canonical hard state (RM06). A more complete assessment of this is given in Section 5.

We note the presence of a sub-population of points at low coronal flux that have significantly high  $E_{fold}$  values compared to the norm while also displaying well-constrained  $\Gamma$  values ( $\sim 1.7$ ) with much less scatter. These observations display a move towards more typical hard state coronal characteristics (see Section 6.4). Although they occur at low flux values the high  $E_{fold}$  observations typically have  $\sim 2.7$  million counts per spectrum and their fits have been verified using the error command on xspec. The remaining observations display low  $E_{fold}$  values (between 10-30 keV), confirming the significant curvature in the Compton component within the PCA bandpass (Figure 7c).  $E_{fold}$  shows no obvious correlation with the coronal flux.  $\Gamma$  shows an overall increase with growing coronal flux (Figure 7d).

Indications of the existence of two (or maybe more) coronal tracks within the steady-hard observations are observed within both  $E_{fold}$  and  $\Gamma$  plots. We note the presence of two tracks at higher luminosities in Figure 7c and two tracks with differing slopes in Figure 7d. These tracks approximately match the set of tracks in Section 4.1.2, but do not map one-to-one. Further interpretation of this splitting is left for future work.

#### 4.4. The radio jet

In this section, we consider all radio observations that time-match (within  $\pm 0.5$  days) the steady-soft (70) and steady-hard (624) X-ray observations (see Section 2.2).

We first examine how the radio flux levels differ in the steady-hard and the steady-soft observations. In Figure 8 we show the radio flux (represented in log scale) as a function of time. We find that 95 % of the steady-hard data points have radio flux  $> 5$  mJy with the maximum radio flux exceeding 100 mJy at times. 99 % of the steady-hard data points have radio flux  $> 2$  mJy (consistent with Muno et al. 2001; Klein-Wolt et al. 2002). In the steady-soft data we conversely find that 77 % have radio flux  $< 2$  mJy and 99 % have radio  $< 5$  mJy. Our observations substantiate the idea that the steady-hard observations are associated with a radio jet. Some steady-soft observations show the presence of radio flux at lower levels. However, this low radio flux does not show any clear relationship with the steady-soft disk or corona. Furthermore, at low radio flux there is a chance that some portion of the emission arises from jet material which is detached from the core. This issue cannot be further investigated with these data given their insufficient spatial resolution. Hence we focus on the radio jet behavior of only the steady-hard observations.

#### 4.5. The corona–jet relationship

Strong coupling of the hard X-ray flux and the jet inferred from theory and observed in data (e.g. Fender et al. 1999a; Poutanen 1999) supports the proposition that in hard states, the corona is associated with the base of the jet. The importance of this coupling is evident in the work by Gallo et al. (2012) in uncovering two tracks relating X-ray and radio luminosity in multiple BHB systems. The study of this hard X-ray/radio connection may shed light on the process of jet formation.

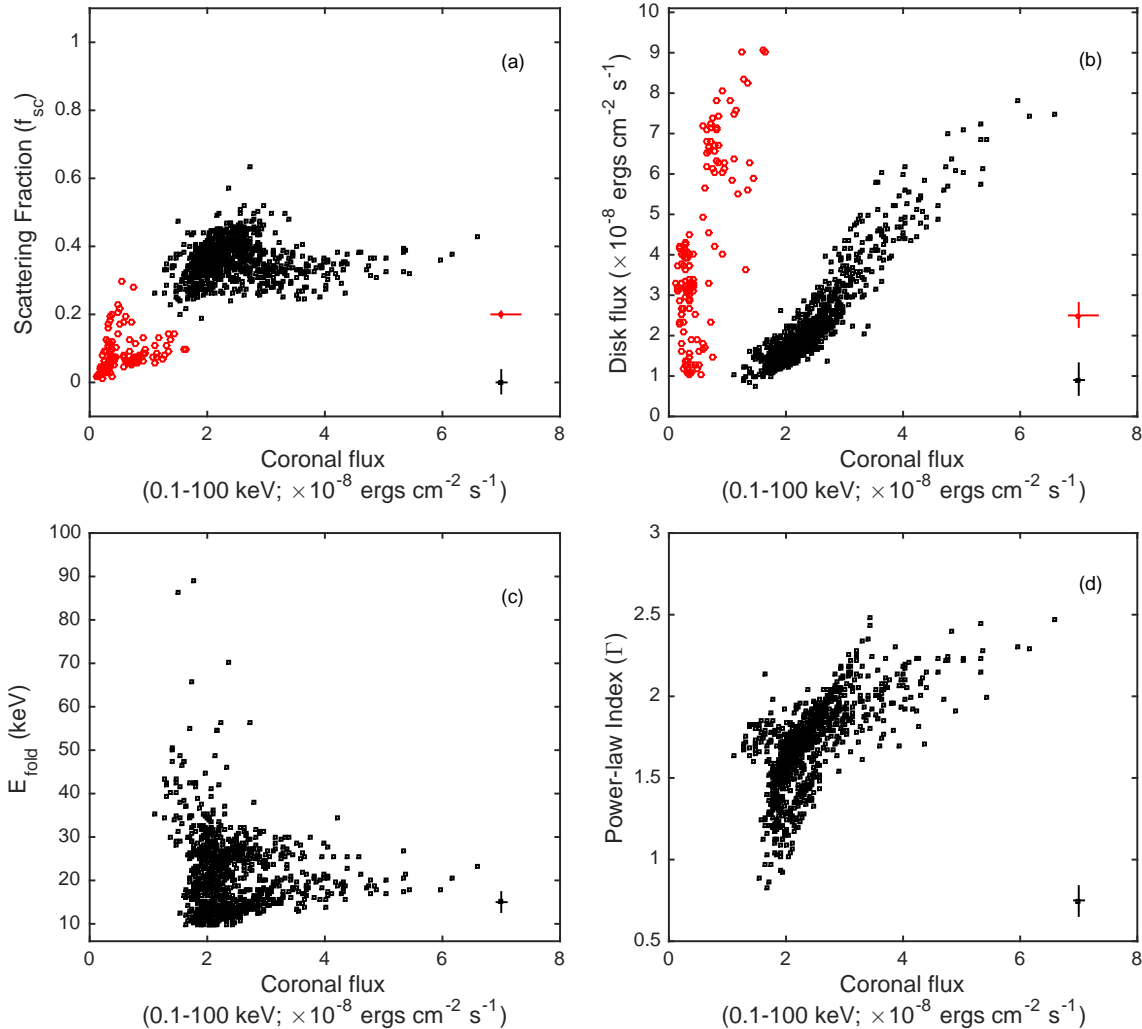


FIG. 7.— Top panels show (a) Scattering fraction ( $f_{sc}$ ) and (b) disk flux as a function of coronal flux in both steady-soft (red circles) and steady-hard (black squares) observations. Bottom panels show (c)  $E_{\text{fold}}$  and (d)  $\Gamma$  as functions of coronal flux in the steady-hard observations.

We isolate the coronal luminosity in the steady-hard observations of GRS1915 which produced good-fits (992/993), and investigate its behavior in response to the radio jet. Figure 9 shows the radio luminosity as a function of 1-10 keV X-ray luminosity<sup>8</sup>. We also overplot the Gallo et al. (2012) tracks (hereafter G12 tracks) in red (0.63 slope track) and blue (0.98 slope track). Taken as a whole, no obvious correlations are apparent. However, we identify three regions of interest: (1) the region with lowest coronal luminosity which seems to display a trend that matches the G12 tracks, (2) the region with highest radio luminosity which corresponds to a subset of the radio plateau state observations and (3) a diffuse region with high coronal luminosity which will be addressed in Section 4.6 (encircled by a green dashed line in Figures 9

<sup>8</sup> To be consistent with the results of Gallo et al. (2012) we use 1-10 keV integrated luminosities for this section.

and 12). In the following paragraphs we will discuss (1) and (2) in the context of recent literature.

The top two panels of Figure 10 show the steady-hard X-ray light curve in energy bands 2.2 - 8.6 keV and 8.6 - 18.0 keV. We note the presence of two time periods when the count-rate gradually decreases to low values in both bands. The first of these dips was categorized by Belloni et al. (2000) as the  $\chi_2$  class. The bottom panel in Figure 10 shows the radio light curve which indicates that the radio luminosity corresponding to the decline into these X-ray dips, is also relatively invariant. As the X-ray count-rate rises out of these light curve dips, the radio luminosity shows large variability ( $\sim 1$  order of magnitude). We neglect any such highly variable points. The points in the X-ray dips corresponding to the luminosity decline are isolated and shown in cyan in both Figures 9 and 10. They are defined by the time ranges given in Table 1. Interestingly, we find that these points

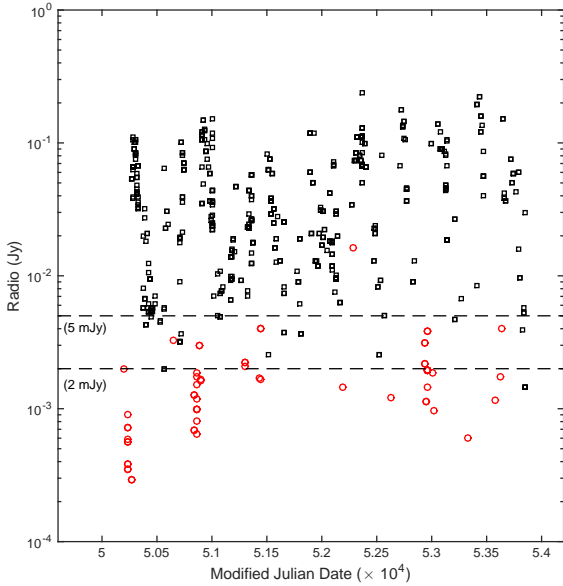


FIG. 8.— The Ryle telescope’s 15 GHz radio light curve of GRS1915’s jet activity. Black squares show the radio flux corresponding with steady-hard observations and the red circles correspond to steady-soft observations (i.e. within  $\pm 0.5$  days of the X-ray point). The dashed lines mark our reference flux levels of 5 mJy and 2 mJy. There is a clear difference in the brightness of the steady-hard compared to steady-soft data. We note that several steady-soft observations are not represented here due to extremely weak radio detections, or even non-detections. The single radio-bright steady-soft observation was tightly sandwiched between two hard states. Emission from jet material disconnected from the core possibly explains its higher radio flux. For reference, the typical error associated with each data point is  $\sim \pm 0.5$  mJy

TABLE 1  
TIME RANGES USED TO OBTAIN G12-LIKE POINTS

Start Date	End Date	# of Obs.
50420	50550	27
53820	53850	4

happen to lie almost exactly on the upper G12 track (red line in Figure 9). A fit to these points yields a log slope  $\eta \sim 0.68 \pm 0.35$  (with the intercept at 5.32 where  $L_X \propto L_R^\eta$ ). This is consistent with the slope of the upper G12 track,  $\eta = 0.63$ . However, we note that the uncertainty associated with our measurement is quite large. These points, hereafter referred to as “G12-like” points, also exhibit high  $E_{\text{fold}}$  values while showing  $\Gamma$  values clustered tightly about  $\sim 1.8$ , as typical for a canonical hard state. The G12-like points suggest that as the system declines to lower X-ray luminosities the steady-hard observations exhibit parameter values which are more typical of a canonical BHB hard state.

The second region of interest is the set of points which are a subset of the radio plateau states of GRS1915 which were previously selected for an independent X-ray–radio study by Rushton et al. (2010). We used *RXTE*/*PCA* observations with simultaneous radio data (see Section 2.2) which are time matched within  $\pm 0.5$  days to the times of the their *RXTE*/*ASM* observations (Rushton et al. 2010; private communication). Hereafter, we refer to them as “R10” points. They are repre-

sented by the purple triangles on the upper-half of Figure 9. A fit to the purple triangles in our plot yields a log slope  $\eta \sim 1.12 \pm 0.13$  (with the intercept at -10.28) showing a higher slope with respect to the G12-like points.

In their study Rushton et al. (2010), obtained a log slope  $\eta \sim 1.7$ . Their use of *RXTE*/*ASM* data necessarily limited their computation to an energy band of 2–12 keV and their analysis included both disk and coronal components. Our value is derived using the isolated coronal component luminosity (i.e. removing the contaminated disk contribution), integrated from 1–10 keV. It is therefore more suitable for comparison with the power law dominated BHB hard state luminosities used by Gallo et al. (2012).

In Figure 11 we show the relationship of the radio luminosity and the model parameter  $E_{\text{fold}}$ .  $E_{\text{fold}}$  is the only parameter that displays a simple relationship to the radio luminosity, showing a strong non-linear anti-correlation. This anti-correlation nicely separates the G12-like points (cyan squares) and the R10 points (purple triangles), with the earlier having the highest  $E_{\text{fold}}$  values and the latter having the lowest  $E_{\text{fold}}$  values. The high  $E_{\text{fold}}$  values of the G12-like points, indicates a hotter corona, closer to a canonical hard state. The low  $E_{\text{fold}}$  values displayed by the R10 points and the anti-correlation itself, are still puzzles.

#### 4.6. A possible connection between the accretion disk and the radio jet

In Figure 12 we represent the two regions of different jet activity discussed above, in the context of the relationship between the coronal flux and the inner disk radius. It is interesting to note that both regions of jet activity that display correlations to coronal luminosity occurs when the steady-hard disk has low  $R_{\text{in}}$ . They also appear linked to two tracks in Figure 12. It is also noteworthy that, the black data points in Figure 9, situated in-between the G12-like region and the R10 region and outside the dashed green circle, displays mid-range  $E_{\text{fold}}$  values and forms a track in Figure 12 which exists in the middle of the purple and cyan tracks.

The apparent link of the two jet activity regions (cyan and purple points) to the two tracks does not hold at high  $R_{\text{in}}$ . The extension of cyan and purple points in Figure 12 is very different from the extension of the same in Figure 9. While the cyan and purple points appear fairly organized in both Figures, any possible tracks within the green area in Figure 12 (high  $R_{\text{in}}$ ) are completely mixed when traced back to Figure 9. In summary, we note that while there appears to be a connection between the radio jet and the inner radius of the disk, the radio jet seems to be a function of other parameters which are presently unknown.

## 5. RIGOROUS COMPARISON TO CANONICAL BHB STATES

In their review of BHBs, RM06 define three BHB spectral-timing states: thermal, SPL and hard. The criteria for each are given in their table 2 and are based on the characteristics of the X-ray spectra, power-density spectra (PDS) and quasi-periodic oscillations (QPOs). In this section we explore our observations of GRS1915 within their widely-used state framework.

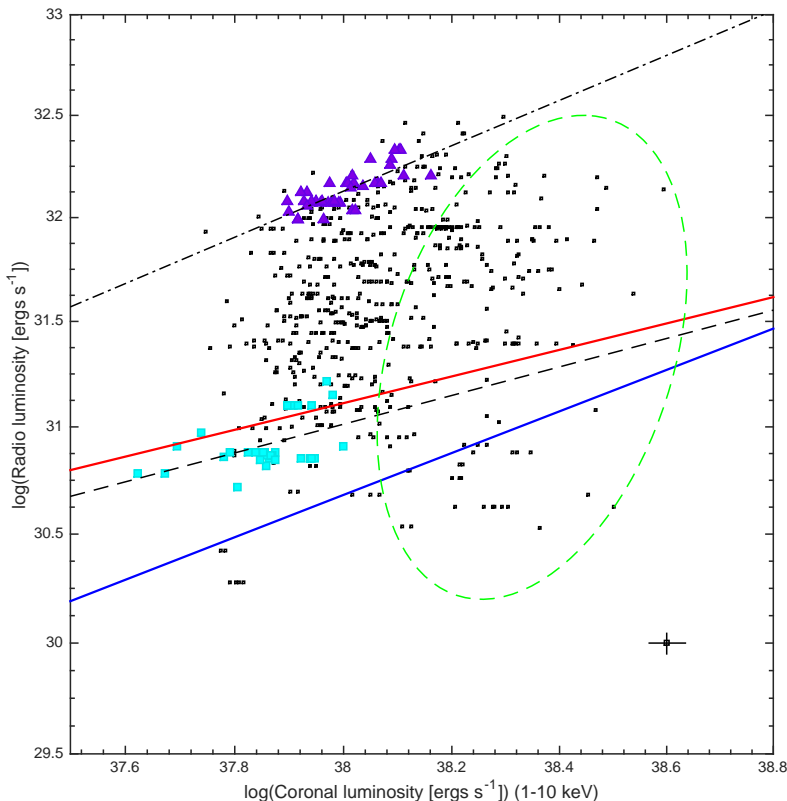


FIG. 9.— Radio versus coronal luminosity. Cyan squares represent the G12-like points on the decline of the steady-hard light-curve dips observed within the time periods specified by Table 1. Purple triangles represent the R10 points. The red and blue lines represent the G12 tracks ( $L_r \propto L_X^\eta$  where  $\eta = 0.63$  and  $0.98$ ). The dashed line represents the fit to the cyan squares ( $\eta \sim 0.68 \pm 0.35$ ) and the dot-dash line represents the fit to the purple triangles ( $\eta \sim 1.12 \pm 0.13$ ). The region encircled by the dashed green line will be explained in Section 4.6.

We took each X-ray observation and its corresponding PDS and matched their parameters to the criteria defining each state. Observations that matched the thermal criteria were represented as red crosses while observations that matched the SPL and hard criteria were represented as green triangles and dark blue squares respectively. The SPL state observations were split into two groups with those displaying low-frequency QPOs (LFQPOs;  $< 30$  Hz) represented by filled-green triangles (referred to as SPL-qpo) and those without LFQPOs marked with open-green triangles (referred to as SPL-noqpo). Observations with parameters that did not fit within the boundaries of the state classifications were marked with black open circles. In addition, any steady-hard observations which did not fit the hard state disk fraction<sup>9</sup> ( $f_{\text{disk}}$ ) constraint of  $f_{\text{disk}} < 20\%$  (see table 2 in RM06), but fit all other hard state criteria were represented as cyan squares. The resulting mapping of these data onto RM06 states is shown in Figure 13, depicting  $R_{\text{in}}$  versus disk luminosity.

A majority of the steady-soft data match either thermal (43 %) or SPL (13 %) states, while the remainder have one or more parameters with values that are outside

<sup>9</sup> Here, to be consistent with RM06, we use the disk fraction calculated using the apparent disk flux divided by the sum of the apparent disk and coronal flux, all in the 2 - 20 keV flux bands.

of the criteria of the three states explored. The thermal states line up nicely, dominating the constant  $R_{\text{in}}$  branch. This is consistent with the observations of canonical BHB thermal states which show  $R_{\text{in}}$  going down to  $R_{\text{ISCO}}$  (e.g. Steiner et al. 2009a).

Among the steady-hard observations, we find a few (0.01 %) that are consistent with the hard state. However, we find that when the disk fraction is neglected, a majority of the steady-hard observations (80 %) are found to match the hard state criteria (cyan points in Figure 13). The higher disk fraction in GRS1915 is a consequence of the unique presence of a hot and bright disk in the steady-hard observations, as determined from our spectral fits. The alignment of the other parameters (rms power, spectral index and QPO behavior) with the well-studied states in many other black-hole systems confirms the posited association between the steady observations of GRS1915 and the canonical black hole states.

When compared, the two groups of SPL observations display several distinct differences in characteristics in addition to LFQPO presence. SPL-noqpo includes the observations that show departure in  $R_{\text{in}}$  (see Section 4.1.1). It also materializes at lower luminosities compared to SPL-qpo as seen clearly in Figure 13. Furthermore, SPL-noqpo displays lower integrated rms power (0.1-10 Hz) and higher scattering fraction ( $f_{\text{sc}}$ )

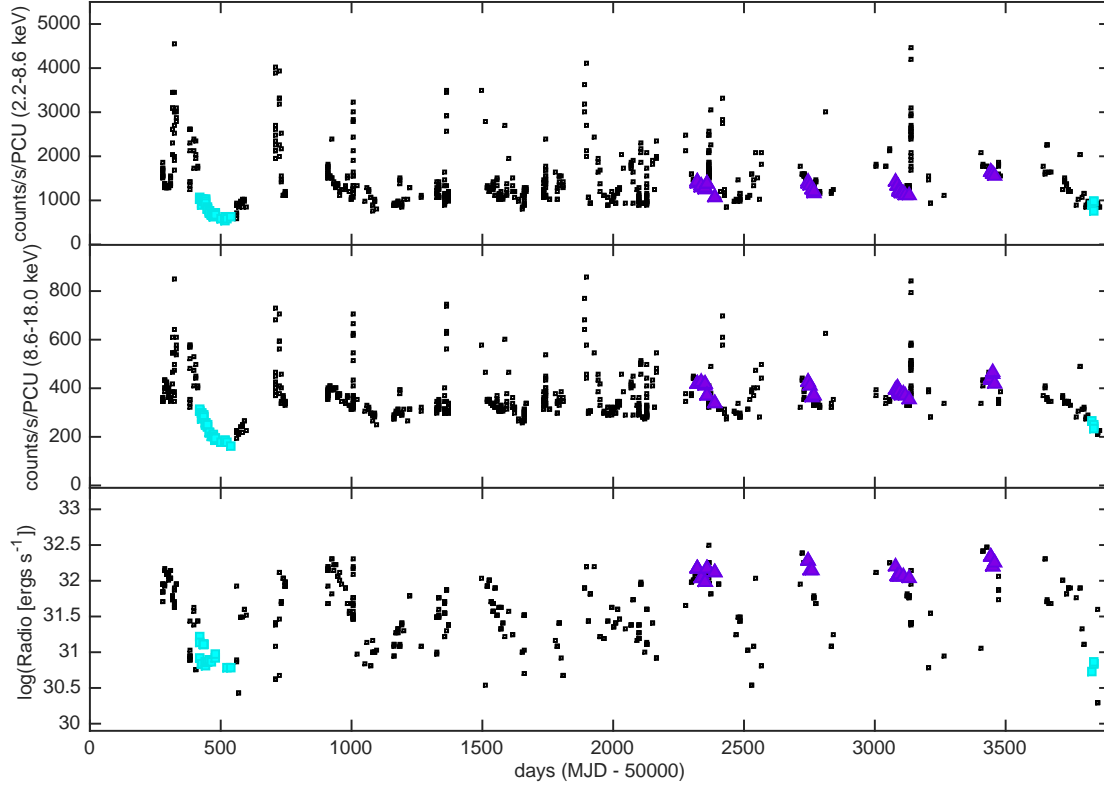


FIG. 10.— X-ray and log(radio) light curves with G12-like points and the R10 points colored in cyan and purple respectively.

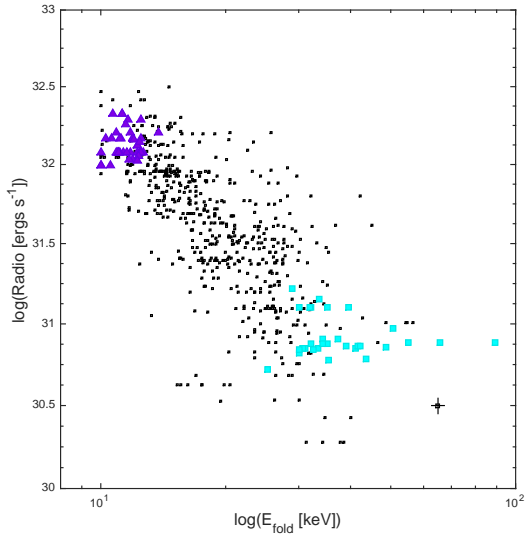


FIG. 11.—  $E_{\text{fold}}$  as a function of radio luminosity. The colors represent the populations described in the caption of Figure 10.

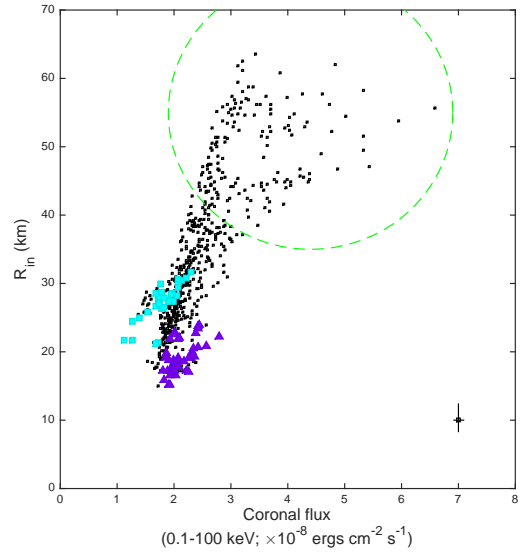


FIG. 12.— The variation of  $R_{\text{in}}$  as function of coronal flux. As in Figure 11, the colored points represent the selections in Figure 10. The dashed green-line roughly outlines the same points as in Figure 9. The apparent link of the two jet activity regions (cyan and purple points) to the two tracks does not hold in this region.

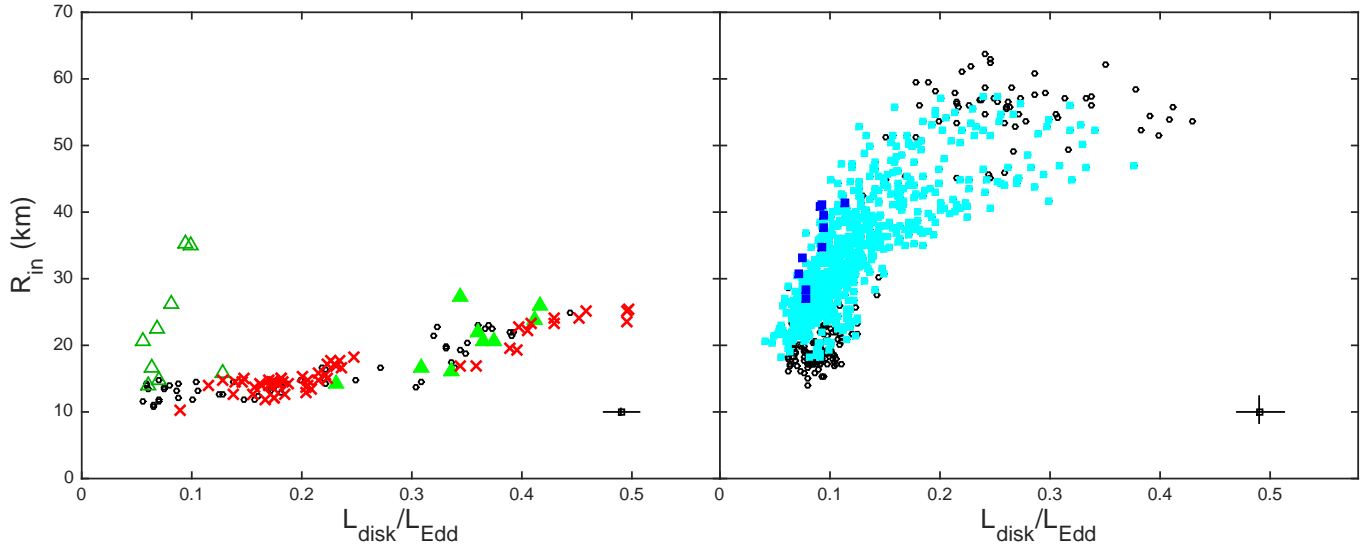


FIG. 13.— **Left:** Steady-soft observations with those matching the thermal (red crosses) and SPL state (green triangles) criteria marked. Filled-green triangles mark SPL state observations with LFQPOs while open-green triangles mark those with no LFQPOs. **Right:** Steady-hard observations with those matching the hard (dark-blue filled squares) state criteria marked. Cyan squares show steady-hard data matching a relaxed definition of the hard state (see text for details). No steady-hard points matched the thermal or SPL state definitions and no steady-soft points matched the hard state definition. Black open circles mark observations which do not fit within the state classifications.

when compared to SPL-qpo.

Figure 14 shows the normalized CD with data points color-coded for states, as described above (see Figure 2). The thermal and the SPL-qpo observations cluster together displaying higher HR1 compared to the SPL-noqpo observations. Remarkably, the locations of the two resultant CD clusters appear to be similar to those of the A and B regions defined for GRS1915’s *variable* observations by Belloni *et al.* (2000) (see their figure 8). While the cluster comprised of the thermal and SPL-qpo observations maps to B, the SPL-noqpo observations appear in a similar location to A. The steady-hard observations map to the location of the C variable state. If such a link exists between the steady observations and the transient A, B and C states, it demonstrates a compelling link between short and long time scales in GRS1915’s phenomenology.

## 6. DISCUSSION

In this section we discuss the confidence in our models and the implications of our results. We first establish our confidence in the models used in this paper by exploring several aspects of their performance. We then move on to discuss the results which they have enabled us to obtain. First we discuss the behavior of the accretion disk in the steady-soft observations. Next, we discuss a magnetically arrested disk as a possible scenario to explain the disk truncation observed in the steady-hard observations. We then discuss the X-ray–radio correlations we observe followed by possible effects due to high spin.

### 6.1. Model confidence

Our adopted spectral models combine the paradigms of BHB accretion research with pragmatic adjustments to gain acceptable model fits. Since the models are not unique, we must evaluate the results on performance is-

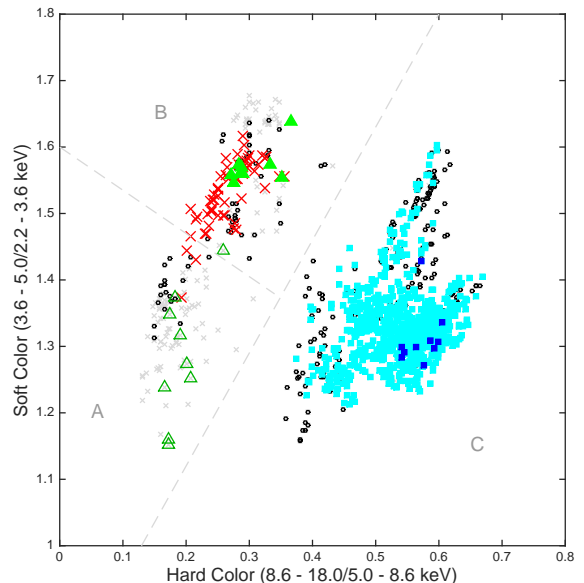


FIG. 14.— The normalized CD, with symbols as defined in Figure 13. Light-grey dashed lines roughly demarcate the regions “A, B and C” regions that govern fast variability cycles in GRS1915 (see also figure 8 in Belloni *et al.* 2000). State assignments appear to map to the A, B and C regions. Light-grey crosses indicate observations that did not satisfy the goodness-of-fit criterion.

sues, e.g. the ability to provide physical parameters that are self-consistent, robust in handling the large range in source luminosity, productive in gaining insights into source behavior and capable of showing correlations with measurements independent of the spectral fits.

As shown in Section 3.2, we used two slightly different



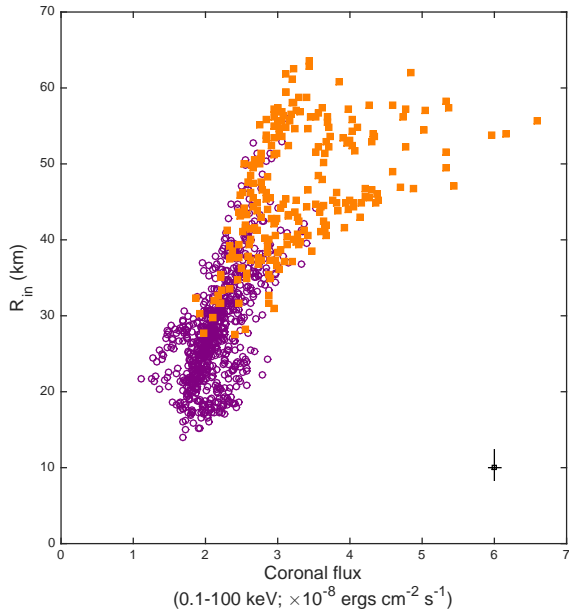


FIG. 15.— Observations with Type 1 (orange squares) and Type 2 (purple circles) LFQPOs represented in the plot of  $R_{\text{in}}$  versus coronal flux. The types are defined within the text.

spectral models to fit the steady-soft and steady-hard observations. In the steady-hard observations we observe that  $R_{\text{in}}$  drops to  $\sim 15$  km when closest to the black hole. This is consistent with the  $R_{\text{in}}$  observed in the steady-soft data showing a self-consistent picture of  $R_{\text{in}}$  across both models.

Our observation of a roughly constant  $R_{\text{in}}$  branch in the steady-soft observations of GRS1915 over a wide range of luminosity, strengthens our confidence in the robustness of our model in handling changes in source luminosity. The minority of steady-soft observations that deviate from the main branch and show increasing  $R_{\text{in}}$  have common properties; they are in the SPL state on the basis of a low disk fraction in energy flux, rather than the alternative path that is based on the presence of LFQPOs.

In order to explore parameter correlations with measurements independent of the fits we turn to timing information within the steady-hard observations. 100 % of the steady-hard power density spectra display a strong LFQPO ( $\sim 0.1 - 10$  Hz). We separate them into two groups based on the shape and maximum frequency of the LFQPO. Type 1 consists of single peak low amplitude higher frequency LFQPOs with no harmonics and Type 2 characterizes high amplitude lower frequency LFQPOs accompanied by one or two harmonics.

In Figure 15 we represent observations corresponding to Type 1 and Type 2 LFQPOs colored in orange and purple respectively, within a plot showing  $R_{\text{in}}$  as a function of coronal flux. The Type 1 and Type 2 LFQPO observations separate to low and high radii respectively. This shows that the timing information is tied to the structure of the inner disk as inferred from spectral results. The correlation of the model-dependent  $R_{\text{in}}$  with independent LFQPO properties bolsters our confidence in our steady-hard model.

We also explored the robustness of the main results (i.e. an approximately constant  $R_{\text{in}}$  branch in the steady-soft observations and a disk truncation in the steady-hard observations) by investigating parameter distribution in other tested models which fell short of our expectations and were not used in our analysis. We derived and compared the apparent  $R_{\text{in}}$  and  $L_{\text{disk}}$  of our SIMPLCUT  $\otimes$  EZDISKBB models with models that used components such as POWERLAW  $\otimes$  HIGHECUT and COMPTT. The  $R_{\text{in}}$  distributions produced by these models were found to reflect our main results for both steady-soft and steady-hard data sets. Such robustness of results, even though these models did not return sufficient good-fits, strengthen our confidence in our SIMPLCUT  $\otimes$  EZDISKBB models.

### 6.2. Behavior of the accretion disk in the steady-soft observations

Tanaka & Lewin (1995) observed for three systems, that  $R_{\text{in}}$  is remarkably constant over a wide range of bolometric disk flux. They associated this constant  $R_{\text{in}}$  with the radius of the innermost stable circular orbit ( $R_{\text{ISCO}}$ ). An alternative way of displaying the same result has been to plot disk luminosity versus temperature which approximately goes as  $L_{\text{disk}} \propto T^4$  for constant  $R_{\text{in}}$  (Gierliński & Done 2004; Kubota & Done 2004; Done et al. 2007). Since then, the stability of  $R_{\text{in}}$  when the system displays a soft state has been observed for many BHB systems and is regarded as a common trait of the soft thermal dominated state of BHBs. The validity of the claim of this stable  $R_{\text{in}}$  as  $R_{\text{ISCO}}$  is bolstered by the many recent and successful spin measurements that are based on this assumption (Shafee et al. 2006; McClintock et al. 2006; Kolehmainen & Done 2010; Steiner et al. 2011, 2012, 2014).

In Figure 5, we observe a similar trait displayed by 96 % of the observations. It serves as a reminder that along with its intense variability, GRS1915 also displays properties similar to canonical BHBs.

Within this roughly constant  $R_{\text{in}}$  branch we note a slight increase in  $R_{\text{in}}$  when luminosity rises above  $0.3 L_{\text{disk}}/L_{\text{Edd}}$ . This increase is manifested in the “spin-droop” found in several black hole systems including GRS1915 itself (e.g., McClintock et al. 2006; Steiner et al. 2010, 2011; McClintock et al. 2014), and may mark the onset of slim-disk effects (Sądowski 2009; Sądowski et al. 2011; though see Straub et al. 2011). The increase in  $R_{\text{in}}$  at high luminosities results in a decrease in the inferred spin value which was apparent in the inconsistency of the two spin measurements for GRS1915 by McClintock et al. (2006) and Middleton et al. (2006) (see McClintock et al. 2006 for details). Considering that the approximately constant  $R_{\text{in}}$  branch also displays nearly constant temperature which also is the highest temperature observed within the steady observations (Figure 6) the increase in  $R_{\text{in}}$  (and corresponding “droop” in spin) might also alternatively be a result of a “local Eddington” effect much like that of the flaring branch of Z-sources (Lin et al. 2009).

### 6.3. A possible magnetic-field controlled truncation in the steady-hard observations

In this section we further discuss the idea presented in Section 4.1.2, namely that global magnetic field properties may be the mechanism distinguishing steady-soft and steady-hard data; and that the magnetic state of the disk may account for its truncation when steady-hard.

Both theory and 3D Magnetohydrodynamical (MHD) simulations have predicted that the accumulation of strong poloidal magnetic field close to the black hole can disrupt the accretion of gas through the disk. As poloidal field builds, magnetic pressure can at some point balance the ram pressure of the accreting gas, halting the flow and producing a truncated inner disk. Originally proposed by Bisnovatyi-Kogan & Ruzmaikin (1974), this theory was refined by Narayan *et al.* (2003) and the effect in question referred to as a Magnetically Arrested Disk (MAD).

The presence of a global magnetic field was also invoked to explain the presence of X-ray QPOs in BHBs (Tagger & Pellat 1999; Varnière *et al.* 2012). Here, magnetized disks were investigated in a theoretical framework known as the Accretion-Ejection Instability (AEI). The degree of disk magnetization was later claimed to be the basis for the different X-ray states in BHBs (Tagger *et al.* 2004), including the “A, B, and C” states that form the basis for fast variability cycles in GRS1915 (see end of Section 5 and also Varnière *et al.* 2011).

When accretion close to a black hole is disrupted by a MAD, it is suggested that matter flows inward in discrete blobs which travel much slower than the free-fall velocity. During this phase almost a significant fraction of the rest mass energy of the gas is expected to be released as heat, radiation and mechanical energy. Simulations have recently shown that MADs are also capable of producing jets efficient at extracting spin energy ( $> 100\%$  efficiency in ideal circumstances which in part requires  $a_* > 0.9$ , Tchekhovskoy *et al.* 2011; McKinney *et al.* 2012).

We note that thus far simulations of MADs have mostly treated accretion disks of substantial thickness, since a thick flow facilitates the trapping of magnetic field lines. They have also been concentrated on systems with low radiative energy loss. More study is needed to assess the importance of MADs in the thin-disk high-spin regime with high radiative losses. We remind the reader that GRS1915 is a system which belongs to the latter regime and therefore our suggestions should be taken with due caution.

Our results show that  $R_{\text{in}}$  increases systematically with increasing disk luminosity and hence the estimated mass accretion rate through the disk. However, if the sampling of time-disparate points at a given disk luminosity suggest the same  $R_{\text{in}}$ , then it would be reasonable to presume that the MAD must reach an equilibrium at a given  $\dot{M}$ , i.e., that B-field losses (reconnection and outflows) must balance the continual inflow of field lines seeded by the global field, so as to hold  $R_{\text{in}}$  steady. In the MAD scenario, the  $R_{\text{in}}-\dot{M}$  correlation further suggests that the global B-field is not random, but is also regulated in some way by accretion, e.g., arising from some type of dynamo in the outer disk. If not, changes in the global field strength would likely destroy the correlation, as we sample dozens of re-formed hard-steady conditions during the 16 years of *RXTE* observations. Additional questions concern the details of magnetic flux accumu-

lation and the effects of disk thickness. Further work is needed to consider these issues and properly assess the MAD as an explanation for hard-steady conditions.

Varnière *et al.* (2011) present another way to classify observations based on the kind of instability that occurs in the disk. This was first developed as a continuation of the extended Magnetic Flood Scenario (Tagger *et al.* 2004; Varnière *et al.* 2007) which has been proposed to explain the overall behavior of the source based on the stored magnetic flux in the inner region of the system. The classification is based on two key parameters; the degree of magnetization of the disk ( $\beta$ ) and the position of the inner edge of the disk ( $\xi_{\text{int}}$ ). From these two parameters they obtain four possible “states” harboring up to two simultaneous instabilities and having quite distinctive timing specificities. Their spectral differences have not been explored in detail but an overall behavior can be deduced from the different instabilities.

The softer states are characterized with a lower magnetization level in the disk, while the harder states tend to have a fully magnetized disk. This clearly separates the behavior of both states even though they can reach similar inner radii. Indeed in the soft, low-magnetization state the instabilities that can occur, such as the magneto-rotational instability (MRI; Balbus & Hawley 1991) and the Rossby Wave Instability (RWI; Tagger & Varnière 2006), both tend to heat up the disk more than the instabilities known to occur in a fully magnetized disk. Using the position of the inner-edge of the disk, the four-state classification separates the softer states further. While the MRI can occur independently of the disk position, the RWI dominates when the inner edge of the disk gets closer to the last stable orbit. This will cause further heating of the inner region of the disk while keeping a relatively stable inner edge. As a consequence of the low magnetization, the softer states will tend to have a more limited coronal emission than the harder states. Using a similar approach as in Varnière & Tagger (2002), we can also infer that the coronal emission will be higher when the RWI is active in the disk; i.e., when the inner edge of the disk is smaller.

Within this framework, the harder states tend to be explained by having a fully magnetized disk, hence the Accretion-Ejection Instability (Tagger & Pellat 1999) causes the transport of angular momentum and the LFQPO. In this scenario (Tagger *et al.* 2004; Varnière *et al.* 2007) the inner edge of the disk is pushed out (as in a MAD) because of the magnetic flux stored inside the inner region. As the stored magnetic flux gets destroyed due to the magnetic flux being transported in by the accretion flow in the disk, the inner edge of the disk moves towards  $R_{\text{ISCO}}$ . This process, depending on the magnetization of the disk, is slow enough for the state to be “steady” during one observation window. This process is also at the origin of the radio emission visible in those states. Once again, depending on whether the inner edge of the disk stays close to the last stable orbit, the RWI will simultaneously occur in the inner region but this time, as shown in Varnière & Tagger (2002), the coronal emission will be higher when the disk is away from its last stable orbit.

While a one-on-one association with the different sub-branches of steady-hard and steady soft is difficult, the level of magnetization in the disk may account for the

behavioral differences we have observed.

#### 6.4. The X-ray-radio correlations of the G12-like and R10 observations within the steady-hard

We find evidence of a (non-linear) X-ray-radio correlation for GRS1915 that occurs during the decline into two luminosity dips in the steady-hard light curves (Figure 10). When examining the coronal parameters of these G12-like points, which are limited to the decline period, we find changes which suggest a move towards more canonical hard state characteristics (Section 4.3). The changes are as follows: (1) While all steady-hard observations show significantly low values of  $E_{\text{fold}}$ , these observations show an increase in  $E_{\text{fold}}$  which corresponds to a decrease in the curvature of the Compton component. This shows a move towards a less curved power law, typical of hard state BHBs. (2) A majority of the steady-hard observations show  $1.4 < \Gamma < 2.1$  with a mean value  $1.69 \pm 0.26$ , which is typical for a hard state. These specific observations occupy a compact spot in the middle of this range and show a much less variability ( $\Gamma = 1.72 \pm 0.09$ ) suggesting a separate population with a more regular power-law index.

Our fit to the G12-like points matches the slope of the upper G12 track (Gallo et al. 2012, see also Gallo et al. 2003, 2006; Corbel et al. 2008) although we note that our uncertainty is large. The changes observed in the coronal parameters within the G12 points increase our confidence that they might map to one of the G12 tracks which are defined using canonical hard state BHBs. Finally, the G12-points lie almost exactly on the upper G12 track (red line in Figure 9) leading us to believe that these might be one and the same.

Our fit to the R10 points obtained using isolated coronal flux (i.e. without the contribution of disk component) produces a log slope  $\eta \sim 1.12 \pm 0.13$ , which is much lower than that observed by Rushton et al. (2010). We find that our value for the slope is consistent with the lower G12 track (blue line in Figure 9). The two slopes observed within the steady-hard observations of GRS1915 is reminiscent of the two slopes observed in the hard state observations of H1743-322 (Coriat et al. 2011).

#### 6.5. Effects due to high spin in the system

One of the most noticeable differences in GRS1915 when compared to canonical BHBs is the unusual curvature observed in the coronal component. Our analyses quantify this as  $E_{\text{fold}}$  values of  $\sim 10$  keV for the steady-soft observations and 10-30 keV for the majority of the steady-hard observations (see Figure 7c). This curvature has been a major source of difficulty in modeling the spectra of this system. We explained earlier using the classical interpretation for Comptonization, that this curvature can be a result of a corona which is intensely cooled by the ample availability of soft photons from the hot inner disk. This leads us to the obvious next question: what causes the disk in GRS1915 to be so hot? The explanation seems to be high spin ( $a_* \geq 0.98$ ; McClintock et al. 2006). The extreme spin, which allows the spacial dimension of  $R_{\text{ISCO}}$  to shrink down to limits smaller than for other known BHBs, could result in the production of a vast number of soft photons that can cool the corona intensely. This will lower the energy of the

coronal electrons inhibiting the upscatter the soft photons to high enough energies to produce the usual power law observed in canonical BHBs.

## 7. SUMMARY

1. The steady state observations of GRS1915 naturally separate into two groups on the CD with a gap in the middle. We label these two groups, steady-soft and steady-hard.
2. The spectral continuum of GRS1915 displays significant curvature of the Compton component ( $E_{\text{fold}} \sim 10$  keV for steady-soft and 10-30 keV for a majority of steady-hard), rendering commonly used models such as POWERLAW or SIMPL ineffective in representing the Comptonization. The new cut-off power-law model SIMPLCUT, describes the curvature well. The extreme curvature suggests significant cooling of the corona in GRS1915.
3. The disk in GRS1915 is significantly hotter than canonical BHB disks. The temperatures of the disk in a majority of the steady-soft and steady-hard observations are  $\sim 2$  keV and  $\sim 1.2$  keV, respectively. Other BHBs show soft and hard observations with typical temperatures of  $\leq 1$  keV and  $\leq 0.5$  keV, respectively.
4. 96% of the steady-soft observations display an almost constant  $R_{\text{in}}$  which is usually observed in canonical soft-state observations of BHBs. However, 4 % of the steady-soft observations show an increase in  $R_{\text{in}}$  at low X-ray luminosity.
5. The steady-hard observations exhibit the presence of a truncated disk with varying  $R_{\text{in}}$ . The minimum  $R_{\text{in}}$  in the steady-hard observations agrees well with the  $R_{\text{in}}$  values for the steady-soft observations (and is therefore close to  $R_{\text{ISCO}}$ ), but increases by a factor of 4 at highest luminosity.
6. A strong correlation is noted between disk and coronal flux in the steady-hard observations. The steady-soft observations show only a very weak correlation with comparatively less coronal flux, suggesting that the two coronae have different origin.
7. A sub-population within the steady-hard observations follows the upper G12 track during the luminosity decline period of two dips in the X-ray light curve ( $50420 < \text{MJD} < 50550$  and  $53820 < \text{MJD} < 53850$ ). GRS1915 shows a shift toward a canonical hard state when dropping down to these low luminosities.
8. The R10 observations display a slope which is consistent with the lower G12 track (0.98).
9. It has been shown earlier that the steady observations of GRS1915 yield spectra that resemble the thermal and hard states. We find evidence to suggest that all three states (thermal, SPL and hard) exists within the steady observations of GRS1915.
10. The locations of the thermal and SPL-qpo observations appear to correspond to the location of variable state B in the CD, while the location of the

SPL-noqpo observations and the steady-hard observations may correspond to the locations of A and C, respectively (Belloni *et al.* 2000). This suggests a link in the phenomenology of GRS1915 between short and long timescales.

#### ACKNOWLEDGMENTS

We acknowledge the use of the it Smithsonian Institution High Performance Cluster (SI/HPC) for spectral fitting. We would also like to thank Jeff Mc-

Clintock, Ramesh Narayan, Javier Garcia and Malgosia Sobolewska for interesting and helpful discussions on the content of this paper. JFS has been supported by NASA Einstein Fellowship grant PF5-160144. SDV acknowledges partial support through a Smithsonian Institution CGPS grant. JR acknowledges financial support from the French Research National Agency: CHAOS project ANR-12-BS05-0009 (<http://www.chaos-project.fr>). PV and JR acknowledge financial support from the UnivEarthS Labex program at Sorbonne Paris Cité (ANR-10-LABX-0023 and ANR-11-IDEX-0005-02).

#### REFERENCES

- Altamirano, D., *et al.* 2011, *ApJ*, 742, L17  
 Arnaud, K. A. 1996, in *Astronomical Society of the Pacific Conference Series*, Vol. 101, *Astronomical Data Analysis Software and Systems V*, ed. G. H. Jacoby & J. Barnes, 17  
 Balbus, S. A., & Hawley, J. F. 1991, *ApJ*, 376, 214  
 Belloni, T., Klein-Wolt, M., Méndez, M., van der Klis, M., & van Paradijs, J. 2000, *A&A*, 355, 271  
 Belloni, T., Méndez, M., King, A. R., van der Klis, M., & van Paradijs, J. 1997a, *ApJ*, 488, L109  
 —. 1997b, *ApJ*, 479, L145  
 Belloni, T. M., Motta, S., & Casella, P. 2013, *The Astronomer's Telegram*, 5417, 1  
 Bisnovatyi-Kogan, G. S., & Ruzmaikin, A. A. 1974, *Ap&SS*, 28, 45  
 Brenneman, L. W., *et al.* 2014, *ApJ*, 788, 61  
 Castro-Tirado, A. J., Brandt, S., & Lund, N. 1992, *IAU Circ.*, 5590, 2  
 Corbel, S., Koerding, E., & Kaaret, P. 2008, *MNRAS*, 389, 1697  
 Corbel, S., Nowak, M. A., Fender, R. P., Tzioumis, A. K., & Markoff, S. 2003, *A&A*, 400, 1007  
 Coriat, M., *et al.* 2011, *MNRAS*, 414, 677  
 Davis, S. W., Done, C., & Blaes, O. M. 2006, *ApJ*, 647, 525  
 Done, C., Gierliński, M., & Kubota, A. 2007, *A&A Rev.*, 15, 1  
 Ebisawa, K. 1991, PhD thesis, Univ. Tokyo  
 Ebisawa, K., *et al.* 1994, *PASJ*, 46, 375  
 Esin, A. A., McClintock, J. E., & Narayan, R. 1997, *ApJ*, 489, 865  
 Fender, R., & Belloni, T. 2004, *ARA&A*, 42, 317  
 Fender, R., *et al.* 1999a, *ApJ*, 519, L165  
 Fender, R. P., Garrington, S. T., McKay, D. J., Muxlow, T. W. B., Pooley, G. G., Spencer, R. E., Stirling, A. M., & Waltman, E. B. 1999b, *MNRAS*, 304, 865  
 Frank, J., King, A., & Raine, D. 1992, *Accretion power in astrophysics*.  
 Gallo, E., Fender, R. P., Miller-Jones, J. C. A., Merloni, A., Jonker, P. G., Heinz, S., Maccarone, T. J., & van der Klis, M. 2006, *MNRAS*, 370, 1351  
 Gallo, E., Fender, R. P., & Pooley, G. G. 2003, *MNRAS*, 344, 60  
 Gallo, E., Miller, B. P., & Fender, R. 2012, *MNRAS*, 423, 590  
 García, J. A., McClintock, J. E., Steiner, J. F., Remillard, R. A., & Grinberg, V. 2014, *ApJ*, 794, 73  
 Gierliński, M., & Done, C. 2004, *MNRAS*, 347, 885  
 Greiner, J., Cuby, J. G., McCaughrean, M. J., Castro-Tirado, A. J., & Mennickent, R. E. 2001, *A&A*, 373, L37  
 Grove, J. E., Johnson, W. N., Kroeger, R. A., McNaron-Brown, K., Skibo, J. G., & Philips, B. F. 1998, *ApJ*, 500, 899  
 Hannikainen, D. C., *et al.* 2005, *A&A*, 435, 995  
 Hua, X.-M., & Titarchuk, L. 1995, *ApJ*, 449, 188  
 Jahoda, K., Markwardt, C. B., Radeva, Y., Rots, A. H., Stark, M. J., Swank, J. H., Strohmayer, T. E., & Zhang, W. 2006, *ApJS*, 163, 401  
 Kitamoto, S., Tsunemi, H., Pedersen, H., Ilovaisky, S. A., & van der Klis, M. 1990, *ApJ*, 361, 590  
 Klein-Wolt, M., Fender, R. P., Pooley, G. G., Belloni, T., Migliari, S., Morgan, E. H., & van der Klis, M. 2002, *MNRAS*, 331, 745  
 Kolehmainen, M., & Done, C. 2010, *MNRAS*, 406, 2206  
 Kotani, T., Ebisawa, K., Dotani, T., Inoue, H., Nagase, F., Tanaka, Y., & Ueda, Y. 2000, *ApJ*, 539, 413  
 Kubota, A., & Done, C. 2004, *MNRAS*, 353, 980  
 Laor, A. 1991, *ApJ*, 376, 90  
 Lee, J. C., Reynolds, C. S., Remillard, R., Schulz, N. S., Blackman, E. G., & Fabian, A. C. 2002, *ApJ*, 567, 1102  
 Lin, D., Remillard, R. A., & Homan, J. 2007, *ApJ*, 667, 1073  
 —. 2009, *ApJ*, 696, 1257  
 Makishima, K., Maejima, Y., Mitsuda, K., Bradt, H. V., Remillard, R. A., Tuohy, I. R., Hoshi, R., & Nakagawa, M. 1986, *ApJ*, 308, 635  
 Makishima, K., *et al.* 2008, *PASJ*, 60, 585  
 Markwardt, C. 2012  
 McClintock, J. E., *et al.* 2001, *ApJ*, 555, 477  
 McClintock, J. E., Narayan, R., & Steiner, J. F. 2014, *Space Sci. Rev.*, 183, 295  
 McClintock, J. E., & Remillard, R. A. 2006, *Black hole binaries*, ed. W. H. G. Lewin & M. van der Klis, 157–213  
 McClintock, J. E., Shafee, R., Narayan, R., Remillard, R. A., Davis, S. W., & Li, L.-X. 2006, *ApJ*, 652, 518  
 McKinney, J. C., Tchekhovskoy, A., & Blandford, R. D. 2012, *MNRAS*, 423, 3083  
 Middleton, M., Done, C., Gierliński, M., & Davis, S. W. 2006, *MNRAS*, 373, 1004  
 Miller, J. M., Homan, J., & Miniutti, G. 2006, *ApJ*, 652, L113  
 Miller, J. M., & Rykoff, E. 2007, *The Astronomer's Telegram*, 1066, 1  
 Mirabel, I. F., & Rodríguez, L. F. 1994, *Nature*, 371, 46  
 Mitsuda, K., *et al.* 1984, *PASJ*, 36, 741  
 Munro, M. P., Morgan, E. H., & Remillard, R. A. 1999, *ApJ*, 527, 321  
 Munro, M. P., Remillard, R. A., & Chakrabarty, D. 2002, *ApJ*, 568, L35  
 Munro, M. P., Remillard, R. A., Morgan, E. H., Waltman, E. B., Dhawan, V., Hjellming, R. M., & Pooley, G. 2001, *ApJ*, 556, 515  
 Narayan, R., Igumenshchev, I. V., & Abramowicz, M. A. 2003, *PASJ*, 55, L69  
 Neilsen, J., & Lee, J. C. 2009, *Nature*, 458, 481  
 Neilsen, J., Remillard, R. A., & Lee, J. C. 2011, *ApJ*, 737, 69  
 Pooley, G. G., & Fender, R. P. 1997, *MNRAS*, 292, 925  
 Poutanen, J. 1999, *Accretion disc corona models and X/γ-ray spectra of accreting black holes*, ed. M. A. Abramowicz, G. Björnsson, & J. E. Pringle, *Cambridge Contemporary Astrophysics*, CUP, 1998, 100  
 Prat, L., Rodríguez, J., & Pooley, G. G. 2010, *ApJ*, 717, 1222  
 Reid, M. J., McClintock, J. E., Steiner, J. F., Steeghs, D., Remillard, R. A., Dhawan, V., & Narayan, R. 2014, *ApJ*, 796, 2  
 Remillard, R. A., & McClintock, J. E. 2006, *ARA&A*, 44, 49  
 Rodríguez, J., *et al.* 2008, *ApJ*, 675, 1449  
 Rushton, A., Spencer, R., Fender, R., & Pooley, G. 2010, *A&A*, 524, A29  
 Sądowski, A. 2009, *ApJS*, 183, 171  
 Sądowski, A., Abramowicz, M., Bursa, M., Kluźniak, W., Lasota, J.-P., & Różańska, A. 2011, *A&A*, 527, A17  
 Shafee, R., McClintock, J. E., Narayan, R., Davis, S. W., Li, L.-X., & Remillard, R. A. 2006, *ApJ*, 636, L113  
 Shidatsu, M., *et al.* 2011, *PASJ*, 63, 785  
 Shimura, T., & Takahara, F. 1995, *ApJ*, 445, 780  
 Sobczak, G. J., McClintock, J. E., Remillard, R. A., Bailyn, C. D., & Orosz, J. A. 1999, *ApJ*, 520, 776  
 Sobczak, G. J., McClintock, J. E., Remillard, R. A., Cui, W., Levine, A. M., Morgan, E. H., Orosz, J. A., & Bailyn, C. D. 2000, *ApJ*, 544, 993

- Steiner, J. F., McClintock, J. E., Orosz, J. A., Remillard, R. A., Bailyn, C. D., Kolehmainen, M., & Straub, O. 2014, ArXiv e-prints
- Steiner, J. F., McClintock, J. E., & Reid, M. J. 2012, *ApJ*, 745, L7
- Steiner, J. F., McClintock, J. E., Remillard, R. A., Gou, L., Yamada, S., & Narayan, R. 2010, *ApJ*, 718, L117
- Steiner, J. F., McClintock, J. E., Remillard, R. A., Narayan, R., & Gou, L. 2009a, *ApJ*, 701, L83
- Steiner, J. F., Narayan, R., McClintock, J. E., & Ebisawa, K. 2009b, *PASP*, 121, 1279
- Steiner, J. F., et al. 2011, *MNRAS*, 416, 941
- Straub, O., et al. 2011, *A&A*, 533, A67
- Tagger, M., & Pellat, R. 1999, *A&A*, 349, 1003
- Tagger, M., & Varnière, P. 2006, *ApJ*, 652, 1457
- Tagger, M., Varnière, P., Rodriguez, J., & Pellat, R. 2004, *ApJ*, 607, 410
- Takizawa, M. 1991, Master's thesis, MSc. thesis. Univ. Tokyo (1991), 173 pages
- Tanaka, Y., & Lewin, W. H. G. 1995, *X-ray Binaries*, 126
- Tchekhovskoy, A., Narayan, R., & McKinney, J. C. 2011, *MNRAS*, 418, L79
- Terada, K., Kitamoto, S., Negoro, H., & Iga, S. 2002, *PASJ*, 54, 609
- Titarchuk, L. 1994, *ApJ*, 434, 570
- Titarchuk, L., & Lyubarskij, Y. 1995, *ApJ*, 450, 876
- Titarchuk, L., & Seifina, E. 2009, *ApJ*, 706, 1463
- Ueda, Y., Inoue, H., Tanaka, Y., Ebisawa, K., Nagase, F., Kotani, T., & Gehrels, N. 1998, *ApJ*, 492, 782
- Varnière, P., & Tagger, M. 2002, *A&A*, 394, 329
- Varnière, P., Tagger, M., & Rodriguez, J. 2011, *A&A*, 525, A87
- Varnière, P., Tagger, M., & Rodriguez, J. 2012, *A&A*, 545, A40
- Varnière, P., Tagger, M., Rodriguez, J., & Cadolle Bel, M. 2007, in *SF2A-2007: Proceedings of the Annual meeting of the French Society of Astronomy and Astrophysics*, ed. J. Bouvier, A. Chalabaev, & C. Charbonnel, 221
- Wilms, J., Allen, A., & McCray, R. 2000, *ApJ*, 542, 914
- Wilson-Hodge, C. A., et al. 2011, *ApJ*, 727, L40
- Zdziarski, A. A., Grove, J. E., Poutanen, J., Rao, A. R., & Vadawale, S. V. 2001, *ApJ*, 554, L45
- Zimmerman, E. R., Narayan, R., McClintock, J. E., & Miller, J. M. 2005, *ApJ*, 618, 832

TABLE 2 Observation list

Reference <sup>1</sup>	MJD <sup>2</sup>	MET <sup>3</sup> Start	MET <sup>3</sup> Stop	Exposure (s)	Type	Spectral fit <sup>4</sup>
0829_a	50182.71652	71686083	71688931	2848	soft	yes
0829_b	50182.78550	71691827	71695107	3280	soft	yes
0829_c	50182.85309	71697587	71701027	3440	soft	yes
0837a_a	50190.58735	72366723	72368371	1648	soft	no
0837a_b	50190.65800	72372739	72374563	1824	soft	yes
0837b_a	50190.71884	72378019	72379795	1776	soft	no
0837c_a	50190.77772	72383379	72384611	1232	soft	no
0840_a	50193.44735	72613923	72615379	1456	soft	no
0840_b	50193.51680	72619667	72621635	1968	soft	no
0840_c	50193.58513	72625427	72627683	2256	soft	no
0840_d	50193.65430	72631187	72633875	2688	soft	yes
0849_a	50202.86522	73426547	73430163	3616	soft	no
0849_b	50202.93217	73432355	73435923	3568	soft	no
0849_c	50203.00522	73439267	73441635	2368	soft	yes
0855_a	50208.60374	73922435	73925891	3456	soft	no
0855_b	50208.65559	73928147	73929139	992	soft	no
0855_c	50208.67402	73929283	73931187	1904	soft	no
0855_d	50208.73328	73933907	73936803	2896	soft	no
0864_a	50217.67559	74706275	74709667	3392	soft	no
0879_a	50232.53430	75991427	75992099	672	soft	yes
0879_b	50232.55013	75992243	75994019	1776	soft	yes
0879_c	50232.60615	75997187	75998755	1568	soft	yes
0879_d	50232.62495	75998899	76000291	1392	soft	yes
0881_a	50234.48347	76159571	76160771	1200	soft	yes
0881_b	50234.54717	76164339	76167011	2672	soft	yes
0881_c	50234.61634	76170099	76173203	3104	soft	yes
0881_d	50234.68504	76175859	76179315	3456	soft	yes
0886_a	50239.48884	76592131	76593139	1008	soft	yes
0886_b	50239.55032	76596579	76599315	2736	soft	yes
0886_c	50239.61995	76602339	76605587	3248	soft	yes
0886_d	50239.68782	76608115	76611539	3424	soft	yes
0888_b	50241.48309	76763683	76766195	2512	soft	yes
0910a_a	50263.57041	78671523	78675043	3520	soft	no
0910b_a	50263.70513	78683283	78686563	3280	soft	no
0910c_a	50263.84374	78695827	78697971	2144	soft	no
0914a_a	50267.37245	79000067	79003491	3424	soft	yes
0914b_a	50267.50300	79011587	79014531	2944	soft	yes
0922a_a	50275.09309	79668579	79669107	528	hard	yes
0922a_b	50275.11550	79670019	79671539	1520	hard	yes
0922b_a	50275.24319	79680099	79683523	3424	hard	yes
0922c_a	50275.37661	79691619	79695059	3440	hard	yes
0925_a	50278.50976	79962483	79965603	3120	hard	yes
0925_b	50278.57819	79968227	79971683	3456	hard	yes
0925_c	50278.64708	79974355	79977459	3104	hard	yes
0927_a	50280.18458	80107475	80110019	2544	hard	yes
0927_b	50280.24606	80112339	80115779	3440	hard	yes
0927_c	50280.30939	80118099	80120963	2864	hard	yes
0927_d	50280.36485	80123859	80124787	928	hard	yes
0930_a	50283.51365	80394707	80398051	3344	hard	yes
0930_b	50283.58143	80400515	80403955	3440	hard	yes
0930_c	50283.64809	80406275	80409715	3440	hard	yes
0934_a	50287.45013	80735219	80737763	2544	hard	yes
0934_b	50287.51680	80740547	80743955	3408	hard	yes
0934_c	50287.58365	80746307	80749747	3440	hard	yes
0937_a	50290.59106	81006659	81009075	2416	hard	yes
0937_b	50290.65161	81011379	81014819	3440	hard	yes
0937_c	50290.71828	81017139	81020579	3440	hard	yes
0940_a	50293.78698	81282291	81285699	3408	hard	yes
0940_b	50293.85356	81288035	81291459	3424	hard	yes
0940_c	50293.91513	81293795	81296339	2544	hard	yes
0945_a	50298.53976	81694419	81694851	432	hard	yes
0945_b	50298.58921	81697187	81700627	3440	hard	yes
0945_c	50298.65587	81702947	81706387	3440	hard	yes
0945_d	50298.72263	81708707	81712163	3456	hard	yes
0948_a	50301.31856	81933523	81935923	2400	hard	yes
0948_b	50301.38735	81939219	81942115	2896	hard	yes
0948_c	50301.45578	81944979	81948179	3200	hard	yes
0952_a	50305.38976	82285043	82287907	2864	hard	yes
0952_b	50305.45911	82290755	82294179	3424	hard	yes
0952_c	50305.52680	82296515	82300115	3600	hard	yes
0956_a	50309.53013	82642419	82645987	3568	hard	yes
0956_b	50309.59680	82648179	82651747	3568	hard	yes

Continued on next page

TABLE 2 – continued

Reference <sup>1</sup>	MJD <sup>2</sup>	MET <sup>3</sup> Start	MET <sup>3</sup> Stop	Exposure (s)	Type	Spectral fit <sup>4</sup>
0956_c	50309.66717	82654547	82657539	2992	hard	yes
0960_a	50313.33337	82971059	82974547	3488	hard	yes
0960_b	50313.39995	82976803	82980307	3504	hard	yes
0960_c	50313.46680	82982563	82986099	3536	hard	yes
0962_a	50315.33874	83144675	83147459	2784	hard	yes
0962_b	50315.40124	83149715	83153219	3504	hard	yes
0962_d	50315.48504	83158435	83158979	544	hard	yes
0967_a	50320.21013	83565747	83568163	2416	hard	yes
0967_b	50320.27059	83570435	83573923	3488	hard	yes
0967_c	50320.33735	83576195	83579699	3504	hard	yes
0971_a	50324.48726	83936019	83936979	960	hard	yes
0971_c	50324.60985	83945683	83948499	2816	hard	yes
0973_a	50326.34300	84095331	84098339	3008	hard	yes
0973_b	50326.40717	84100659	84104099	3440	hard	yes
0973_c	50326.46143	84106483	84107651	1168	hard	yes
0980_a	50333.75856	84737027	84738051	1024	hard	yes
0980_b	50333.80856	84741235	84742483	1248	hard	yes
0980_c	50333.82430	84742627	84743811	1184	hard	yes
0980_e	50333.94467	84751907	84755331	3424	hard	yes
1026a_a	50379.17106	88659459	88662899	3440	hard	yes
1026a_b	50379.23772	88665219	88668659	3440	hard	yes
1026b_a	50379.50985	88689203	88691699	2496	hard	yes
1026b_b	50379.57735	88695107	88697459	2352	hard	yes
1026b_c	50379.64569	88701155	88703219	2064	hard	yes
1026b_d	50379.71374	88707155	88708979	1824	hard	yes
1032_a	50385.51254	89207779	89210387	2608	hard	yes
1032_b	50385.57967	89213619	89216147	2528	hard	yes
1032_c	50385.64671	89219443	89221907	2464	hard	yes
1032_d	50385.71347	89225203	89227683	2480	hard	yes
1041_a	50394.25171	89962931	89965363	2432	hard	yes
1041_b	50394.31226	89967635	89971123	3488	hard	yes
1048a_a	50401.11189	90555459	90558275	2816	hard	yes
1048b_a	50401.63782	90601571	90603043	1472	hard	yes
1048b_b	50401.66124	90603635	90605027	1392	hard	yes
1048b_c	50401.70319	90607299	90608611	1312	hard	yes
1062_a	50415.19124	91771539	91775107	3568	hard	yes
1062_b	50415.25078	91777635	91779299	1664	hard	yes
1069_a	50421.99597	92359523	92362979	3456	hard	yes
1069_b	50422.06235	92365235	92368739	3504	hard	yes
1069_c	50422.12559	92370995	92373907	2912	hard	yes
1075_a	50428.78587	92947299	92948499	1200	hard	yes
1075_b	50428.81050	92949283	92950771	1488	hard	yes
1075_c	50428.86569	92953059	92956531	3472	hard	yes
1075_d	50428.92865	92958819	92961651	2832	hard	yes
1083_a	50436.67522	93628307	93630771	2464	hard	yes
1083_b	50436.72337	93633107	93634291	1184	hard	yes
1083_c	50436.74402	93634435	93636531	2096	hard	yes
1083_d	50436.79226	93638867	93640435	1568	hard	yes
1083_e	50436.81291	93640579	93642291	1712	hard	yes
1088_a	50441.93448	94082643	94085235	2592	hard	yes
1088_b	50442.00171	94088387	94091107	2720	hard	yes
1088_c	50442.05652	94094147	94094819	672	hard	yes
1089_a	50442.13911	94099907	94103331	3424	hard	yes
1095_a	50448.28976	94632531	94633539	1008	hard	yes
1095_b	50448.34217	94635827	94639299	3472	hard	yes
1095_c	50448.40911	94641635	94645059	3424	hard	yes
1103_a	50456.01097	95298595	95301699	3104	hard	yes
1103_b	50456.07893	95304275	95307763	3488	hard	yes
1103_c	50456.14569	95310035	95313539	3504	hard	yes
1109_a	50462.08272	95823011	95826483	3472	hard	yes
1118_a	50471.08921	96601155	96604659	3504	hard	yes
1118_c	50471.16967	96609283	96610435	1152	hard	yes
1118_d	50471.22698	96613427	96616195	2768	hard	yes
1124_b	50477.95948	97194755	97198243	3488	hard	yes
1124_c	50478.02226	97200515	97203331	2816	hard	yes
1124_d	50478.04291	97203411	97204003	592	hard	yes
1127_a	50480.89754	97448931	97451763	2832	hard	yes
1127_b	50480.96069	97454083	97457523	3440	hard	yes
1127_c	50481.02754	97459843	97463315	3472	hard	yes
1148_a	50501.90309	99263667	99266787	3120	hard	yes
1159_a	50512.90911	100214403	100217891	3488	hard	yes

Continued on next page

TABLE 2 – continued

Reference <sup>1</sup>	MJD <sup>2</sup>	MET <sup>3</sup> Start	MET <sup>3</sup> Stop	Exposure (s)	Type	Spectral fit <sup>4</sup>
1164_c	50517.17884	100584531	100585571	1040	hard	yes
1172_a	50524.93069	101254179	101255443	1264	hard	yes
1181_a	50534.92356	102116579	102119811	3232	hard	yes
1204_c	50557.59309	104075683	104078003	2320	hard	yes
1208_a	50561.14226	104382467	104384515	2048	hard	yes
1208_c	50561.21235	104388819	104390275	1456	hard	yes
1210_a	50563.59837	104594611	104596787	2176	hard	yes
1210_b	50563.66467	104600019	104602835	2816	hard	yes
1210_e	50563.85995	104617299	104619299	2000	hard	yes
1215_a	50568.94865	105057299	105058627	1328	hard	yes
1216_a	50569.46171	105101411	105103171	1760	hard	yes
1223_a	50576.68615	105725523	105727443	1920	hard	yes
1230b_a	50583.22624	106290995	106292099	1104	hard	yes
1230c_c	50583.56208	106320115	106321011	896	hard	yes
1230c_d	50583.61013	106323283	106326147	2864	hard	yes
1230c_f	50583.74708	106334803	106338291	3488	hard	yes
1236_a	50589.49689	106832819	106833843	1024	hard	yes
1236_b	50589.54884	106836163	106839475	3312	hard	yes
1243_a	50596.20245	107412435	107412947	512	hard	yes
1293a_a	50646.31717	111741539	111743667	2128	soft	yes
1293b_a	50646.39180	111748675	111749427	752	soft	yes
1293b_b	50646.44448	111751987	111755219	3232	soft	yes
1293b_c	50646.51032	111757763	111760819	3056	soft	no
1293b_d	50646.56754	111763523	111764947	1424	soft	no
1296_a	50649.44328	112011379	112014019	2640	soft	no
1296_b	50649.51171	112017155	112020067	2912	soft	no
1301_a	50654.04717	112408787	112412163	3376	soft	no
1301_c	50654.12217	112415987	112417923	1936	soft	no
1305_a	50658.52263	112796147	112798163	2016	soft	no
1355a_a	50708.07152	117077411	117078947	1536	hard	yes
1355a_j	50708.60735	117122915	117126035	3120	hard	yes
1355b_a	50708.67411	117128691	117131795	3104	hard	yes
1355b_b	50708.74069	117134435	117137555	3120	hard	yes
1355b_c	50708.80569	117139907	117143315	3408	hard	yes
1355b_d	50708.87235	117145667	117149075	3408	hard	yes
1355b_e	50708.93902	117151427	117154835	3408	hard	yes
1355b_f	50708.99856	117157299	117159251	1952	hard	yes
1356_e	50709.40587	117191747	117195187	3440	hard	yes
1356_f	50709.47513	117197955	117200947	2992	hard	yes
1356_g	50709.54097	117203571	117206707	3136	hard	yes
1357_a	50710.00680	117244995	117245779	784	hard	yes
1367_a	50720.61022	118159827	118163219	3392	hard	yes
1371_a	50724.86309	118528723	118529219	496	hard	yes
1371_c	50724.99809	118540051	118541219	1168	hard	yes
1373_a	50726.35809	118657443	118658835	1392	hard	yes
1374_a	50727.49513	118755955	118756803	848	hard	yes
1374_b	50727.54606	118758995	118762563	3568	hard	yes
1375_a	50728.42809	118836467	118837507	1040	hard	yes
1375_b	50728.47976	118839699	118843203	3504	hard	yes
1376_a	50729.34772	118914675	118918211	3536	hard	yes
1376_b	50729.40800	118920899	118922403	1504	hard	yes
1377_a	50730.41504	119006899	119010419	3520	hard	yes
1382_a	50735.55828	119452067	119454003	1936	hard	yes
1384_a	50737.42208	119612547	119615587	3040	hard	yes
1384_b	50737.48847	119618739	119620867	2128	hard	yes
1390_a	50743.30134	120121427	120122643	1216	hard	yes
1390_b	50743.35615	120125139	120128403	3264	hard	yes
1390_c	50743.42532	120131331	120134163	2832	hard	yes
1390_d	50743.49365	120137443	120139859	2416	hard	yes
1393_a	50746.28958	120378531	120381907	3376	hard	yes
1393_b	50746.35763	120384531	120387667	3136	hard	yes
1393_c	50746.42634	120390643	120393427	2784	hard	yes
1393_d	50746.49411	120396595	120399187	2592	hard	yes
1393_e	50746.56319	120402771	120404947	2176	hard	yes
1393_f	50746.62745	120408643	120410179	1536	hard	yes
1403_b	50756.48384	121260755	121261251	496	soft	no
1410_b	50763.29541	121847795	121851251	3456	soft	no
1416_a	50769.23985	122362179	122364067	1888	soft	no
1416_b	50769.29939	122366707	122369827	3120	soft	no
1416_c	50769.36606	122372467	122375587	3120	soft	no
1421_a	50774.23782	122793715	122796179	2464	soft	no

Continued on next page



TABLE 2 – continued

Reference <sup>1</sup>	MJD <sup>2</sup>	MET <sup>3</sup> Start	MET <sup>3</sup> Stop	Exposure (s)	Type	Spectral fit <sup>4</sup>
1421_b	50774.30152	122798963	122801939	2976	soft	no
1421_c	50774.36819	122804723	122807699	2976	soft	no
1429_a	50782.03022	123466995	123469427	2432	soft	no
1438_a	50791.18541	124258435	124260003	1568	soft	no
1438_b	50791.23208	124262259	124264243	1984	soft	no
1438_c	50791.24967	124264387	124265155	768	soft	no
1483_a	50836.92745	128210739	128211923	1184	soft	yes
1483_b	50836.98439	128214947	128217555	2608	soft	yes
1486_a	50839.78476	128457491	128458915	1424	soft	yes
1486_b	50839.85374	128463267	128465059	1792	soft	yes
1490_a	50843.12643	128745187	128748659	3472	soft	yes
1490_b	50843.19226	128751827	128753395	1568	soft	yes
1494_a	50847.71708	129142771	129144339	1568	soft	yes
1494_b	50847.74143	129145123	129146195	1072	soft	yes
1494_c	50847.79430	129148483	129151971	3488	soft	yes
1498_a	50851.12569	129437267	129438851	1584	soft	no
1498_b	50851.14245	129438995	129440019	1024	soft	no
1498_c	50851.20013	129443203	129445779	2576	soft	no
1502_b	50855.20097	129788867	129791459	2592	soft	no
1503a_a	50856.06485	129863267	129866339	3072	soft	no
1503b_a	50856.79615	129926259	129929715	3456	soft	no
1503b_b	50856.85059	129932019	129933363	1344	soft	no
1504_a	50857.01337	129946499	129947011	512	soft	yes
1504_b	50857.06467	129949603	129952771	3168	soft	yes
1506_a	50859.00782	130118307	130119843	1536	soft	no
1506_b	50859.06448	130122339	130125603	3264	soft	no
1507_a	50860.87087	130279299	130280787	1488	soft	no
1507_c	50860.99745	130289267	130292691	3424	soft	no
1507_d	50861.06522	130295203	130298467	3264	soft	no
1508_a	50861.79504	130358451	130361331	2880	soft	no
1508_b	50861.86143	130364147	130367107	2960	soft	yes
1508_c	50861.92948	130369907	130373107	3200	soft	yes
1508_d	50861.99772	130375667	130379139	3472	soft	yes
1508_e	50862.05958	130381667	130383827	2160	soft	yes
1510_a	50862.99865	130462195	130465571	3376	soft	no
1510_b	50863.06597	130468067	130471331	3264	soft	yes
1510_c	50863.13402	130474067	130477091	3024	soft	yes
1510_d	50863.20171	130480003	130482851	2848	soft	yes
1511a_a	50864.87059	130624931	130626307	1376	soft	no
1511b_a	50864.93754	130630227	130632579	2352	soft	no
1518_a	50871.80374	131223907	131225379	1472	soft	yes
1518_b	50871.86495	131228435	131231427	2992	soft	yes
1529_a	50882.86939	132179075	132182355	3280	soft	no
1529_b	50882.92532	132184787	132186307	1520	soft	no
1534_a	50887.07208	132542083	132545571	3488	soft	yes
1534_b	50887.12597	132547843	132549123	1280	soft	yes
1542_a	50895.88597	133304451	133306243	1792	soft	yes
1542_b	50895.94254	133308467	133312003	3536	soft	yes
1548_a	50901.68124	133804675	133807443	2768	soft	yes
1554_a	50907.74495	134328259	134331667	3408	hard	yes
1554_b	50907.81115	134333987	134337379	3392	hard	yes
1554_c	50907.87874	134339859	134343187	3328	hard	yes
1554_d	50907.94754	134345987	134348947	2960	hard	yes
1554_e	50908.01522	134351923	134354707	2784	hard	yes
1554_f	50908.08097	134358099	134359891	1792	hard	yes
1556_a	50909.88874	134514339	134516035	1696	hard	yes
1556_b	50909.94226	134518611	134521011	2400	hard	yes
1559_a	50912.89152	134773955	134775299	1344	hard	yes
1559_b	50912.94782	134777923	134781059	3136	hard	yes
1560_a	50913.01726	134784163	134786819	2656	hard	yes
1561_a	50914.39967	134904387	134905475	1088	hard	yes
1561_b	50914.41976	134905619	134907715	2096	hard	yes
1570_a	50923.28161	135670611	135674051	3440	hard	yes
1572_a	50925.89374	135897315	135898723	1408	hard	yes
1572_b	50925.94680	135901059	135904147	3088	hard	yes
1578_a	50931.68763	136397811	136399411	1600	hard	yes
1578_b	50931.75809	136403907	136405491	1584	hard	yes
1585_a	50938.90059	137021443	137022179	736	hard	yes
1585_b	50938.95541	137025155	137027939	2784	hard	yes
1591_a	50944.95967	137544051	137546579	2528	hard	yes
1592a_a	50945.02976	137550403	137552339	1936	hard	yes

Continued on next page

TABLE 2 – continued

Reference <sup>1</sup>	MJD <sup>2</sup>	MET <sup>3</sup> Start	MET <sup>3</sup> Stop	Exposure (s)	Type	Spectral fit <sup>4</sup>
1592b_a	50945.09893	137556595	137558099	1504	hard	yes
1592c_a	50945.16671	137562547	137563859	1312	hard	yes
1599_a	50952.62217	138205603	138209107	3504	hard	yes
1604_a	50957.82606	138655523	138658419	2896	hard	yes
1611_a	50964.81948	139260323	139262083	1760	hard	yes
1622_a	50975.35041	140170067	140172083	2016	hard	yes
1622_b	50975.41939	140176243	140177827	1584	hard	yes
1622_c	50975.48606	140181587	140184003	2416	hard	yes
1627_a	50980.77097	140638723	140640099	1376	hard	yes
1627_b	50980.82578	140642435	140645859	3424	hard	yes
1638a_a	50991.62735	141575651	141579155	3504	hard	yes
1638b_a	50991.70115	141582643	141584915	2272	hard	yes
1649a_a	51002.17930	142488675	142489507	832	hard	yes
1649b_a	51002.21689	142491827	142492851	1024	hard	yes
1649b_b	51002.44291	142511187	142512547	1360	hard	yes
1650a_a	51003.17902	142575011	142575923	912	hard	yes
1650b_a	51003.21726	142578227	142579315	1088	hard	yes
1650b_b	51003.44300	142597587	142598963	1376	hard	yes
1651a_a	51004.17958	142661491	142662339	848	hard	yes
1651b_g	51004.42624	142681907	142684547	2640	hard	yes
1651b_h	51004.44717	142684691	142685379	688	hard	yes
1651b_i	51004.49198	142687667	142690147	2480	hard	yes
1652_a	51005.24597	142753603	142754499	896	hard	yes
1652_b	51005.28689	142756787	142758387	1600	hard	yes
1652_c	51005.31226	142759299	142760259	960	hard	yes
1652_d	51005.36439	142762547	142766019	3472	hard	yes
1652_e	51005.43106	142768307	142771779	3472	hard	yes
1652_f	51005.49772	142774067	142777539	3472	hard	yes
1653a_a	51006.17847	142834099	142835139	1040	hard	yes
1653b_a	51006.21828	142837475	142838643	1168	hard	yes
1653b_b	51006.24495	142839827	142840899	1072	hard	yes
1653b_c	51006.28698	142843187	142844803	1616	hard	yes
1653b_d	51006.31161	142845587	142846659	1072	hard	yes
1653b_e	51006.36439	142848947	142852419	3472	hard	yes
1653b_g	51006.49161	142860467	142862883	2416	hard	yes
1655a_a	51008.90671	143069379	143071299	1920	hard	yes
1655b_a	51008.97513	143075443	143077059	1616	hard	yes
1664_a	51017.76911	143834707	143837395	2688	hard	yes
1700_a	51053.71087	146940403	146942435	2032	hard	yes
1703_a	51056.77837	147205507	147207395	1888	hard	yes
1714_a	51067.64050	148143683	148146195	2512	hard	yes
1714_b	51067.70865	148149699	148151955	2256	hard	yes
1718_a	51071.90791	148513059	148514227	1168	hard	yes
1718_b	51071.96726	148517139	148520403	3264	hard	yes
1725_b	51078.02411	149041299	149042867	1568	hard	yes
1728_a	51081.83504	149369651	149373043	3392	hard	yes
1728_b	51081.89309	149375379	149377347	1968	hard	yes
1736_a	51089.71606	150051907	150052627	720	hard	yes
1736_b	51089.75430	150054947	150056195	1248	hard	yes
1736_c	51089.78087	150057347	150058387	1040	hard	yes
1736_d	51089.82087	150060707	150061939	1232	hard	yes
1743_a	51096.36865	150625475	150628627	3152	hard	yes
1812a_a	51165.70319	156617107	156618003	896	hard	yes
1812b_a	51165.81374	156626851	156627363	512	hard	yes
1813_a	51166.15087	156655571	156656899	1328	hard	yes
1813_b	51166.16948	156657363	156658323	960	hard	yes
1813_c	51166.22430	156661075	156664083	3008	hard	yes
1820_a	51173.67254	157305795	157306419	624	hard	yes
1820_b	51173.69384	157307027	157308867	1840	hard	yes
1820_c	51173.74587	157311539	157313347	1808	hard	yes
1826_a	51179.07328	157772019	157773443	1424	hard	yes
1826_b	51179.09347	157773587	157775363	1776	hard	yes
1826_c	51179.15097	157777715	157781171	3456	hard	yes
1826_d	51179.21902	157783731	157786915	3184	hard	yes
1833_a	51186.08717	158377475	158379987	2512	hard	yes
1833_b	51186.14837	158382291	158385747	3456	hard	yes
1833_c	51186.21495	158388035	158391507	3472	hard	yes
1841_a	51194.01022	159061667	159064899	3232	hard	yes
1841_b	51194.07809	159067427	159070867	3440	hard	yes
1841_c	51194.14467	159073187	159076611	3424	hard	yes
1849_a	51202.93828	159833155	159836179	3024	hard	yes

Continued on next page

TABLE 2 – continued

Reference <sup>1</sup>	MJD <sup>2</sup>	MET <sup>3</sup> Start	MET <sup>3</sup> Stop	Exposure (s)	Type	Spectral fit <sup>4</sup>
1862_d	51215.34717	160905859	160907731	1872	hard	yes
1868_a	51221.07041	161399747	161402819	3072	hard	yes
1868_c	51221.20661	161411763	161414339	2576	hard	yes
1868_d	51221.27559	161417939	161420083	2144	hard	yes
1911_a	51264.92347	165189459	165190915	1456	hard	yes
1911_b	51264.97837	165193187	165196675	3488	hard	yes
1946b_c	51299.23291	168153939	168155107	1168	soft	yes
1946c_a	51299.83078	168205411	168206947	1536	soft	yes
1946c_b	51299.88634	168209267	168212691	3424	soft	yes
1970_a	51323.66939	170264147	170267523	3376	hard	yes
1970_b	51323.72467	170269907	170271315	1408	hard	yes
1972_a	51325.07772	170386563	170388467	1904	hard	yes
1972_b	51325.14671	170392723	170394227	1504	hard	yes
1972_c	51325.21476	170398723	170399987	1264	hard	yes
1972_d	51325.25226	170402259	170402931	672	hard	yes
1972_e	51325.28097	170404419	170405731	1312	hard	yes
1978_a	51331.39643	170931747	170935155	3408	hard	yes
1978_b	51331.46272	170937459	170940899	3440	hard	yes
1978_c	51331.52948	170943219	170946675	3456	hard	yes
1979_a	51332.00319	170984803	170986947	2144	hard	yes
1979_b	51332.07059	170990691	170992707	2016	hard	yes
1979_c	51332.13754	170996499	170998467	1968	hard	yes
1979_d	51332.20384	171002211	171004211	2000	hard	yes
1983_a	51336.06495	171335635	171337987	2352	hard	yes
1983_b	51336.13217	171341491	171343747	2256	hard	yes
1983_c	51336.19198	171346067	171349507	3440	hard	yes
2003_a	51356.22911	173078499	173079491	992	hard	yes
2003_b	51356.29865	173084259	173085747	1488	hard	yes
2003_c	51356.36708	173090019	173091811	1792	hard	yes
2003_d	51356.43661	173095779	173098067	2288	hard	yes
2004_a	51357.22809	173164851	173165763	912	hard	yes
2004_b	51357.29791	173170595	173172083	1488	hard	yes
2004_c	51357.36671	173176355	173178211	1856	hard	yes
2004_d	51357.43550	173182115	173184339	2224	hard	yes
2005_a	51358.22550	173250851	173252115	1264	hard	yes
2005_b	51358.29476	173256627	173258307	1680	hard	yes
2005_c	51358.36430	173262387	173264563	2176	hard	yes
2005_d	51358.43282	173268115	173270675	2560	hard	yes
2006_a	51359.22476	173337171	173338467	1296	hard	yes
2006_b	51359.29402	173342963	173344643	1680	hard	yes
2006_c	51359.36291	173348723	173350787	2064	hard	yes
2006_d	51359.43217	173354451	173357027	2576	hard	yes
2008_a	51361.91171	173569059	173570883	1824	hard	yes
2008_b	51361.98208	173575427	173576675	1248	hard	yes
2009_a	51362.05059	173581539	173582403	864	hard	yes
2009_b	51362.08402	173584611	173585107	496	hard	yes
2009_c	51362.11884	173587539	173588195	656	hard	yes
2014_a	51367.28745	174033603	174035267	1664	hard	yes
2014_b	51367.35652	174039347	174041459	2112	hard	yes
2014_c	51367.41902	174045107	174046499	1392	hard	yes
2014_d	51367.43374	174046547	174047603	1056	hard	yes
2014_e	51367.49828	174050867	174054435	3568	hard	yes
2014_f	51367.56485	174056627	174060179	3552	hard	yes
2016_a	51369.90652	174259843	174261603	1760	hard	yes
2016_b	51369.97458	174265843	174267363	1520	hard	yes
2017_a	51370.04328	174271955	174273123	1168	hard	yes
2017_b	51370.07865	174275331	174275859	528	hard	yes
2017_c	51370.11059	174277843	174278867	1024	hard	yes
2017_d	51370.14698	174281075	174281923	848	hard	yes
2073_c	51426.91597	179185731	179186947	1216	soft	yes
2087_a	51440.62347	180369347	180371987	2640	soft	yes
2087_b	51440.69069	180375219	180377731	2512	soft	yes
2094_a	51447.74550	180984483	180987539	3056	soft	yes
2094_b	51447.81004	180989875	180993299	3424	soft	no
2094_c	51447.87652	180995619	180999043	3424	soft	no
2100_a	51453.73578	181501891	181505251	3360	soft	yes
2100_b	51453.80235	181507651	181510995	3344	soft	yes
2117_b	51470.45115	182946371	182949187	2816	soft	no
2117_c	51470.51828	182952227	182954931	2704	soft	no
2144_d	51497.74013	185304099	185306995	2896	hard	yes
2160_e	51513.69902	186683923	186684867	944	hard	yes

Continued on next page

TABLE 2 – continued

Reference <sup>1</sup>	MJD <sup>2</sup>	MET <sup>3</sup> Start	MET <sup>3</sup> Stop	Exposure (s)	Type	Spectral fit <sup>4</sup>
2165_a	51518.51411	187099779	187101059	1280	hard	yes
2165_b	51518.58467	187106147	187106883	736	hard	yes
2165_c	51518.62180	187109507	187109939	432	hard	yes
2165_d	51518.65374	187112259	187112707	448	hard	yes
2165_e	51518.68921	187115267	187115827	560	hard	yes
2172_a	51525.50402	187703779	187704915	1136	hard	yes
2172_b	51525.57134	187709715	187710611	896	hard	yes
2172_c	51525.63995	187715811	187716371	560	hard	yes
2172_d	51525.67800	187719011	187719747	736	hard	yes
2180_a	51533.49022	188393507	188395203	1696	hard	yes
2180_b	51533.55828	188399443	188401027	1584	hard	yes
2180_c	51533.62680	188405523	188406787	1264	hard	yes
2187_a	51540.47624	188997011	188998883	1872	hard	yes
2187_b	51540.54309	189002819	189004627	1808	hard	yes
2187_c	51540.61004	189008643	189010371	1728	hard	yes
2187_d	51540.65078	189012707	189013347	640	hard	yes
2187_e	51540.66976	189014387	189014947	560	hard	yes
2189_a	51542.53893	189175235	189177091	1856	hard	yes
2189_b	51542.60485	189180899	189182819	1920	hard	yes
2189_c	51542.71828	189190915	189192403	1488	hard	yes
2189_d	51542.79615	189196675	189200099	3424	hard	yes
2193_a	51546.46161	189513875	189516291	2416	hard	yes
2193_b	51546.52809	189519651	189522003	2352	hard	yes
2193_c	51546.59495	189525443	189527763	2320	hard	yes
2203_a	51556.43652	190375219	190378611	3392	hard	yes
2203_b	51556.50309	190380947	190384387	3440	hard	yes
2203_c	51556.56939	190386707	190390083	3376	hard	yes
2207_a	51560.43245	190720803	190723523	2720	hard	yes
2207_b	51560.49559	190725971	190729267	3296	hard	yes
2207_c	51560.55124	190731731	190733123	1392	hard	yes
2207_d	51560.57809	190734467	190735027	560	hard	yes
2214_a	51567.35541	191319267	191321347	2080	hard	yes
2214_b	51567.39948	191323747	191324483	736	hard	yes
2214_c	51567.42634	191325763	191327107	1344	hard	yes
2214_d	51567.46597	191329491	191330227	736	hard	yes
2214_e	51567.49680	191332179	191332867	688	hard	yes
2214_f	51567.53272	191335251	191336003	752	hard	yes
2221_a	51574.34587	191923507	191925059	1552	hard	yes
2221_b	51574.41485	191929683	191930803	1120	hard	yes
2221_c	51574.48309	191935747	191936531	784	hard	yes
2228_a	51581.33180	192527011	192528723	1712	hard	yes
2228_b	51581.39958	192532963	192534483	1520	hard	yes
2235_a	51588.45097	193142211	193143715	1504	hard	yes
2242_a	51595.29856	193733507	193735683	2176	hard	yes
2242_b	51595.36643	193739491	193741427	1936	hard	yes
2242_c	51595.43226	193745203	193747091	1888	hard	yes
2242_d	51595.49874	193751059	193752723	1664	hard	yes
2249_a	51602.34643	194342147	194344915	2768	hard	yes
2265_a	51618.31847	195722947	195724083	1136	hard	yes
2265_b	51618.35847	195726435	195727507	1072	hard	yes
2265_c	51618.42282	195732147	195732915	768	hard	yes
2272_a	51625.23513	196320451	196321779	1328	hard	yes
2272_b	51625.30384	196326563	196327539	976	hard	yes
2272_c	51625.37180	196332579	196333267	688	hard	yes
2272_d	51625.40587	196335459	196336275	816	hard	yes
2286_a	51639.19921	197526755	197528467	1712	hard	yes
2286_b	51639.26643	197532611	197534227	1616	hard	yes
2301_c	51654.34328	198834643	198837475	2832	hard	yes
2303_a	51656.40865	199012851	199016163	3312	hard	yes
2303_c	51656.53624	199024291	199026771	2480	hard	yes
2304_a	51657.33911	199093235	199096563	3328	hard	yes
2304_b	51657.40106	199098979	199101523	2544	hard	yes
2305_a	51658.07208	199156707	199159747	3040	hard	yes
2305_b	51658.13884	199162483	199165507	3024	hard	yes
2305_c	51658.20291	199167811	199171251	3440	hard	yes
2305_d	51658.26921	199173523	199176995	3472	hard	yes
2305_e	51658.33569	199179283	199182723	3440	hard	yes
2305_f	51658.39578	199185043	199187347	2304	hard	yes
2305_g	51658.80115	199219523	199222915	3392	hard	yes
2306_a	51659.19745	199253987	199256931	2944	hard	yes
2306_b	51659.25198	199259683	199260659	976	hard	yes

Continued on next page

TABLE 2 – continued

Reference <sup>1</sup>	MJD <sup>2</sup>	MET <sup>3</sup> Start	MET <sup>3</sup> Stop	Exposure (s)	Type	Spectral fit <sup>4</sup>
2306_c	51659.86485	199311411	199314835	3424	hard	yes
2315_a	51668.10948	200023955	200026963	3008	hard	yes
2315_b	51668.16532	200029763	200030803	1040	hard	yes
2315_c	51668.18393	200031107	200032675	1568	hard	yes
2378_a	51730.92319	205451811	205453315	1504	hard	yes
2378_b	51730.99217	205457987	205459059	1072	hard	yes
2378_c	51731.06041	205464051	205464787	736	hard	yes
2378_d	51731.09337	205466979	205467555	576	hard	yes
2378_e	51731.12772	205469923	205470547	624	hard	yes
2384_a	51737.90022	206054531	206056227	1696	hard	yes
2384_b	51737.96763	206060435	206061971	1536	hard	yes
2385a_a	51738.03661	206066611	206067715	1104	hard	yes
2385a_b	51738.10374	206072499	206073427	928	hard	yes
2385b_a	51738.27745	206087171	206088771	1600	hard	yes
2385b_b	51738.34661	206092931	206094963	2032	hard	yes
2385b_c	51738.42069	206098659	206102035	3376	hard	yes
2385b_d	51738.48569	206104611	206107315	2704	hard	yes
2385b_e	51738.54819	206110131	206112595	2464	hard	yes
2386_a	51739.27393	206173251	206174883	1632	hard	yes
2386_b	51739.34319	206179011	206181091	2080	hard	yes
2386_c	51739.41800	206184771	206188259	3488	hard	yes
2386_d	51739.48458	206190531	206194003	3472	hard	yes
2387_a	51740.27115	206259459	206260995	1536	hard	yes
2387_b	51740.29782	206262163	206262899	736	hard	yes
2387_c	51740.34041	206265155	206267267	2112	hard	yes
2387_d	51740.36393	206267859	206268627	768	hard	yes
2387_e	51740.41448	206270867	206274355	3488	hard	yes
2387_f	51740.48115	206276627	206280115	3488	hard	yes
2387_g	51740.54772	206282387	206285859	3472	hard	yes
2391_b	51744.08134	206588771	206590083	1312	hard	yes
2405_a	51758.88772	207867395	207870003	2608	hard	yes
2405_b	51758.95430	207873171	207875731	2560	hard	yes
2405_c	51759.02134	207879043	207881443	2400	hard	yes
2426_b	51779.99041	209691555	209692387	832	hard	yes
2433_a	51786.79291	210279091	210280323	1232	hard	yes
2433_b	51786.86208	210285075	210286291	1216	hard	yes
2433_c	51786.96513	210294179	210294995	816	hard	yes
2433_d	51786.99782	210297043	210297779	736	hard	yes
2440_a	51793.76652	210881299	210883155	1856	hard	yes
2440_b	51793.83522	210887443	210888883	1440	hard	yes
2440_c	51793.90254	210893347	210894611	1264	hard	yes
2440_d	51793.97022	210899299	210900355	1056	hard	yes
2446_a	51799.94569	211415555	211416659	1104	hard	yes
2455_a	51808.70495	212171731	212174083	2352	hard	yes
2455_b	51808.77152	212177491	212179827	2336	hard	yes
2455_c	51808.83800	212183251	212185555	2304	hard	yes
2538_b	51891.55856	219330867	219332051	1184	hard	yes
2538_c	51891.62578	219336739	219337795	1056	hard	yes
2538_d	51891.69430	219342867	219343507	640	hard	yes
2544_a	51897.45939	219840403	219842179	1776	hard	yes
2544_b	51897.52911	219846547	219848083	1536	hard	yes
2544_c	51897.59606	219852403	219853795	1392	hard	yes
2544_d	51897.66532	219858611	219859555	944	hard	yes
2549_a	51902.50347	220276195	220278003	1808	hard	yes
2549_b	51902.57171	220282259	220283731	1472	hard	yes
2549_c	51902.63884	220288131	220289459	1328	hard	yes
2559_a	51912.45189	221135507	221137779	2272	hard	yes
2559_b	51912.51800	221141203	221143507	2304	hard	yes
2559_c	51912.58458	221146963	221149251	2288	hard	yes
2559_d	51912.63013	221151523	221152563	1040	hard	yes
2573_a	51926.49847	222349555	222350979	1424	hard	yes
2587_a	51940.38643	223549555	223550819	1264	hard	yes
2587_b	51940.45513	223555667	223556579	912	hard	yes
2587_c	51940.59050	223567603	223568035	432	hard	yes
2594_a	51947.35097	224151123	224152723	1600	hard	yes
2594_b	51947.41819	224157027	224158435	1408	hard	yes
2594_c	51947.48606	224163043	224164147	1104	hard	yes
2614_a	51967.30643	225874947	225877203	2256	hard	yes
2614_b	51967.37421	225880659	225883203	2544	hard	yes
2614_c	51967.43930	225886179	225888931	2752	hard	yes
2623_a	51976.26791	226649731	226650963	1232	hard	yes

Continued on next page

TABLE 2 – continued

Reference <sup>1</sup>	MJD <sup>2</sup>	MET <sup>3</sup> Start	MET <sup>3</sup> Stop	Exposure (s)	Type	Spectral fit <sup>4</sup>
2623_b	51976.32208	226653331	226656723	3392	hard	yes
2623_c	51976.45393	226665011	226667827	2816	hard	yes
2629_a	51982.22624	227163699	227166595	2896	hard	yes
2629_b	51982.29004	227168979	227172339	3360	hard	yes
2639_a	51992.90652	228086723	228089123	2400	hard	yes
2640_a	51993.10532	228103875	228106323	2448	hard	yes
2640_b	51993.17198	228110483	228111235	752	hard	yes
2644_a	51997.22291	228460131	228461587	1456	hard	yes
2644_b	51997.29069	228466115	228467315	1200	hard	yes
2644_c	51997.35828	228472067	228473043	976	hard	yes
2651_a	52004.18217	229061235	229063043	1808	hard	yes
2651_b	52004.25022	229067267	229068771	1504	hard	yes
2651_c	52004.31754	229073171	229074499	1328	hard	yes
2658_a	52011.20745	229668163	229670083	1920	hard	yes
2658_b	52011.27485	229674099	229675795	1696	hard	yes
2658_c	52011.34143	229679859	229681539	1680	hard	yes
2663_a	52016.17680	230097379	230099571	2192	hard	yes
2663_b	52016.24319	230103107	230105315	2208	hard	yes
2663_c	52016.30550	230108147	230111043	2896	hard	yes
2663_d	52016.35958	230113363	230115171	1808	hard	yes
2672_a	52025.18448	230875043	230878435	3392	hard	yes
2672_b	52025.25078	230880771	230884163	3392	hard	yes
2678_b	52031.21541	231396099	231399523	3424	hard	yes
2686_b	52039.18402	232085939	232086659	720	hard	yes
2692_a	52045.07809	232595091	232596003	912	hard	yes
2713_a	52066.01467	234403459	234405475	2016	hard	yes
2713_b	52066.08069	234409395	234410947	1552	hard	yes
2713_c	52066.14958	234415155	234417091	1936	hard	yes
2713_d	52066.21180	234420211	234422787	2576	hard	yes
2720_a	52073.03504	235009571	235012483	2912	hard	yes
2720_b	52073.09819	235014771	235018195	3424	hard	yes
2720_c	52073.16134	235020515	235023363	2848	hard	yes
2725_a	52078.00171	235438435	235441859	3424	hard	yes
2737_a	52090.92226	236554915	236558051	3136	hard	yes
2743_b	52096.96448	237077971	237079091	1120	hard	yes
2743_c	52097.03226	237084003	237084771	768	hard	yes
2746_b	52099.15430	237267459	237268003	544	hard	yes
2746_c	52099.19087	237270499	237271283	784	hard	yes
2747_a	52100.11476	237350419	237351011	592	hard	yes
2747_b	52100.14809	237353267	237353923	656	hard	yes
2747_c	52100.25208	237361891	237363267	1376	hard	yes
2747_d	52100.32217	237367923	237369347	1424	hard	yes
2748_a	52101.00624	237427267	237428211	944	hard	yes
2748_b	52101.07448	237433219	237434051	832	hard	yes
2748_c	52101.14152	237439059	237439795	736	hard	yes
2753a_a	52106.04152	237862179	237863395	1216	hard	yes
2753a_b	52106.10911	237868131	237869123	992	hard	yes
2753b_a	52106.36050	237888675	237892019	3344	hard	yes
2754a_d	52107.20809	237963027	237964131	1104	hard	yes
2759_a	52112.92689	238456739	238458627	1888	hard	yes
2759_c	52113.06180	238468627	238470051	1424	hard	yes
2770_a	52122.99115	239325891	239328579	2688	hard	yes
2773a_a	52126.03476	239588531	239591875	3344	hard	yes
2773a_b	52126.10106	239594259	239597603	3344	hard	yes
2773b_a	52126.16726	239599987	239603315	3328	hard	yes
2773b_b	52126.22902	239605715	239608259	2544	hard	yes
2773b_c	52126.29569	239611443	239614051	2608	hard	yes
2773b_d	52126.35374	239617171	239618355	1184	hard	yes
2773b_e	52126.37004	239618435	239619907	1472	hard	yes
2773b_g	52126.49809	239628611	239631859	3248	hard	yes
2774_a	52127.15735	239685875	239688515	2640	hard	yes
2774_b	52127.22189	239691603	239693939	2336	hard	yes
2774_c	52127.28874	239697315	239699779	2464	hard	yes
2774_d	52127.35624	239703043	239705715	2672	hard	yes
2774_e	52127.42337	239708771	239711587	2816	hard	yes
2774_f	52127.49161	239714499	239717651	3152	hard	yes
2775_a	52128.14809	239771651	239773939	2288	hard	yes
2775_b	52128.21467	239777363	239779731	2368	hard	yes
2775_c	52128.28161	239783075	239785587	2512	hard	yes
2775_d	52128.34893	239788787	239791507	2720	hard	yes
2775_f	52128.48439	239800243	239803459	3216	hard	yes

Continued on next page

TABLE 2 – continued

Reference <sup>1</sup>	MJD <sup>2</sup>	MET <sup>3</sup> Start	MET <sup>3</sup> Stop	Exposure (s)	Type	Spectral fit <sup>4</sup>
2795_a	52148.76652	241553459	241554995	1536	hard	yes
2795_c	52148.93680	241568643	241569235	592	hard	yes
2804_a	52157.77485	242331699	242333395	1696	hard	yes
2804_b	52157.90995	242343603	242344835	1232	hard	yes
2809_a	52162.74059	242760627	242762547	1920	hard	yes
2809_b	52162.80800	242766563	242768259	1696	hard	yes
2809_c	52162.87550	242772499	242773987	1488	hard	yes
2831_b	52184.84939	244670083	244673491	3408	soft	yes
2882_a	52235.67958	249061843	249065187	3344	soft	no
2882_b	52235.74161	249067539	249070211	2672	soft	yes
2901_a	52254.47717	250686883	250688371	1488	soft	no
2901_c	52254.61282	250698883	250699811	928	soft	no
2907_a	52260.49624	251206899	251208451	1552	soft	no
2923a_a	52276.42680	252582931	252585219	2288	hard	yes
2923a_b	52276.49309	252588707	252590899	2192	hard	yes
2936_a	52289.37717	253701283	253704691	3408	soft	yes
2943_a	52296.38254	254306627	254309875	3248	hard	yes
2943_b	52296.45245	254312851	254315731	2880	hard	yes
2951_a	52304.39430	254999891	255001043	1152	hard	yes
2951_b	52304.46198	255005907	255006723	816	hard	yes
2951_c	52304.52948	255011859	255012435	576	hard	yes
2959_a	52312.32217	255684595	255686275	1680	hard	yes
2959_b	52312.38930	255690499	255691971	1472	hard	yes
2959_c	52312.45680	255696451	255697683	1232	hard	yes
2959_d	52312.52421	255702387	255703395	1008	hard	yes
2959_e	52312.55976	255705635	255706291	656	hard	yes
2965_a	52318.33319	256203859	256205715	1856	hard	yes
2965_b	52318.40050	256209795	256211411	1616	hard	yes
2965_c	52318.46772	256215699	256217123	1424	hard	yes
2965_d	52318.53513	256221635	256222835	1200	hard	yes
2980_a	52333.32013	257498083	257501235	3152	hard	yes
2980_b	52333.38365	257503603	257506691	3088	hard	yes
2986_a	52339.32967	258017251	258020515	3264	hard	yes
2986_b	52339.39495	258022835	258026211	3376	hard	yes
2986_c	52339.46115	258028547	258031939	3392	hard	no
3001_a	52354.26643	259308883	259309955	1072	hard	yes
3001_b	52354.30143	259312179	259312707	528	hard	yes
3001_c	52354.33467	259314947	259315683	736	hard	yes
3007_a	52360.20782	259822003	259823507	1504	hard	yes
3007_b	52360.27559	259828003	259829219	1216	hard	yes
3007_d	52360.41004	259839827	259840627	800	hard	yes
3009_a	52362.83884	260048451	260051699	3248	hard	yes
3009_b	52362.89559	260054163	260055795	1632	hard	yes
3009_c	52362.91439	260055875	260057331	1456	hard	yes
3009_d	52362.96041	260059859	260061299	1440	hard	yes
3011_b	52364.63254	260204387	260205715	1328	hard	yes
3011_d	52364.75393	260213955	260217123	3168	hard	yes
3011_e	52364.81985	260219651	260222819	3168	hard	yes
3011_f	52364.88587	260225363	260228515	3152	hard	yes
3011_g	52364.93772	260231075	260231763	688	hard	yes
3012a_a	52364.96337	260233043	260234227	1184	hard	yes
3012a_b	52365.02180	260237443	260239923	2480	hard	yes
3012a_c	52365.08495	260243507	260244771	1264	hard	yes
3012a_d	52365.09819	260244915	260245651	736	hard	yes
3012a_e	52365.15800	260249555	260251347	1792	hard	yes
3012a_f	52365.22541	260255507	260257043	1536	hard	yes
3012a_g	52365.29245	260261379	260262755	1376	hard	yes
3012b_a	52365.35976	260267315	260268451	1136	hard	yes
3012b_b	52365.42634	260273139	260274131	992	hard	yes
3012b_c	52365.46495	260276595	260277347	752	hard	yes
3012b_d	52365.49393	260279091	260279859	768	hard	yes
3012b_e	52365.53263	260282227	260283411	1184	hard	yes
3012b_f	52365.55995	260284787	260285571	784	hard	yes
3012b_g	52365.61050	260287939	260291155	3216	hard	yes
3012b_h	52365.67393	260293731	260296323	2592	hard	yes
3012c_a	52365.74319	260299347	260302675	3328	hard	yes
3012c_b	52365.80921	260305059	260308371	3312	hard	yes
3012c_c	52365.87522	260310755	260314083	3328	hard	yes
3012c_d	52365.92671	260316467	260317267	800	hard	yes
3013a_a	52365.95328	260318547	260319779	1232	hard	yes
3013a_b	52366.01171	260322947	260325475	2528	hard	yes

Continued on next page

TABLE 2 – continued

Reference <sup>1</sup>	MJD <sup>2</sup>	MET <sup>3</sup> Start	MET <sup>3</sup> Stop	Exposure (s)	Type	Spectral fit <sup>4</sup>
3013a_c	52366.07985	260329011	260331187	2176	hard	yes
3013b_a	52366.14745	260334995	260336883	1888	hard	yes
3013b_b	52366.21495	260340947	260342595	1648	hard	yes
3013b_c	52366.28235	260346883	260348307	1424	hard	yes
3013b_d	52366.34976	260352819	260354019	1200	hard	yes
3019_a	52372.14828	260853827	260854995	1168	hard	yes
3019_b	52372.21522	260859699	260860691	992	hard	yes
3035_a	52388.11754	262232483	262235827	3344	hard	yes
3035_b	52388.18782	262238915	262241539	2624	hard	yes
3041_a	52394.19309	262757811	262760355	2544	hard	yes
3041_b	52394.25411	262762659	262766051	3392	hard	yes
3049_a	52402.10587	263441027	263444467	3440	hard	yes
3049_b	52402.15643	263446723	263447507	784	hard	yes
3049_c	52402.18772	263449475	263450163	688	hard	yes
3057_a	52410.10365	264133123	264134387	1264	hard	yes
3057_b	52410.17097	264139059	264140083	1024	hard	yes
3063_a	52416.03856	264645715	264647347	1632	hard	yes
3063_b	52416.10680	264651699	264653155	1456	hard	yes
3063_c	52416.17384	264657587	264658851	1264	hard	yes
3069_a	52422.04152	265164259	265166115	1856	hard	yes
3069_b	52422.10865	265170163	265171811	1648	hard	yes
3069_c	52422.17550	265176019	265177507	1488	hard	yes
3069_d	52422.24300	265181987	265183203	1216	hard	yes
3078_a	52431.00069	265938883	265939635	752	hard	yes
3078_b	52431.07013	265944707	265945811	1104	hard	yes
3105_a	52458.98356	268356467	268357491	1024	hard	yes
3119_a	52472.89513	269557971	269559907	1936	hard	yes
3119_b	52473.02985	269569859	269571299	1440	hard	yes
3126_a	52479.88374	270161683	270163827	2144	hard	yes
3132_a	52485.22597	270623331	270625315	1984	hard	yes
3132_b	52485.28097	270627651	270630499	2848	hard	yes
3132_c	52485.34772	270633347	270636339	2992	hard	yes
3132_d	52485.41393	270639043	270642083	3040	hard	yes
3132_e	52485.47078	270644739	270646211	1472	hard	yes
3133_a	52486.86819	270765139	270767283	2144	hard	yes
3160_a	52513.78097	273090755	273092195	1440	hard	yes
3160_b	52513.84865	273096755	273097891	1136	hard	yes
3167_a	52520.76782	273694275	273696003	1728	hard	yes
3174_a	52527.75356	274297715	274299699	1984	hard	yes
3174_b	52527.82078	274303651	274305379	1728	hard	yes
3182_a	52535.72652	274986387	274988755	2368	hard	yes
3182_b	52535.79226	274992067	274994435	2368	hard	yes
3189_a	52542.70902	275589347	275592371	3024	hard	yes
3197_a	52550.74652	276283603	276286995	3392	hard	yes
3203_a	52556.67680	276795955	276799395	3440	hard	yes
3211_a	52564.66337	277487043	277488387	1344	hard	yes
3211_b	52564.73124	277493059	277494099	1040	hard	yes
3265_a	52618.54143	282142099	282143459	1360	soft	no
3274_a	52627.49189	282915267	282916931	1664	soft	yes
3280_b	52633.54606	283438483	283439875	1392	soft	yes
3287_a	52640.45541	284034995	284037299	2304	soft	yes
3287_b	52640.53245	284042387	284043219	832	soft	yes
3293_a	52646.44245	284551779	284555075	3296	soft	yes
3293_b	52646.50819	284557443	284560771	3328	soft	yes
3306_a	52659.40856	285672019	285675379	3360	soft	no
3321_a	52674.36050	286964771	286966323	1552	soft	no
3321_b	52674.42569	286970563	286971795	1232	soft	no
3329_a	52682.45254	287664019	287665379	1360	soft	yes
3364_a	52717.26356	290671779	290672963	1184	hard	yes
3372_a	52725.21809	291359171	291360115	944	hard	yes
3372_b	52725.28495	291365027	291365811	784	hard	yes
3378_a	52731.78967	291925731	291929123	3392	hard	yes
3378_b	52731.85550	291931427	291934803	3376	hard	yes
3378_c	52731.92384	291937555	291940483	2928	hard	yes
3379_a	52732.19263	291961267	291963219	1952	hard	yes
3379_b	52732.25939	291967139	291968883	1744	hard	yes
3385_a	52738.89439	292539699	292542851	3152	hard	yes
3385_b	52738.95754	292545587	292547875	2288	hard	yes
3385_c	52739.02319	292551523	292553283	1760	hard	yes
3385_d	52739.09180	292557443	292559219	1776	hard	yes
3386_a	52739.22911	292569123	292571267	2144	hard	yes

Continued on next page



TABLE 2 – continued

Reference <sup>1</sup>	MJD <sup>2</sup>	MET <sup>3</sup> Start	MET <sup>3</sup> Stop	Exposure (s)	Type	Spectral fit <sup>4</sup>
3386_b	52739.29513	292574835	292576963	2128	hard	yes
3386_c	52739.35356	292579251	292582643	3392	hard	yes
3386_d	52739.41939	292584947	292588323	3376	hard	yes
3386_e	52739.47032	292590643	292591427	784	hard	yes
3386_f	52739.49319	292592019	292594003	1984	hard	yes
3386_g	52739.55143	292596403	292599683	3280	hard	yes
3392_a	52745.20772	293085075	293088419	3344	hard	yes
3392_b	52745.27374	293091443	293093459	2016	hard	yes
3399_a	52752.24291	293693139	293696035	2896	hard	yes
3407_a	52760.13708	294374979	294378307	3328	hard	yes
3413_a	52766.06680	294888163	294889779	1616	hard	yes
3413_b	52766.13587	294894403	294895475	1072	hard	yes
3415_a	52768.61587	295108003	295110419	2416	hard	yes
3415_b	52768.68726	295113635	295117123	3488	hard	yes
3415_c	52768.75282	295119283	295122803	3520	hard	yes
3415_d	52768.81874	295124979	295128499	3520	hard	yes
3415_e	52768.87384	295130691	295132307	1616	hard	yes
3415_f	52768.89208	295132339	295133811	1472	hard	yes
3419_a	52772.05254	295405315	295406963	1648	hard	yes
3419_b	52772.12004	295411299	295412643	1344	hard	yes
3419_c	52772.18726	295417235	295418323	1088	hard	yes
3427_a	52780.07504	296098419	296100147	1728	hard	yes
3427_b	52780.14198	296104307	296105827	1520	hard	yes
3427_c	52780.20856	296110131	296111507	1376	hard	yes
3433_a	52786.05671	296615091	296617107	2016	hard	yes
3433_b	52786.12115	296621027	296622307	1280	hard	yes
3433_c	52786.18985	296626771	296628435	1664	hard	yes
3456_c	52809.11745	298608083	298609011	928	hard	yes
3482_a	52835.89522	300921251	300923043	1792	hard	yes
3482_b	52835.96356	300927155	300928947	1792	hard	yes
3482_c	52836.02828	300933027	300934259	1232	hard	yes
3490_a	52843.97819	301619139	301621891	2752	hard	yes
3567_a	52920.69458	308248195	308249427	1232	soft	yes
3567_b	52920.76226	308254227	308255091	864	soft	yes
3567_c	52920.86198	308262995	308263555	560	soft	yes
3574_a	52927.65958	308849795	308851379	1584	soft	yes
3574_b	52927.72661	308855715	308857043	1328	soft	no
3574_c	52927.79356	308861603	308862723	1120	soft	no
3580_a	52933.63754	309366163	309368003	1840	soft	yes
3580_b	52933.70467	309372083	309373683	1600	soft	yes
3580_c	52933.76930	309377971	309378963	992	soft	no
3588_a	52941.64735	310058483	310059779	1296	soft	yes
3588_c	52941.77828	310069763	310071123	1360	soft	yes
3592a_b	52945.32430	310375187	310378451	3264	soft	yes
3592b_e	52945.92448	310427811	310429539	1728	soft	yes
3602_a	52955.58078	311262019	311263939	1920	soft	no
3602_b	52955.63809	311266243	311269619	3376	soft	no
3602_c	52955.70393	311271939	311275299	3360	soft	yes
3602_d	52955.76559	311277651	311280243	2592	soft	yes
3608_a	52961.61606	311782739	311786115	3376	soft	no
3608_b	52961.67013	311788611	311789587	976	soft	no
3613_a	52966.01087	312163011	312165267	2256	soft	yes
3613_b	52966.07828	312168643	312171283	2640	soft	yes
3613_c	52966.14671	312174339	312177411	3072	soft	yes
3613_d	52966.21421	312179987	312183427	3440	soft	yes
3613_e	52966.27995	312185683	312189091	3408	soft	yes
3613_f	52966.34522	312191811	312194243	2432	soft	yes
3613_g	52966.40411	312197027	312199203	2176	soft	yes
3613_h	52966.72606	312225459	312226403	944	soft	yes
3613_j	52966.85939	312236755	312238147	1392	soft	yes
3614_a	52967.52884	312293635	312296947	3312	soft	yes
3614_b	52967.60856	312301731	312302627	896	soft	yes
3624_a	52977.52606	313158307	313159795	1488	soft	yes
3629_b	52982.71735	313607043	313608115	1072	soft	no
3635_a	52988.48606	314105507	314106483	976	soft	yes
3635_b	52988.55763	314111331	314113027	1696	soft	yes
3635_c	52988.62513	314117219	314118803	1584	soft	yes
3648_a	53001.55365	315233603	315236467	2864	hard	yes
3648_b	53001.62180	315239507	315242339	2832	hard	yes
3660_a	53013.43995	316260355	316263667	3312	soft	yes
3668_a	53021.39893	316949011	316950323	1312	soft	yes

Continued on next page

TABLE 2 – continued

Reference <sup>1</sup>	MJD <sup>2</sup>	MET <sup>3</sup> Start	MET <sup>3</sup> Stop	Exposure (s)	Type	Spectral fit <sup>4</sup>
3668_b	53021.46671	316955059	316955987	928	soft	yes
3668_c	53021.56763	316963891	316964595	704	soft	yes
3672_a	53025.40587	317295219	317296515	1296	soft	yes
3672_b	53025.47309	317301155	317302195	1040	soft	no
3672_c	53025.53985	317307027	317307859	832	soft	no
3692_a	53045.36272	319019059	319021219	2160	hard	yes
3692_b	53045.49208	319030051	319032579	2528	hard	yes
3701_a	53054.41745	319800803	319804131	3328	hard	yes
3701_b	53054.48374	319806579	319809811	3232	hard	yes
3724_a	53077.27976	321777123	321778419	1296	hard	yes
3731_a	53084.23689	322378003	322379731	1728	hard	yes
3731_b	53084.29958	322383939	322384627	688	hard	yes
3731_c	53084.37078	322389795	322391075	1280	hard	yes
3731_d	53084.43772	322395683	322396755	1072	hard	yes
3731_e	53084.50430	322401523	322402419	896	hard	yes
3736_a	53089.22476	322808947	322810691	1744	hard	yes
3736_b	53089.35661	322820627	322821795	1168	hard	yes
3741a_a	53094.21254	323239699	323241827	2128	hard	yes
3741a_b	53094.27911	323245539	323247491	1952	hard	yes
3741a_c	53094.34458	323251187	323253155	1968	hard	yes
3741a_d	53094.41208	323257171	323258835	1664	hard	yes
3741b_a	53094.59198	323272515	323274579	2064	hard	yes
3741b_b	53094.61208	323274723	323275843	1120	hard	yes
3741b_c	53094.66467	323278131	323281523	3392	hard	yes
3741b_d	53094.73041	323283827	323287187	3360	hard	yes
3741b_e	53094.79624	323289523	323292867	3344	hard	yes
3747_a	53100.24615	323760771	323763363	2592	hard	yes
3750_a	53102.94319	323994019	323996163	2144	hard	yes
3750_b	53103.13495	324010355	324012963	2608	hard	yes
3756_a	53109.31300	324544595	324546291	1696	hard	yes
3764_a	53117.12374	325219411	325221171	1760	hard	yes
3769a_a	53122.11467	325650771	325652243	1472	hard	yes
3769b_a	53122.18384	325657059	325657907	848	hard	yes
3770_a	53123.09930	325735827	325737331	1504	hard	yes
3771_a	53124.08347	325820803	325822419	1616	hard	yes
3772_a	53125.13624	325911955	325913187	1232	hard	yes
3773_a	53126.12078	325996995	325998275	1280	hard	yes
3774_a	53127.10485	326081955	326083363	1408	hard	yes
3775_a	53128.15634	326172899	326174115	1216	hard	yes
3778_a	53131.10791	326427763	326429283	1520	hard	yes
3778_b	53131.17532	326433699	326434995	1296	hard	yes
3779a_a	53132.22680	326524611	326525779	1168	hard	yes
3779b_a	53132.54180	326550691	326554131	3440	hard	yes
3779b_b	53132.60717	326556323	326559795	3472	hard	yes
3779b_c	53132.67309	326562035	326565475	3440	hard	yes
3779b_d	53132.73847	326567667	326571139	3472	hard	yes
3779b_e	53132.80365	326573363	326576707	3344	hard	yes
3784_a	53137.08013	326943635	326945411	1776	hard	yes
3785a_c	53138.26124	327046243	327046899	656	hard	yes
3785b_d	53138.64939	327078707	327081507	2800	hard	yes
3786a_a	53139.04504	327113507	327115075	1568	hard	yes
3786a_c	53139.18115	327125267	327126835	1568	hard	yes
3786a_d	53139.24847	327131203	327132531	1328	hard	yes
3786a_e	53139.31430	327136899	327138211	1312	hard	yes
3786b_c	53139.69587	327168819	327172227	3408	hard	yes
3786b_d	53139.76235	327174643	327177891	3248	hard	yes
3786b_e	53139.83032	327180707	327183571	2864	hard	yes
3786b_f	53139.89328	327186643	327188515	1872	hard	yes
3787a_a	53140.03161	327198483	327200579	2096	hard	yes
3787a_b	53140.09837	327204355	327206243	1888	hard	yes
3787a_c	53140.16559	327210307	327211907	1600	hard	yes
3787b_a	53140.23180	327216099	327217555	1456	hard	yes
3787b_b	53140.29809	327221859	327223251	1392	hard	yes
3787b_c	53140.33819	327225587	327226451	864	hard	yes
3787b_d	53140.36124	327227091	327228931	1840	hard	yes
3787b_e	53140.41791	327231219	327234595	3376	hard	yes
3851_a	53204.93559	332805811	332808659	2848	hard	yes
3851_b	53204.99263	332810979	332813347	2368	hard	yes
3861_a	53214.90717	333667123	333670435	3312	hard	yes
3861_b	53214.97263	333672755	333676115	3360	hard	yes
3911_a	53264.89772	337987203	337988723	1520	hard	yes

Continued on next page

TABLE 2 – continued

Reference <sup>1</sup>	MJD <sup>2</sup>	MET <sup>3</sup> Start	MET <sup>3</sup> Stop	Exposure (s)	Type	Spectral fit <sup>4</sup>
3980_b	53333.60911	343924003	343925251	1248	soft	no
3980_c	53333.67578	343929859	343930915	1056	soft	yes
3988_a	53341.54180	344609091	344610931	1840	soft	yes
3988_b	53341.67254	344620851	344621763	912	soft	yes
4000_b	53353.53772	345645443	345647475	2032	soft	yes
4014_a	53367.43782	346845763	346849091	3328	soft	no
4014_b	53367.50328	346851411	346854755	3344	soft	no
4014_c	53367.56837	346857043	346860371	3328	soft	no
4029_b	53382.47022	348145635	348146819	1184	soft	no
4029_c	53382.53708	348151523	348152483	960	soft	no
4036_a	53389.41902	348745779	348747427	1648	soft	no
4036_b	53389.48597	348751667	348753107	1440	soft	no
4053_a	53406.51717	350223203	350224563	1360	hard	yes
4063_a	53416.36217	351073139	351075843	2704	hard	yes
4063_b	53416.42411	351078163	351081523	3360	hard	yes
4063_c	53416.48347	351084451	351085491	1040	hard	yes
4078_a	53431.32189	352366419	352367603	1184	hard	yes
4078_b	53431.38930	352372403	352373267	864	hard	yes
4086_a	53439.32050	353057363	353058819	1456	hard	yes
4086_b	53439.45365	353069043	353070147	1104	hard	yes
4089_a	53442.97754	353373187	353374931	1744	hard	yes
4089_b	53443.04615	353379171	353380803	1632	hard	yes
4090_a	53443.11328	353385075	353386499	1424	hard	yes
4090_b	53443.25124	353396851	353398563	1712	hard	yes
4091_a	53444.02791	353464035	353465587	1552	hard	yes
4091_b	53444.10041	353470019	353472131	2112	hard	yes
4093_a	53446.26198	353657363	353658307	944	hard	yes
4093_b	53446.39921	353669139	353670243	1104	hard	yes
4093_c	53446.46624	353674755	353676211	1456	hard	yes
4095_a	53448.23272	353827075	353829139	2064	hard	yes
4095_b	53448.29735	353832979	353834403	1424	hard	yes
4103_a	53456.29458	354523443	354525859	2416	hard	yes
4119a_a	53472.27254	355904579	355905715	1136	hard	yes
4119b_a	53472.94078	355961203	355964563	3360	hard	yes
4119b_b	53473.00624	355966851	355970227	3376	hard	yes
4120a_a	53473.07272	355972659	355975907	3248	hard	yes
4120a_b	53473.13745	355978179	355981571	3392	hard	yes
4120b_a	53473.99069	356051987	356055203	3216	hard	yes
4126_a	53479.25041	356507667	356508403	736	hard	yes
4162_a	53515.08652	359603219	359605331	2112	soft	yes
4162_b	53515.15319	359608867	359611203	2336	soft	no
4175_a	53528.01763	360720819	360722227	1408	soft	no
4189_a	53542.04541	361932835	361934211	1376	soft	no
4194_a	53547.94004	362441955	362443683	1728	soft	no
4195_a	53548.00476	362447859	362448963	1104	soft	no
4203_a	53555.99976	363138131	363140227	2096	soft	no
4217_a	53570.80745	364416883	364420243	3360	soft	no
4224_a	53577.89837	365030611	365031827	1216	soft	no
4225_a	53578.00180	365039747	365040563	816	soft	yes
4225_b	53578.06772	365045395	365046307	912	soft	no
4235_a	53588.84356	365976099	365977667	1568	soft	no
4235_b	53588.91069	365982035	365983331	1296	soft	no
4247_a	53600.90013	367017667	367019475	1808	soft	no
4274b_a	53627.87643	369348883	369349763	880	soft	yes
4287_a	53640.40930	370430451	370433875	3424	soft	yes
4293_a	53646.77578	370981427	370983027	1600	hard	yes
4300_a	53653.71856	371581075	371583091	2016	hard	yes
4300_b	53653.78143	371586867	371588163	1296	hard	yes
4307_a	53660.00152	372123267	372126595	3328	hard	yes
4307_b	53660.06309	372128867	372131635	2768	hard	yes
4308_a	53661.71541	372272227	372273795	1568	hard	yes
4316_a	53669.70476	372962131	372964451	2320	hard	yes
4316_b	53669.77032	372967795	372970115	2320	hard	yes
4331_a	53684.58550	374248323	374249651	1328	soft	yes
4331_b	53684.65328	374254371	374255315	944	soft	yes
4334_a	53687.66559	374514643	374515571	928	soft	yes
4334_b	53687.76800	374523699	374524211	512	soft	yes
4365_a	53718.58328	377185139	377187651	2512	hard	yes
4365_b	53718.64411	377189987	377193315	3328	hard	yes
4370_a	53723.48282	377608835	377610595	1760	hard	yes
4370_b	53723.50106	377610659	377611923	1264	hard	yes

Continued on next page

TABLE 2 – continued

Reference <sup>1</sup>	MJD <sup>2</sup>	MET <sup>3</sup> Start	MET <sup>3</sup> Stop	Exposure (s)	Type	Spectral fit <sup>4</sup>
4370_c	53723.55911	377614867	377617747	2880	hard	yes
4377_a	53730.43411	378208803	378211811	3008	hard	yes
4377_b	53730.51661	378216995	378217875	880	hard	yes
4387_a	53740.47429	379077106	379078450	1344	hard	yes
4387_b	53740.54058	379082930	379084082	1152	hard	yes
4387_c	53740.60697	379088818	379089666	848	hard	yes
4391_a	53744.46438	379422194	379422850	656	hard	yes
4418_a	53771.52180	381759283	381761283	2000	hard	yes
4425_a	53778.32680	382346563	382349907	3344	hard	yes
4435_a	53788.29726	383208963	383210403	1440	hard	yes
4435_b	53788.43134	383220819	383221715	896	hard	yes
4441_a	53794.32393	383729619	383731155	1536	hard	yes
4450_a	53803.29522	384504547	384506467	1920	hard	yes
4450_b	53803.36208	384510435	384512131	1696	hard	yes
4456_a	53809.25402	385019203	385021491	2288	hard	yes
4456_b	53809.31967	385024883	385027155	2272	hard	yes
4462_a	53815.21097	385533619	385536435	2816	hard	yes
4476_a	53829.22263	386744355	386746915	2560	hard	yes
4481_a	53834.86022	387231011	387234435	3424	hard	yes
4481_b	53834.92550	387236627	387240099	3472	hard	yes
4484_a	53837.16532	387431203	387432563	1360	hard	yes
4498a_a	53851.11411	388636115	388638003	1888	hard	yes
4498a_b	53851.18069	388641923	388643699	1776	hard	yes
4498b_a	53851.24735	388647795	388649347	1552	hard	yes
4498b_b	53851.31272	388653699	388654739	1040	hard	yes
4499_a	53852.16300	388726787	388728579	1792	hard	yes
4506_a	53859.23513	389337715	389339715	2000	hard	yes
4506_b	53859.29291	389342035	389345379	3344	hard	yes
4580_a	53933.90402	395789443	395790771	1328	hard	yes
4581_a	53934.00698	395798627	395799379	752	hard	yes
4581_b	53934.07328	395804339	395805123	784	hard	yes
4586_a	53939.86430	396304323	396305827	1504	hard	yes
4586_b	53939.99671	396316179	396316851	672	hard	yes
4587_a	53940.06522	396322067	396322803	736	hard	yes
4594_b	53947.91995	397000307	397001859	1552	hard	yes
4643_b	53996.24115	401174339	401177731	3392	hard	yes
4652_b	54005.81069	402001971	402003715	1744	hard	yes
4658_a	54011.70235	402510867	402512899	2032	hard	yes
4658_b	54011.76615	402516227	402518563	2336	hard	yes
4658_c	54011.82559	402520851	402524211	3360	hard	yes
4666_a	54019.68421	403199859	403203171	3312	hard	yes
4666_b	54019.74958	403205507	403208819	3312	hard	yes
4672_a	54025.44634	403697699	403701027	3328	hard	yes
4674_a	54027.68032	403891379	403893379	2000	hard	yes
4674_b	54027.73865	403895811	403899027	3216	hard	yes
4680_b	54033.74726	404416179	404416947	768	hard	yes
4697_a	54050.06948	405825123	405828483	3360	hard	yes
4697_b	54050.13485	405830771	405834131	3360	hard	yes
4698_a	54051.58430	405956787	405958579	1792	hard	yes
4698_b	54051.65115	405962675	405964243	1568	hard	yes
4698_c	54051.71745	405968483	405969891	1408	hard	yes
4698_d	54051.78319	405974323	405975411	1088	hard	yes
4705_a	54058.97430	406594547	406597811	3264	hard	yes
4707_a	54060.55161	406731347	406733571	2224	hard	yes
4707_b	54060.61809	406737171	406739235	2064	hard	yes
4707_c	54060.74772	406748259	406750547	2288	hard	yes
4714_a	54067.55235	407335731	407338915	3184	hard	yes
4714_b	54067.61680	407341203	407344579	3376	hard	yes
4725_a	54078.49013	408281075	408283619	2544	hard	yes
4725_b	54078.53698	408285955	408286835	880	hard	yes
4725_c	54078.55671	408286915	408289283	2368	hard	yes
4725_d	54078.60476	408291587	408292915	1328	hard	yes
4737_a	54090.54809	409323667	409324643	976	hard	yes
4737_b	54090.61485	409329539	409330307	768	hard	yes
4737_c	54090.68161	409335411	409335971	560	hard	yes
4744_a	54097.48606	409922819	409924371	1552	hard	yes
4744_b	54097.55282	409928691	409930035	1344	hard	yes
4747_a	54100.43078	410177123	410178915	1792	hard	yes
4747_b	54100.49772	410183027	410184579	1552	hard	yes
4747_c	54100.56328	410188819	410190115	1296	hard	yes
4758_a	54111.42671	411127011	411129123	2112	hard	yes

Continued on next page

TABLE 2 – continued

Reference <sup>1</sup>	MJD <sup>2</sup>	MET <sup>3</sup> Start	MET <sup>3</sup> Stop	Exposure (s)	Type	Spectral fit <sup>4</sup>
4758_b	54111.49282	411132723	411134835	2112	hard	yes
4758_c	54111.55671	411138099	411140499	2400	hard	yes
4758_d	54111.61559	411142803	411145971	3168	hard	yes
4765_a	54118.42597	411731155	411734451	3296	hard	yes
4765_b	54118.49143	411736803	411740115	3312	hard	yes
4765_c	54118.55680	411742435	411745779	3344	hard	yes
4771_a	54124.38328	412245827	412249203	3376	hard	yes
4771_b	54124.44893	412251523	412254851	3328	hard	yes
4771_c	54124.51439	412257171	412260515	3344	hard	yes
4778_a	54131.38791	412851059	412854371	3312	hard	yes
4778_b	54131.44069	412856755	412857795	1040	hard	yes
4778_c	54131.50791	412862707	412863459	752	hard	yes
4778_d	54131.57235	412868051	412869251	1200	hard	yes
4784_a	54137.35911	413368035	413369219	1184	hard	yes
4784_b	54137.42717	413374131	413374883	752	hard	yes
4784_c	54137.52763	413382803	413383571	768	hard	yes
4791_a	54144.36522	413973299	413974611	1312	hard	yes
4791_c	54144.49902	413985091	413985939	848	hard	yes
4798_a	54151.30208	414572403	414574195	1792	hard	yes
4798_b	54151.36911	414578307	414579875	1568	hard	yes
4798_c	54151.50235	414590019	414591187	1168	hard	yes
4806_a	54159.28661	415262099	415264227	2128	hard	yes
4806_c	54159.41865	415273779	415275363	1584	hard	yes
4813_a	54166.94930	415924435	415926003	1568	hard	yes
4820a_a	54173.16828	416461731	416463347	1616	hard	yes
4820b_a	54173.42559	416483571	416485971	2400	hard	yes
4824_a	54177.40291	416827635	416829187	1552	hard	yes
4830_a	54183.23930	417330995	417334355	3360	hard	yes
4834_a	54187.88726	417732531	417735987	3456	hard	yes
4840_a	54193.20356	418192915	418194259	1344	hard	yes
4840_b	54193.27032	418198803	418199907	1104	hard	yes
4840_c	54193.33726	418204707	418205571	864	hard	yes
4861a_a	54214.01022	419990131	419992435	2304	hard	yes
4861a_b	54214.07421	419996019	419997603	1584	hard	yes
4861b_a	54214.59634	420040419	420043427	3008	hard	yes
4869_a	54222.12606	420690835	420694147	3312	hard	yes
4869_b	54222.19143	420696467	420699811	3344	hard	yes
4869_c	54222.25680	420702115	420705459	3344	hard	yes
4873_a	54226.63828	421081011	421083683	2672	hard	yes
4876_b	54229.19504	421301571	421304931	3360	hard	yes
4879_a	54232.45874	421584355	421586115	1760	hard	yes
4882_a	54235.13689	421816195	421817059	864	hard	yes
4882_b	54235.20328	421821891	421822835	944	hard	yes
4890_a	54243.15374	422508819	422509747	928	hard	yes
4890_b	54243.25374	422517635	422518211	576	hard	yes
4898_a	54251.13809	423198467	423199795	1328	hard	yes
4898_b	54251.20448	423204275	423205459	1184	hard	yes
4903_c	54256.17726	423633795	423635235	1440	hard	yes
4911_a	54264.01717	424311667	424312099	432	hard	yes
4932_a	54285.95837	426206803	426208403	1600	soft	yes
4951_a	54304.87402	427841107	427842723	1616	soft	yes
4951_b	54304.94226	427846979	427848643	1664	soft	yes
4967_a	54320.83921	429219795	429222819	3024	soft	no
4973a_a	54326.32976	429694547	429696835	2288	soft	no
4973b_a	54326.72800	429728419	429731779	3360	soft	yes
4975_a	54328.96967	429923507	429924051	544	soft	yes
4975_b	54329.00958	429926563	429927891	1328	soft	yes
4981_a	54334.83356	430429603	430431235	1632	soft	no
4981_b	54334.89504	430435267	430436195	928	soft	no
4985_a	54338.85124	430777107	430777987	880	soft	no
4985_b	54338.95282	430785891	430786755	864	soft	no
4993_a	54346.76958	431460947	431462435	1488	soft	no
4993_b	54346.83541	431466835	431467923	1088	soft	no
4993_c	54346.90328	431472739	431473747	1008	soft	no
4998_a	54351.74217	431890531	431892115	1584	soft	no
4998_b	54351.80967	431896403	431897907	1504	soft	no
4998_c	54351.87597	431902211	431903555	1344	soft	no
4999_a	54352.13884	431925011	431926179	1168	soft	no
5005_a	54358.34356	432460003	432463363	3360	soft	no
5005_b	54358.40171	432465699	432467715	2016	soft	no
5018_c	54371.11059	433564243	433565267	1024	soft	yes

Continued on next page

TABLE 2 – continued

Reference <sup>1</sup>	MJD <sup>2</sup>	MET <sup>3</sup> Start	MET <sup>3</sup> Stop	Exposure (s)	Type	Spectral fit <sup>4</sup>
5019_a	54372.94847	433722691	433724403	1712	soft	no
5020_a	54373.06402	433732419	433734643	2224	soft	no
5044_a	54397.62597	435854931	435856435	1504	soft	no
5044_b	54397.69282	435860819	435862099	1280	soft	no
5050_a	54403.64643	436375011	436376691	1680	soft	no
5050_b	54403.71198	436380931	436382099	1168	soft	no
5058_a	54411.62893	437064579	437066499	1920	soft	yes
5058_b	54411.69217	437070387	437071619	1232	soft	yes
5071_a	54424.70865	438194099	438197155	3056	soft	no
5085_a	54438.51930	439387219	439390515	3296	soft	no
5093_a	54446.51476	440079203	440080147	944	soft	yes
5100_a	54453.51856	440684003	440685603	1600	soft	no
5100_b	54453.58513	440689859	440691251	1392	soft	no
5114_b	54467.51791	441893155	441895539	2384	soft	yes
5134_a	54487.52393	443622387	443623347	960	soft	yes
5134_b	54487.59022	443628035	443629155	1120	soft	yes
5140_a	54493.37513	444127795	444129027	1232	soft	yes
5148_b	54501.42550	444823299	444824627	1328	soft	no
5162_a	54515.29115	446021011	446022899	1888	soft	no
5162_b	54515.35754	446026787	446028595	1808	soft	no
5168_a	54521.30847	446540659	446543043	2384	soft	no
5174_a	54527.26272	447055715	447056883	1168	soft	yes
5180_a	54533.34356	447580339	447583027	2688	soft	no
5205_a	54558.15513	449724707	449726099	1392	soft	no
5205_b	54558.28698	449736387	449737203	816	soft	no
5211_a	54564.17541	450244675	450246435	1760	soft	no
5211_b	54564.23735	450250467	450251347	880	soft	yes
5216_a	54569.34032	450690259	450693347	3088	soft	yes
5231_a	54584.13411	451968963	451971011	2048	hard	yes
5231_b	54584.19217	451973331	451976675	3344	hard	yes
5236_a	54589.10643	452398515	452400675	2160	hard	yes
5236_b	54589.28217	452414307	452415251	944	hard	yes
5244_a	54597.09578	453089203	453090547	1344	hard	yes
5244_b	54597.16309	453095187	453096195	1008	hard	yes
5244_c	54597.22976	453101043	453101859	816	hard	yes
5252_a	54605.07772	453778691	453780339	1648	hard	yes
5262_a	54615.08319	454643251	454644723	1472	hard	yes
5262_b	54615.21569	454654387	454656483	2096	hard	yes
5266_a	54619.07374	454987811	454989731	1920	hard	yes
5266_b	54619.13948	454993891	454995011	1120	hard	yes
5275_a	54628.16115	455772531	455775315	2784	hard	yes
5280_a	54633.07171	456196659	456199731	3072	hard	yes
5289_a	54642.96384	457052243	457053507	1264	hard	yes
5290_a	54643.03171	457058323	457059155	832	hard	yes
5290_b	54643.13263	457067091	457067827	736	hard	yes
5291_a	54644.99384	457227731	457228803	1072	hard	yes
5291_b	54645.06050	457233667	457234387	720	hard	yes
5307_a	54660.95550	458606451	458608259	1808	hard	yes
5308_a	54661.01911	458612339	458613363	1024	hard	yes
5316_a	54669.06717	459307203	459309203	2000	hard	yes
5316_b	54669.12439	459311523	459314771	3248	hard	yes
5320_a	54673.05661	459651731	459654051	2320	hard	yes
5326_a	54679.07208	460171107	460174147	3040	hard	yes
5344_a	54697.86254	461795571	461796675	1104	hard	yes
5344_b	54697.92939	461801475	461802323	848	hard	yes
5349_a	54702.83430	462224979	462226387	1408	hard	yes
5358_a	54711.72726	462993091	462994979	1888	hard	yes
5364_a	54717.74439	463512947	463514883	1936	hard	yes
5364_b	54717.81282	463518819	463520835	2016	hard	yes
5370_a	54723.82782	464038131	464040915	2784	hard	yes
5547_a	54900.72245	479322163	479324275	2112	hard	yes
5653_a	55006.97337	488502627	488503971	1344	soft	yes
5653_b	55007.03735	488508515	488509139	624	soft	yes
5658_a	55011.81059	488920067	488922403	2336	soft	yes
5695_a	55048.83791	492119731	492121059	1328	soft	yes
5710_a	55063.81476	493413475	493415315	1840	hard	yes
5710_b	55063.87763	493419331	493420323	992	hard	yes
5715_a	55068.98115	493859811	493861731	1920	hard	yes
5791_a	55144.53208	500387987	500388755	768	hard	yes
5797_a	55150.54606	500907235	500908723	1488	hard	yes
5912_a	55265.58245	510846755	510847491	736	hard	yes

Continued on next page

TABLE 2 – continued

Reference <sup>1</sup>	MJD <sup>2</sup>	MET <sup>3</sup> Start	MET <sup>3</sup> Stop	Exposure (s)	Type	Spectral fit <sup>4</sup>
5918_a	55271.26828	511337379	511339379	2000	hard	yes
5918_b	55271.33365	511343331	511344723	1392	hard	yes
5924_a	55277.60124	511884083	511887011	2928	hard	yes
5933_a	55286.42226	512646723	512648643	1920	hard	yes
5937_a	55290.68495	513015683	513016275	592	hard	yes
5946_a	55299.19356	513750579	513751667	1088	hard	yes
6071_a	55424.90782	524612131	524613539	1408	hard	yes
6071_b	55424.97634	524617763	524619747	1984	hard	yes
6081_a	55434.59189	525449091	525449987	896	hard	yes
6100_a	55453.66985	527097251	527098499	1248	hard	yes
6107_a	55460.67013	527701795	527703603	1808	hard	yes
6114_a	55467.99208	528334547	528336083	1536	hard	yes
6120_a	55473.53671	528813475	528815267	1792	hard	yes
6128_a	55481.64115	529513603	529515587	1984	hard	yes
6143_a	55496.60893	530806147	530809475	3328	hard	yes
6148_a	55501.56226	531235379	531236179	800	hard	yes
6148_b	55501.58328	531236867	531238323	1456	hard	yes
6162_a	55515.63948	532451331	532452771	1440	hard	yes
6239_a	55592.47587	539090131	539091299	1168	hard	yes
6247_a	55600.32022	539766771	539770163	3392	hard	yes
6255_a	55608.30476	540457603	540459059	1456	hard	yes
6255_b	55608.37161	540463491	540464723	1232	hard	yes
6262_a	55615.29448	541061395	541063091	1696	hard	yes
6262_b	55615.36171	541067283	541068819	1536	hard	yes
6269_a	55622.28393	541665123	541667139	2016	hard	yes
6269_b	55622.34597	541671027	541671955	928	hard	yes
6275_a	55628.29328	542184227	542186451	2224	hard	yes
6304_b	55657.24171	544685955	544687011	1056	hard	yes
6311_a	55664.16180	545283667	545285091	1424	hard	yes
6311_b	55664.22985	545289555	545290963	1408	hard	yes
6339_a	55692.22745	547708387	547710115	1728	hard	yes
6345_a	55698.11347	548216147	548219459	3312	hard	yes
6352_a	55705.04847	548816339	548817635	1296	hard	yes
6387_a	55740.09791	551843939	551846579	2640	hard	yes
6394_a	55747.01217	552441891	552443411	1520	hard	yes
6398_a	55751.90569	552864963	552865939	976	hard	yes
6398_b	55751.93032	552866803	552868355	1552	hard	yes
6479_a	55832.74402	559848547	559851219	2672	soft	yes
6483_a	55836.97504	560214419	560216467	2048	soft	yes
6497_a	55850.67198	561398371	561399347	976	soft	no
6548_a	55901.49522	565788291	565791683	3392	hard	yes
6556_a	55909.46115	566477475	566479011	1536	hard	yes
6556_b	55909.52809	566483411	566484643	1232	hard	yes
6560_a	55913.16634	566796675	566800067	3392	hard	yes
6562_a	55915.52393	567001315	567002819	1504	hard	yes
6562_b	55915.59059	567007203	567008451	1248	hard	yes
6568_a	55921.45272	567513347	567515283	1936	hard	yes
6568_b	55921.51902	567519171	567520915	1744	hard	yes
6574_a	55927.11476	568001875	568005155	3280	hard	yes

<sup>1</sup> Data reference name, using MET day (see note 3).<sup>2</sup> Modified Julian Date of exposure midpoint; MDJ = JD - 2400000.5.<sup>3</sup> Mission Elapsed Time (MET), here in integer seconds, is the time since 1994 January 1 0 h (UTC). The truncated fraction is 0.374 s. RXTE Standard 2 data is collected during 16-s intervals of Spacecraft time (SCT), which is related by: MET = SCT + 3.374<sup>4</sup> Indicates whether a good-fit (i.e. a fit with  $\chi^2_\nu < 2$ ) was achieved or not.